

PRESSURE DISTURBANCE UPSTREAM OF THE BOUNDARY LAYER DATA SYSTEM

A Thesis

presented to

the Faculty of California Polytechnic State University,

San Luis Obispo

In Partial Fulfillment

of the Requirements for the Degree

Master of Science in Mechanical Engineering

by

Michelle Simone Leclere

July 2022

© 2022

Michelle Simone Leclere

ALL RIGHTS RESERVED

COMMITTEE MEMBERSHIP

TITLE: Pressure Disturbance Upstream of the
Boundary Layer Data System

AUTHOR: Michelle Simone Leclere

DATE SUBMITTED: July 2022

COMMITTEE CHAIR: Russell Westphal, Ph.D.
Professor of Mechanical Engineering

COMMITTEE MEMBER: Kim Shollenberger, Ph.D.
Professor of Mechanical Engineering

COMMITTEE MEMBER: Nandeesh Hiremath, Ph.D.
Professor of Aerospace Engineering

ABSTRACT

Pressure Disturbance Upstream of the Boundary Layer Data System

Michelle Simone Leclere

The primary objective for this work was to evaluate the reliability of computational fluid dynamics (CFD) tools in the prediction of upstream surface pressure disturbance and pressure drag of various instrument excrescence shapes for a small aircraft flight test device called the Boundary Layer Data System (BLDS). Insights on pressure disturbance will serve as a guide for the placement of BLDS probes/sensors, and pressure drag can be used to ensure sufficient adhesive is used to install BLDS instrumentation. The Mach number for all CFD cases was 0.12 and the Reynolds number based on excrescence height varied from 4×10^4 to 1×10^5 . Excrescences studied have height to local boundary layer thickness ratios $0.75 < h/\delta < 1.9$ and width to height ratios $3 \leq w/h < 4$.

Wind tunnel tests were first conducted in the Cal Poly Fluids Lab's 2 x 2-foot wind tunnel to obtain measurements of the upstream pressure disturbance created by a blunt BLDS housing and a streamlined BLDS fairing. Upstream surface pressure data was measured for two-dimensional excrescences and for three-dimensional models of the blunt and streamlined housings. A rake measurement of the undisturbed boundary layer profile at the leading edge location of each excrescence was also obtained to compare to the computed boundary layer.

Prior to viscous modeling with CFD, potential flow theory was used to compute the inviscid upstream pressure disturbance for a generic excrescence on a smooth surface. A Rankine oval was generated using superposition, and a MATLAB program was written to evaluate ovals of varying chord and height. The potential flow results for the pressure distribution upstream of a Rankine oval were found to agree quite well with 2-D measurements and viscous CFD.

Ansys ICEM CFD and FLUENT were used for computational modeling. A viscous CFD model was first created in two-dimensions and validated by comparing the upstream pressure disturbance results to the two-dimensional experimental measurements. The validated FLUENT case set-up was extended to three-dimensions, and three-dimensional models were created for blunt and streamlined BLDS excrescences. ICEM CFD was used to generate meshes for 2-D and 3-D models and FLUENT was used to solve the Reynolds-Averaged Navier Stokes (RANS) equations in conjunction with the Spalart-Allmaras turbulence model. Mesh independence studies and evaluation of discretization error were conducted to ensure that the final mesh employed provided adequate spatial resolution. The computed flow features, and results for dimensionless pressure and drag, were compared to experimental measurements and classic aerodynamic principles to evaluate the CFD solutions.

It was concluded that CFD can accurately compute upstream pressure disturbances and pressure drag for excrescences mounted to a smooth surface. The viscous calculations showed that the effect of excrescence shape on upstream pressure field is only significant within 6 body heights of the leading edge. Beyond that, no significant difference in the pressure disturbance was observed between different excrescence configurations. Additionally, the spanwise pressure disturbance was found to become negligible at about 1-1.5 housing widths away from the upstream centerline of each excrescence regardless of its shape. Finally, all computed blunt housing models resulted in a pressure drag coefficient of about 0.5 which corroborates past experimental drag measurements. This thesis has set-up a working FLUENT CFD case that can be used for future computational studies related to the BLDS and provides detailed guidance for existing BLDS housing shapes beyond the rules of thumb currently used for informing housing designs.

ACKNOWLEDGMENTS

I would like to express my sincere gratitude to my committee chair, Dr. Russell Westphal, who guided me through this project. His expertise in Fluid Mechanics offered deep insight into this work, and his patience and enthusiasm will leave a lasting impact on myself and many others.

Thank you to Dr. Kim Shollenberger and Dr. Nandeesh Hiremath for taking the time to review my thesis and be a part of my committee. A special thanks to Dr. Kim Shollenberger for sparking my interest in CFD and Fluid Mechanics in general.

Lastly, I would like to thank my family and friends for their continuous love and support throughout this process. I could not have completed this work without the strength they give me to move forward each day.

TABLE OF CONTENTS

	Page
LIST OF TABLES	x
LIST OF FIGURES	xii
LIST OF NOMENCLATURE	xvii
CHAPTERS	
1. INTRODUCTION	1
1.1 Background	1
1.2 Dimensionless Parameters.....	10
1.3 Using Potential Flows.....	17
1.4 Computational Methods.....	21
2. EXPERIMENTAL PRELIMINARIES.....	30
2.1 Two-Dimensional Experiments.....	31
2.2 Three-Dimensional Experiments.....	42
2.2.1 Blunt Body Experiment.....	43
2.2.2 Streamlined Body Experiment.....	45
2.3 Boundary Layer Measurement.....	47
3. 2-D CFD CASES AND CALIBRATION.....	51
3.1 2-D Inviscid Analysis	51
3.2 2-D Model Design and Case Set-Up	58
3.2.1 2-D Model Design in ICEM CFD	58
3.2.2 2-D Case Set-Up in FLUENT	68

4. 3-D CFD CASES.....	86
4.1 3-D Model Designs in ICEM CFD.....	87
4.1.1 3-D Ramped-Front Enclosure	88
4.1.2 3-D Half-Scale Fairing.....	93
4.2 3-D Case Set-Ups in FLUENT.....	96
5. CONCLUSIONS AND RECOMMENDATIONS.....	124
5.1 Conclusions	125
5.1.1 2-D CFD Conclusions.....	125
5.1.2 3-D CFD Conclusions.....	126
5.2 Recommendations.....	130
REFERENCES.....	133
APPENDICES	
A. Test Set-Up & BLDS Housing Shapes from Past Pressure Disturbance Experiment...	136
B. 2-D Experiment Raw Data for Test Cases 1 and 2.....	139
C. Empty Tunnel Correction Raw Data.....	140
D. 3-D Experiment Raw Data for Test Cases 3 and 4.....	141
E. Boundary Layer Rake Experiment Raw Data.....	142
F. MATLAB Scripts for all Inviscid Analyses	143
G. 2-D Geometry Replay Script	151
H. Discretization Error Calculations for 2-D and 3-D Meshes.....	154
I. 3-D RFE-A Mesh, Height, and Width Independence Study	156
J. 3-D HSF-A Mesh, Height, and Width Independence Study.....	160

K. p_{ref} Locations and Values for all 2-D and 3-D CFD Cases	164
---	-----

LIST OF TABLES

Table	Page
2-1: Experimental Cases	31
2-2: Boundary Layer Parameters Computed From Collected Profile Data	50
3-1: 2-D Domain/Mesh Identifiers	59
3-2: 2-D Mesh Independence Study Case Identifiers	65
3-3: 2-D Height Independence Study Case Identifiers	67
3-4: 2-D CFD Cases	69
3-5: 2-D Simulation Solver Settings	70
3-6: Boundary Conditions (BC's) for 2-D FLUENT Cases	71
3-7: Solution Methods for 2-D CFD Cases	71
3-8: Solution Under-Relaxation Factors for Pressure-Based SIMPLE Algorithm	72
3-9: Reynolds Numbers From 2-D CFD Cases and Wind Tunnel Experiments	74
3-10: Height to Boundary Layer Thickness Ratios, h/δ , for 2-D CFD Cases	84
3-11: Pressure Drag Coefficients for 2-D Cases 3 and 4	85
4-1: 3-D Domain/Mesh Identifiers	87
4-2: 3-D CFD Cases	96
4-3: Boundary Conditions for 3-D RFE Cases	97
4-4: Boundary Conditions for 3-D HSF Cases	97
4-5: Solution Methods for 3-D CFD Cases	98
4-6: Reynolds Numbers From 3-D CFD Cases and Wind Tunnel Experiments	101
4-7: Height to Boundary Layer Thickness Ratios, h/δ , for 3-D CFD Cases	104

4-8: Pressure Drag Coefficients for 3-D Cases 1 and 2.....	117
4-9: 3-D FLUENT Pressure Disturbance and Pressure Drag Results by Case	122
A-1: Summary of Test Cases From Past Pressure Disturbance Experiment ⁷	136
H-1: Discretization Error Estimation for 2-D Tall Mesh.....	154
H-2: Discretization Error Estimation for 3-D RFE Mesh.	155
H-3: Discretization Error Estimation for 3-D HSF Mesh.	155
I-1: 3-D Ramped-Front Enclosure Mesh Independence Study Case Identifiers.	156
I-2: 3-D RFE Height Independence Study Case Identifiers.	157
I-3: 3-D RFE Width Independence Study Case Identifiers	157
I-4: 3-D RFE-A Mesh Edge Parameters.	159
J-1: 3-D Half-Scale Fairing Mesh Independence Study Case Identifiers.	160
J-2: 3-D HSF Height Independence Study Case Identifiers.	161
J-3: 3-D HSF Width Independence Study Case Identifiers.	161
J-4: 3-D HSF-A Mesh Edge Parameters.	163
K-1: Free Stream Reference Static Pressure for CFD Cases.	165

LIST OF FIGURES

Figure	Page
1-1: First Generation BLDS on Cessna 206 StationAir II Turbo ¹	2
1-2: Exploded View of BLDS Electronics Unit ³	2
1-3: BLDS-R, Rake Arrays, and Static Probes Installed on E170 Vertical Tail ⁴	3
1-4: Corrected Experimental Pressure Coefficients Upstream of Several BLDS Housing Configurations. Private Communication, 2018 ⁷	5
1-5: Drag Coefficients of 3-D Protuberances. Adapted From Hoerner ⁵ Fig. 5-13.	7
1-6: BLDS Configurations and C_D Results. Private Communication, 2017 ⁸	9
1-7: Schematic of BLDS Housing on a Flat Surface.	13
1-8: Superposition of Uniform and Doublet Potential Flows ¹⁴	20
1-9: Flow Features over a 2-D Forward-Facing Step. Adapted from Sherry et.al, 2009 ²¹	25
1-10: Flow Features Over a 2-D Backward-Facing Step. Adapted from White Fig. 6-33 ²²	25
1-11: Structured (Left) & Unstructured (Right) 2-D Airfoil Mesh. From McLean Fig. 10.3.1 ¹⁶ ...	26
2-1: Diagram of BLDS Model in 2 x 2-Foot Wind Tunnel.	30
2-2: Tall (Left) and Short (Right) 2-D Wind Tunnel Models in 2 x 2-Foot Wind Tunnel.	32
2-3: Wind Tunnel Test Set-Up Used for 2-D Experiments.	33
2-4: Static Traverse Probe 0.25 Inches Above the Test-Section Floor.	34
2-5: Traverse Probe Aligned With Upstream Floor Scale.	35
2-6: Total-Static Pressure as a Function of Upstream Distance, x , for Test 2 (Short Model).	36
2-7: Pressure Coefficients as a Function of Upstream Distance, x , for Test 2 (Short Model)....	37
2-8: Surface C_P as a Function of x/h for 2-D Wind Tunnel Test 2 (Short Model).	38

2-9: Empty Tunnel C_p as a Function of Upstream Distance, x , at 50 Hz.	39
2-10: Corrected and Uncorrected C_p as a Function of x/h for Test 2 (Short Model).	40
2-11: Corrected C_p as a Function of x/h for Tests 1 (Tall Model) and 2 (Short Model).	41
2-12: BLDS Ramped-Front Enclosure With Critical Dimensions.	43
2-13: Wind Tunnel Test Set-Up Used for 3-D Blunt Body Experiment.	44
2-14: Upstream C_p as a Function of x/h for Test 3 (Ramped-Front Enclosure).	44
2-15: BLDS Half-Scale Fairing with Critical Dimensions.	45
2-16: Wind Tunnel Test Set-Up Used for 3-D Streamlined Body Experiment.	46
2-17: Upstream C_p as a Function of x/h for Test 4 (Half-Scale Fairing).	46
2-18: Corrected C_p Versus x/h for Tests 3 (Ramped-Front Enclosure) and 4 (Half-Scale Fairing).	47
2-19: Test Set-Up for Undisturbed Boundary Layer Profile Measurement.	48
2-20: Velocity Profile Taken 33.15 Inches Downstream of the Test-Section Inlet.	49
3-1: Generic Rankine Oval Potential Flow Created in IFM ²⁹	52
3-2: Rankine Oval Pressure Disturbance Experiment. Private Communication, 2014 ³⁰	53
3-3: Potential Flow Analysis Compared to Past Experimental C_p Measurements.	54
3-4: Schematic of 2-D Wind Tunnel Model for Comparison to Inviscid Analysis.	55
3-5: C_p from Tall ($h = 1.50$ in) 2-D Wind Tunnel Experiment Compared to Inviscid Analysis.	56
3-6: C_p from Short ($h = 0.713$ in) 2-D Wind Tunnel Experiment Compared to Inviscid Analysis.	56
3-7: ICEM Geometry for 2-D TB Model. Dimensions are in Inches.	59
3-8: Blocking Geometry for 2-D TB Model.	61
3-9: Mesh Pattern for 2-D TB Model.	62

3-10: Viscous Sublayer Resolution Technique. Adapted From Ansys Theory Guide ¹⁹	63
3-11: Structured Mesh for 2-D TB Model Including BC's.....	64
3-12: 2-D TB Mesh Independence Study.	66
3-13: 2-D TB Height Independence Study.	68
3-14: Scaled Residual Monitor From Processing 2-D CFD Case 2 (SB Model).	73
3-15: Upstream C_f for 2-D CFD Cases 1 and 2.....	75
3-16: Velocity Vector Plots for Cases 1 and 2.	76
3-17: Computed Upstream C_p From 2-D Case 1 (Tall) Compared to Experiment.....	77
3-18: Computed Upstream C_p From 2-D Case 2 (Short) Compared to Experiment.	77
3-19: 2-D CFD Upstream C_p for Cases 1 (Tall) and 2 (Short).	78
3-20: Wall-Bounded (Case 1) and Free-Air (Case 3) Upstream C_p for the Tall Excrescence.	79
3-21: Wall-Bounded (Case 2) and Free-Air (Case 4) Upstream C_p for the Short Excrescence. ...	80
3-22: 2-D CFD Case 3 Upstream C_p Compared to Inviscid Analysis.	81
3-23: 2-D CFD Case 4 Upstream C_p Compared to Inviscid Analysis.	82
3-24: Boundary Layer Velocity Profiles for Cases 5 and 6 Compared to Experiment.....	83
3-25: Curves Over Which Static Pressure is Integrated for 2-D Computation of C_{DP}	84
4-1: BLDS Ramped-Front Enclosure and Half-Scale Fairing Housings as Modeled in ICEM.	86
4-2: ICEM Geometry for 3-D RFE Model. Dimensions are in Inches.	88
4-3: 3-D RFE Model Surface Boundary Conditions.	89
4-4: 3-D RFE Model Blocking and Material Families.	90
4-5: Converged Mesh Pattern for 3-D RFE Model.	91
4-6: 2-D Fairing Domain Design Based on NASA Turbulence Modeling Resource ³¹	93

4-7: ICEM Geometry for 3-D HSF Model. Dimensions are in Inches.	94
4-8: 3-D HSF Model Surface Boundary Conditions.	94
4-9: Converged Mesh Pattern for 3-D HSF Domain.	95
4-10: Adapted HSF-A Mesh.	100
4-11: Computed Upstream C_p From 3-D Case 1 (RFE) Compared to Experiment.	102
4-12: Computed Upstream C_p From 3-D Case 2 (HSF) Compared to Experiment.	102
4-13: Boundary Layer Velocity Profile for Case 3 (RFE) Compared to Experiment.	103
4-14: Boundary Layer Velocity Profile for Case 4 (HSF) Compared to Experiment.	103
4-15: Center-Plane Particle Pathlines for Case 1 (RFE).	105
4-16: Upstream C_f From 3-D Case 1 (RFE).	106
4-17: Surface C_f Along Top of RFE for 3-D Case 1.	107
4-18: Center-Plane Particle Pathlines for Case 2 (HSF).	108
4-19: Upstream C_f From 3-D Case 2 (HSF).	108
4-20: Pathlines Along the Center-Plane for Case 1 (RFE).	109
4-21: Streamlines Past a Circular Cylinder. Adapted From Batchelor ¹¹ Figure 5.11.3.	110
4-22: Top View of Case 1 Pathlines.	110
4-23: Contours of Surface Static Pressure for Case 1 (RFE).	111
4-24: 3-D CFD Upstream C_p for Cases 1 and 2.	112
4-25: Spanwise C_p at Three Upstream Locations for 3-D Case 1 (RFE).	114
4-26: Spanwise C_p at Three Upstream Locations for 3-D Case 2 (HSF).	115
4-27: Surfaces Used to Integrate Static Pressure and Case 1 Characteristic Area.	116
4-28: Surfaces Used to Integrate Static Pressure and Case 2 Characteristic Area.	117

4-29: 3-D CFD Upstream C_p for RFE Case 7 (60° Ramp) and HSF Case 2.	118
4-30: 3-D CFD Upstream C_p for Enclosure Cases 1, 7 and 8.	120
4-31: 3-D CFD Upstream C_p for Cases 1, 5 and 6.	121
A-1: Experimental Set-Up from Past Pressure Disturbance Experiment ⁷	136
I-1: 3-D Ramped-Front Enclosure Mesh Independence Study.	156
I-2: 3-D RFE Height Independence Study.	157
I-3: 3-D Enclosure Width Independence Study.	158
I-4: 3-D RFE-A Mesh.	158
J-1: 3-D Half-Scale Fairing Mesh Independence Study.	160
J-2: 3-D HSF Height Independence Study.	161
J-3: 3-D HSF Width Independence Study.	162
J-4: 3-D HSF-A Mesh.	162
K-1: Location of Free Stream Reference Static Pressure for 2-D CFD Cases.	164
K-2: Location of Free Stream Reference Static Pressure for 3-D RFE Cases.	164
K-3: Location of Free Stream Reference Static Pressure for 3-D HSF Cases.	165

LIST OF NOMENCLATURE

Symbol	Meaning, [dimensions]
A	= Characteristic area of surface or excrescence, [m^2] or [in^2]
C	= Chord length, [in]
c	= Local speed of sound, [m/s]
C_D	= Drag coefficient, $\left(= \frac{drag}{q_{ref}A} \right)$
C_{DP}	= Pressure drag coefficient, $\left(= \frac{F_{DP}}{q_{ref}A} \right)$
C_f	= Skin friction coefficient, $\left(= \frac{\tau_w}{q_{ref}} \right)$
C_p	= Pressure coefficient, $\left(= \frac{(p_x - p_{ref})}{q_{ref}} \right)$
F_{DP}	= Drag force due to pressure, [N]
GCI_{fine}	= Fine grid convergence index
H	= Boundary layer shape factor, $\left(= \frac{\delta^*}{\theta_m} \right)$
h	= Maximum excrescence height, [in]
h_D	= Domain height, [in]
K	= Doublet strength, [m^2/s]
l	= Maximum excrescence length, [in]
M	= Mach number, $\left(\equiv \frac{U}{c} \right)$
m	= Point source strength, [m^2/s]
p	= Static pressure, [Pa]
p_0	= Total pressure, [Pa]

p_{ref}	=	Reference static pressure, [Pa]
p_x	=	Static pressure at upstream location x , [Pa]
q_{ref}	=	Reference dynamic pressure, [Pa]
r	=	Radial distance to origin, based on polar coordinate system, [in]
Re	=	Reynolds number, $\left(= \rho \frac{UL}{\mu}\right)$
Re_{δ}	=	Reynolds number based on local boundary layer thickness ($L = \delta$)
Re/L	=	Reynolds number per unit length, [ft^{-1}]
Re_h	=	Reynolds number based on maximum excrescence height ($L = h$)
$Re_{x_{le}}$	=	Reynolds number based on leading edge location ($L = x_{le}$)
t	=	Time, [s]
U	=	Free stream velocity, [m/s]
\vec{u}	=	Velocity vector field, magnitude in [m/s]
\bar{u}	=	Mean part in Reynolds decomposition of velocity, [m/s]
		Any variable with overbar accent represents a mean term.
u'	=	Fluctuating part in Reynolds decomposition of velocity, [m/s]
		Any variable with apostrophe represents a fluctuating term.
u_r	=	Radial velocity component in polar coordinate system, [m/s]
u_{θ}	=	Tangential velocity component in polar coordinate system, [m/s]
u_x	=	Axial velocity component in Cartesian coordinate system, [m/s]
u_y	=	Tangential component in Cartesian coordinate system, [m/s]
W	=	Excrescence half width, [in]

w	=	Maximum excrescence width, [<i>in</i>]
w_D	=	Domain width, [<i>in</i>]
w_e	=	Ramped-front enclosure width, [<i>in</i>]
w_f	=	Half-scale fairing width, [<i>in</i>]
x	=	Distance upstream of model leading edge, [<i>in</i>]
x_{le}	=	Excrescence leading edge location relative to the inlet, [<i>in</i>]
y^+	=	Dimensionless distance from excrescence and wall surfaces
δ	=	Local boundary layer thickness, [<i>in</i>]
δ^*	=	Displacement thickness, [<i>in</i>]
θ	=	Angular distance to abscissa in polar coordinate system, [<i>rad</i>]
θ_m	=	Momentum thickness, [<i>in</i>]
μ	=	Fluid dynamic viscosity, [<i>N-s/m²</i>]
ν	=	Fluid kinematic viscosity, [<i>m²/s</i>]
ρ	=	Fluid density, [<i>kg/m³</i>]
τ_{ij}	=	Reynolds stress tensor, ($\equiv \overline{\rho u_i' u_j'}$)
τ_w	=	Wall shear stress, [<i>N/m²</i>]
φ	=	Scalar velocity potential function
ψ	=	Stream function

1. INTRODUCTION

The objective of this thesis is to characterize the surface pressure disturbance created by excrescences of shapes used for small instrument housings and probe/sensor mounts in aircraft flight testing. Experimental, analytical, and especially computational (CFD) approaches are employed with the intent of evaluating the use of CFD to predict pressure disturbance and pressure drag on these types of excrescences. This work is motivated by the needs of the Boundary Layer Data System (BLDS) project, and the results of this work will serve as guidance for future BLDS student researchers in instrument housing design. This section includes background information associated with the BLDS project and relevant literature, dimensionless parameters, and the computational approach used for this work.

1.1 Background

The Boundary Layer Data System (BLDS) is a family of compact, lightweight, self-contained systems designed to measure boundary layer properties on an aircraft surface during flight^{1,2,4}. The basic requirements for all BLDS devices are that they must weigh less than 1 lb., be affixed directly to an aircraft using only adhesives, and require no connection to any aircraft systems¹. The first “proof-of-concept” BLDS prototype was flown in 2005 on the wing of a Cessna 206 StationAir experimental aircraft as depicted in Figure 1-1.



Figure 1-1: First Generation BLDS on Cessna 206 StationAir II Turbo¹.

In 2008, a third generation BLDS² was developed and tested solidifying the basic design of the system that persists in present configurations. Particularly, the third generation design included a main electronics unit with common programmable microcontroller that requires only software changes to operate the instrument in different configurations. Figure 1-2 shows an exploded view of the main BLDS electronics unit including the microcontroller, battery assembly, various insulation materials, and ramped-front aluminum housing³.

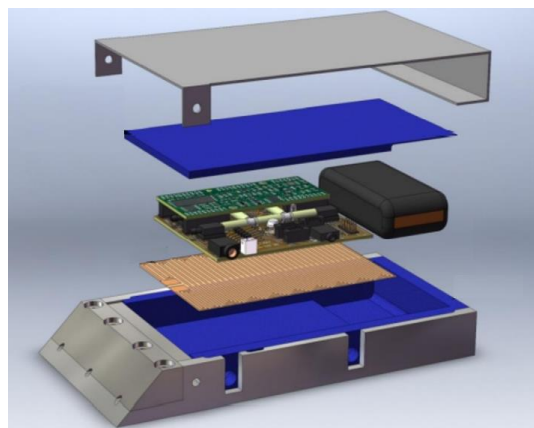


Figure 1-2: Exploded View of BLDS Electronics Unit³.

One version of the third generation BLDS, called the “BLDS-R”, contains sixteen 1.5 psid pressure sensors connected to an external rake array of fixed total pressure probes⁴. In 2016, the BLDS-R was included in the Boeing and Embraer ecoDemonstrator program and was flown on an Embraer 170 experimental aircraft. Figure 1-3 shows the arrangement of two external rake arrays, surface static probes, and the BLDS-R unit mounted to the vertical tail of the E170. A close-up of the static probe/rake array pair at location 1 is shown in the lower left.

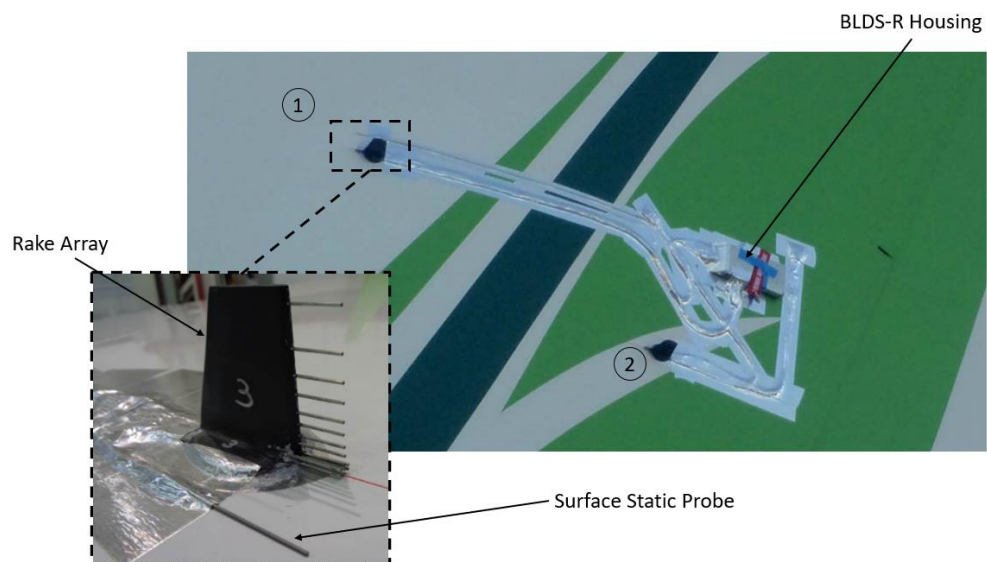


Figure 1-3: BLDS-R, Rake Arrays, and Static Probes Installed on E170 Vertical Tail⁴.

The enclosed electrical unit is a small protuberance on an otherwise smooth aerodynamic surface, so it imposes some level of disturbance to the surrounding pressure field during flight⁵. As shown in Figure 1-3, the BLDS-R electrical unit was installed quite far behind the rake array at position 1 to avoid flow disturbance to the boundary layer during in-flight measurements. At position 2, another static probe/rake array pair was placed off to its side. It is not uncommon for external pressure

measurement instruments like this to be mounted directly upstream, or in the spanwise vicinity, of the main BLDS electrical unit. However, in some flight test scenarios, the aircraft surface of interest has limited space over which BLDS instrumentation can be spread out⁶. Therefore, it is important to have a refined estimate of how far upstream the pressure field will be disturbed by the presence of the BLDS electrical unit.

Cal Poly student Neil Sharma conducted experiments in 2018 with several BLDS housing geometries to characterize the disturbance they introduce to the upstream pressure field⁷. In the past work, an aluminum plate containing 41 drilled surface static pressure taps was installed in the 2 x 2-foot Cal Poly wind tunnel test section upstream of each BLDS housing geometry evaluated. The leading edge of each model was placed directly at the 31st static pressure port, and a trip wire was installed to ensure the boundary layer growing on the test section floor was turbulent. The static pressures measured from the taps were used to compute the pressure coefficient, C_p , at each upstream location. The results for the upstream C_p values are presented below and images and dimensions of the housings studied in this work and test set-up can be seen in Appendix A.

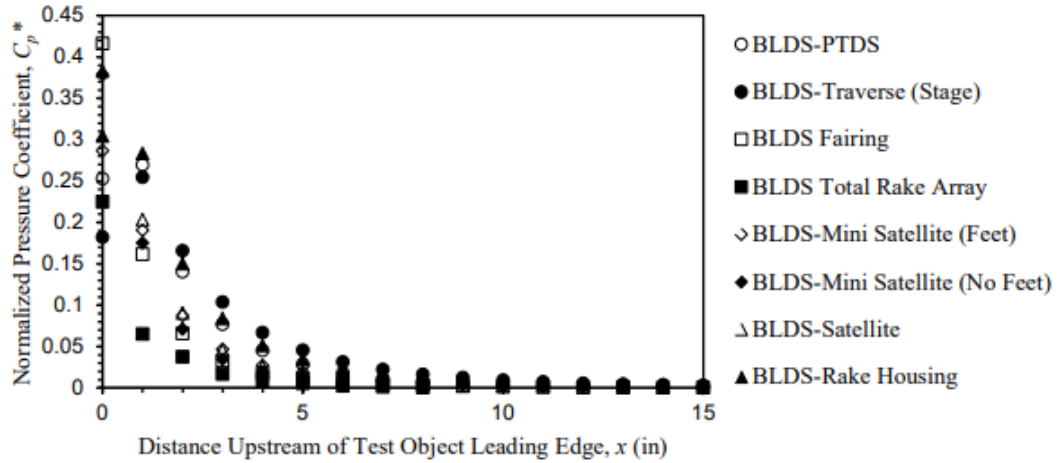


Figure 1-4: Corrected Experimental Pressure Coefficients Upstream of Several BLDS Housing Configurations. Private Communication, 2018⁷.

From the past work, it was found that the “BLDS Fairing” geometry causes the largest pressure disturbance directly at the model leading edge ($x = 0$ inches). However, the C_p curves in Figure 1-4 show that for $x > 1$ inch, the BLDS Fairing caused one of the smallest disturbances to the pressure field. By contrast, the “BLDS-Satellite”, which has the same shape as the ramped-front housing displayed in Figure 1-2, had one of the larger effects on the upstream pressure field until about 1 inch upstream of the model nose. At this point, the pressure disturbance from the BLDS Fairing became much larger, meeting $C_p \approx 0.415$ at its nose. In general, this work found that there is a large spread in the pressure coefficient values near the leading edge of each excrescence. However, as distance upstream increases, the pressure values between each shape approach each other and the spread decreases⁷. More specifically, the upstream pressure disturbance becomes negligible about 5-10 housing heights upstream of the unit⁷ regardless of its shape.

While this past work provides guidance on the extent of upstream pressure disturbance, it covers a broad range of BLDS housing geometries, many of which are no longer being used. This thesis aims to study the pressure disturbance upstream of specifically the ramped-front aluminum housing depicted in Figure 1-2 with the intent of refining past estimates of upstream pressure disturbance. Particularly, the upstream pressure disturbance for the ramped-front housing will be compared to that of several other similar ramped-front geometries, and a streamlined housing that resembles the BLDS Fairing, using computational fluid dynamic (CFD) methods. The spanwise pressure disturbance at several upstream locations will also be examined to estimate how far offset a pressure measurement device must be placed to avoid flow disturbed by the housing.

Another goal of this thesis is to compute the aerodynamic loads on several ramped-front geometries and a faired housing, compare them to the values obtained in past student work, and use them to make informed decisions about next generation BLDS main unit housing designs. One of the driving design constraints of all BLDS devices is that they be affixed to aircraft surfaces using only adhesives¹. In the case of the BLDS-R, this requirement was met by affixing the BLDS electrical unit to the E170 using 3M VHB 4658F viscoelastic structural adhesive tape⁴. While this method ensures that the BLDS is not permanently attached to the aircraft, it does introduce the risk of in-flight loads dislodging the BLDS from the aircraft surface. Therefore, the total in-flight load on the BLDS imposed by the flowing air is an important consideration in BLDS housing design.

Sighard Hoerner's *Fluid Dynamic Drag*⁵ is a common reference in any analysis of aerodynamic loads on small objects mounted to flat surfaces. In general, the drag on a small excrescence is dependent upon the excrescence height to local boundary layer thickness (h/δ), the Reynolds number, and the shape of the excrescence. Hoerner contends that the drag coefficients of 2-D and 3-D protuberances, the heights of which are in the order of or less than the boundary layer thickness, are proportional to $(h/\delta)^{1/3}$ regardless of their shape⁵. Thus, the drag coefficient of a protuberance *increases* with the Reynold's number⁵. The diagram adapted from Hoerner in Figure 1-5 provides a depiction of how the general shape of a 3-D excrescence immersed in a turbulent boundary layer affects the magnitude of its drag coefficient, C_D .

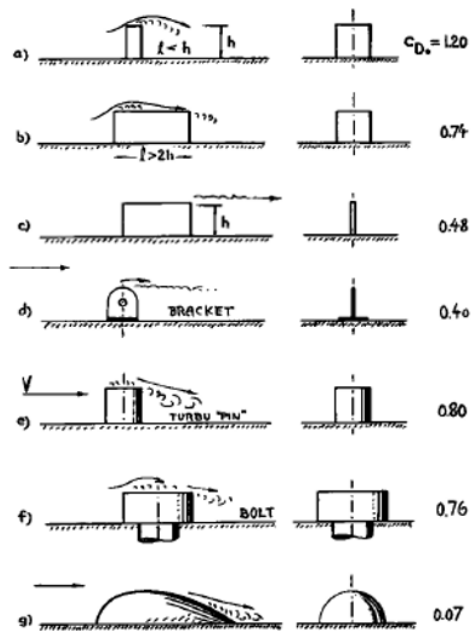


Figure 1-5: Drag Coefficients of 3-D Protuberances. Adapted From Hoerner⁵ Fig. 5-13.

The excrescences depicted in Figure 1-5 represent protuberances whose heights, h , are on the order of, or less than, the local boundary layer thickness, δ . In general, square “plates”, characterized by their streamwise length, l , being less than h , have C_D between 1.0 and 1.3⁵. Comparing the square plate of item A to the blunt, prismatic body of item B shows that increasing the streamwise length of the excrescence coincides with a reduction in C_D . More specifically, beyond $l \approx h$, the C_D can be expected to be less than 1.0 and eventually settle to a constant level with $C_D \approx 0.74$ for $l > 2h$. Additionally, the comparison between items B and C demonstrates that the drag coefficient is reduced for a blunt excrescence by reducing its width perpendicular to the direction of fluid flow without changing h . Cylindrical “pin” excrescences, like items E and F, that have rounded edges and flat tops, have comparatively high C_D values when compared to the prismatic bodies of items B and C. Item G has the smallest drag coefficient of all geometries and is characterized by rounded edges, curvature across its top, and a streamlined trailing edge.

The BLDS housing geometries studied in this thesis are expected to have drag coefficients consistent with the conventional observations from Hoerner because their heights are on the order of the local boundary layer thickness. However, BLDS housing design in the past has been based on an estimated in-flight drag coefficient of 1. Recent Cal Poly student project work done by Declan Mages⁸ attempted to refine this C_D estimate for several BLDS enclosure shapes using wake analysis. The results of Mages’ study are reproduced in Figure 1-6.

Model	C_D
A - Original	0.52
B - Boeing	0.33
C - w/Traverse	1.04
D - Fairing	0.16
E - Fairing w/Flat Back	0.19

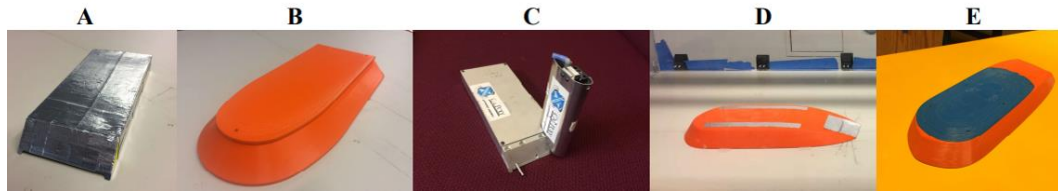


Figure 1-6: BLDS Configurations and C_D Results. Private Communication, 2017⁸.

The C_D values presented in Figure 1-6 are consistent with classic principles. The ramped-front shape of the “A-Original” model has $C_D \approx 0.52$ which is certainly less than the previously assumed $C_D = 1$. The “B-Boeing” housing also shows how rounding the front and streamlining the sides of the body can reduce C_D to about 0.3. By adding curvature to the top of the excrescence and streamlining its trailing edge, as demonstrated by housing D, the drag coefficient is almost halved again. It is important to note that fairings D and E are intended to be placed *on top of* an existing BLDS electrical unit. These fairings are called “drop-on” fairings and consequently have a larger height, width, and frontal area than simpler enclosures like the A-Original model. This thesis does not consider full-scale drop-on fairings. Instead, all fairing geometries used in the present work represent *half-scale* models of the larger drop-on fairings depicted in D and E of Figure 1-6.

Finally, this past study was conducted using two different methods: wake analysis and model suspension⁸. In the wake analysis, a grid of stagnation pressure readings was taken at the same location in the wind tunnel with and without the BLDS housing present, and the drag was computed from the difference in momentum. Therefore, the results from the wake analysis incorporate the *interference drag* between the flat floor of the wind tunnel and BLDS housing. Interference drag is the resistive force caused by the mutual interaction between the boundary layer of the flat surface and the excrescence when they are in contact with each other⁵. The suspension method *does not* include interference drag because the model is suspended on cables above the wind tunnel floor. When the resulting C_D 's from each method were compared, the values were approximately the same⁸. This suggests that the interference drag associated with connecting excrescences of this scale to a flat surface is very small⁶.

In general, Mages' work refined the estimate of C_D for a ramped-front enclosure from $C_D = 1$ to approximately $C_D = 0.5$, and this thesis aims to corroborate that experimental value with computed drag coefficients. Having a well-substantiated C_D is valuable for the BLDS project because it allows the team to meet required factors of safety making BLDS industry partners more comfortable with attaching the technology to aircraft⁶.

1.2 Dimensionless Parameters

This thesis aims to use computational methods to predict upstream pressure disturbances caused by, and aerodynamic loads imposed on, the BLDS main unit

housing. This section covers the dimensionless parameters that will be used to quantify the pressure disturbance, drag force and other flow characteristics throughout this thesis.

The variation in pressure across a smooth flat plate is zero⁹. Therefore, all the resistance to fluid flow over a flat plate is due to the shear stress at the surface of the plate. This resistive force is known as *skin friction* and it is commonly quantified using the skin friction coefficient, C_f .

$$C_f = \frac{\tau_w}{\frac{1}{2}\rho U^2} \quad (1-1)$$

In equation (1-1), ρ represents the density of the flowing fluid, and U represents the free stream velocity of the fluid. The denominator in equation (1-1) is known as dynamic pressure, q . For this thesis, the *reference dynamic pressure* will be defined as shown in equation (1-2).

$$q_{ref} = \frac{1}{2}\rho U^2 \quad (1-2)$$

The skin friction coefficient is an important dimensionless parameter in boundary layer flows, and it represents the fraction of the dynamic pressure that is felt as shear stress on the wall. Boundary layer separation occurs when the surface shear stress, τ_w , vanishes or reverses direction. For this reason, the skin friction coefficient serves as an indicator of when the boundary layer has separated. Particularly, $C_f = 0$ or $C_f < 0$ will represent a separated flow. The skin friction coefficient, and particularly its utility as a

boundary layer separation indicator, is a parameter of importance for external air flow over a small “bump” on a flat plate, as the boundary layer is expected to separate from the surface slightly upstream of the disturbance⁵.

The *drag force* felt by each BLDS housing geometry is also of particular importance to the present work. Drag is the component of force on a body acting parallel to the direction of relative motion⁹. Any small object mounted on an otherwise smooth, aerodynamic surface will introduce an additional component of drag known as *excrescence drag*. The term “excrescence” typically refers to small surface imperfections¹⁰ where the height of the excrescence h is far smaller than the local boundary layer thickness δ . More generally, excrescences encompass any protuberance on the surface of an aircraft whose height to local boundary layer thickness ratio, h/δ , is roughly ≤ 1 . These items often include rivet heads, sheet metal joins, antenna, stub wings or fairings¹⁰. The BLDS housings considered in this work are typically no more than about 1 inch in height and are in the range of $h/\delta \leq 5$, so they will be considered excrescences. However, the total drag associated with excrescences is not limited to the forces on the items themselves, but usually includes any changes in the skin friction on the surrounding surface due to their presence. Semi-empirical methods for estimating full-scale aircraft excrescence drag have been developed by the Engineering Sciences Data Unit (ESDU)¹⁰ and are widely used in the aviation industry. These ESDU Data Items present the excrescence drag as an *incremental* drag coefficient as it is compared to the drag on the smooth aerodynamic surface without the excrescence present. Therefore, the incremental excrescence drag is made up of the load on the excrescence itself, plus

any changes in skin friction on the surface surrounding it, minus the skin friction corresponding to the area covered by the excrescence¹⁰. However, the present work is not concerned with the way loading is disturbed on the aircraft surface surrounding the BLDS, but more so with the load felt by the housing itself. For that reason, an incremental drag coefficient will not be computed for each excrescence geometry. Instead, the *pressure drag coefficient*, C_{DP} , will be used to quantify the drag force felt by each BLDS housing geometry.

As depicted in Figure 1-7, the BLDS electrical unit is an excrescence mounted to an otherwise smooth flat surface.

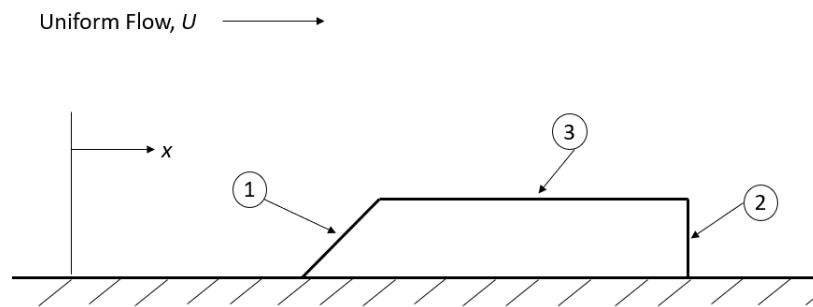


Figure 1-7: Schematic of BLDS Housing on a Flat Surface.

According to Hoerner, excrescences on flat surfaces like the BLDS may experience drag forces due to skin friction, pressure, and interference. As stated previously, the interference drag attributed to joining the BLDS housing to a flat surface is small and will not be included in any computation of drag on the BLDS for this thesis. In the absence of the excrescence, all drag imposed on the surface is due to skin friction⁹. When the BLDS

is added to the surface, the pressure variation across it is no longer zero. There is some wall shear stress that will exist across the top surface 3 in Figure 1-7, but this tangential force is expected to be quite small because the BLDS housing is a “blunt” body⁵. This means that its pressure drag is expected to be many times larger than the drag caused by skin friction. Therefore, the resultant differential between the pressure forces on the forward face at location 1 and the rear face at location 2 will be used to represent the drag imposed on each excrescence and will be referred to as the pressure drag.

The force on a surface due to pressure only is defined as the component of the resultant pressure force parallel to the velocity of the flowing fluid. For air flow in the x -direction, the pressure drag force on an excrescence surface can be calculated using the x -wise component of equation (1-3).

$$F_{DP} = \int_A (p \cdot dA) \vec{n} \quad (1-3)$$

The force due to pressure on a surface, F_{DP} , can be made into a dimensionless pressure drag coefficient by dividing by a reference dynamic pressure and a characteristic area.

$$C_{DP} = \frac{F_{DP}}{q_{ref}A} \quad (1-4)$$

For the present work, the characteristic area, A , will be computed by multiplying the maximum height, h , and maximum width, w , of each excrescence evaluated.

Any alteration of the pressure field relative to an undisturbed flow is called *pressure disturbance*. The *pressure coefficient*, C_p , is a parameter of importance for flow

near a small excrescence because it indicates the magnitude of the pressure differential between the local static pressure at a point of interest and some undisturbed reference static pressure value⁵. For the present work, C_p will be used to measure the pressure disturbance at the surfaces upstream and in the vicinity of BLDS housing geometries.

$$C_p = \frac{(p_x - p_{ref})}{q_{ref}} \quad (1-5)$$

The points of interest at which p_x will be computed lie along the surface upstream of the BLDS housing, and p_{ref} is the undisturbed static pressure at some location in the free stream far from the surface and BLDS housing.

In addition to capturing the computed pressure disturbance and drag force, it is desired to simulate flow characteristics that represent the actual BLDS testing environment. To ensure that the computed flow reasonably matches the actual flow, the *Mach* number, M , and *Reynolds* number, Re will be computed. The Mach number is a key parameter for characterizing compressibility effects in a flow, and it is defined as the ratio of flow speed, U to the local speed of sound, c .

$$M \equiv \frac{U}{c} \quad (1-6)$$

In general, if $M < 0.3$, the maximum density variation in the flow is less than 5% and the flow can be treated as incompressible⁹. The BLDS has been successfully operated at flight Mach numbers up to 0.84^{1,2,4}, but the present work focusses on BLDS geometries in subsonic flow with a maximum Mach number of 0.12 to best replicate the air flow in

the Cal Poly 2 x 2-foot wind tunnel test section. Compressibility will not be considered in any of the present analyses.

The Reynolds number based on several different characteristic sizes will also be used to characterize air flow over the BLDS surfaces. The Reynolds number is defined as

$$Re = \rho \frac{UL}{\mu} \quad (1-7)$$

Where μ is the molecular dynamic viscosity of the fluid, and L is the characteristic size scale in the flow⁹. The Re is of particular importance because it represents the ratio of inertial forces to viscous forces in the flow. In wind tunnel testing conducted with BLDS^{7,8} housings, the Reynolds number on a per unit length basis, Re/L , is typically on the order of $8 \times 10^5 \text{ ft}^{-1}$. In flight test scenarios, the Reynolds number for BLDS applications varies widely with choice of L . When the BLDS was flown on the wing of Scaled Composites' White Knight I aircraft in 2009¹², the Reynolds number based on wing chord was around 3×10^6 . Ultimately, the BLDS is typically operated at high Reynolds numbers, and the present work will focus on using Re/L , Reynolds number based on local boundary layer thickness (Re_δ) and Reynolds number based on model leading edge location ($Re_{x_{le}}$) to ensure the computer simulation properly represents the flow seen in the wind tunnel.

1.3 Using Potential Flows

A proper computational model including BLDS housing geometries must include a boundary layer. However, a natural precursor to any viscous analysis is an inviscid analysis to understand the basic flow structure. The over-arching mass-conservation equation in the study of thermodynamics and fluid mechanics, known as the *continuity equation*, provides the basis for inviscid analysis. For a steady state process, the continuity equation states that the rate at which mass enters a system is equivalent to the rate at which mass leaves the system.

$$\frac{\partial \rho}{\partial t} + \vec{\nabla} \cdot (\rho \vec{u}) = 0 \quad (1-8)$$

As previously stated, the air flowing across the BLDS surfaces will be considered incompressible. For an incompressible fluid, the rate of change in density, $\frac{\partial \rho}{\partial t}$ in equation (1-8), will be zero. If density is also considered uniform, the continuity equation reduces to a linear partial differential equation.

$$\vec{\nabla} \cdot \vec{u} = 0 \quad (1-9)$$

In equation (1-9), \vec{u} is a vector that represents the velocity field. For any *irrotational flow* the velocity field can be defined as the gradient of a scalar *velocity potential*, φ , and the continuity equation becomes what is known as *Laplace's Equation*.

$$\begin{aligned} \vec{\nabla} \cdot \vec{u} &= \vec{\nabla} \cdot (\vec{\nabla} \varphi) = 0 \\ \vec{\nabla}^2 \varphi &= 0 \end{aligned} \quad (1-10)$$

Solutions to Laplace's Equation are called *potential flows*. Since equation (1-10) is linear, its solutions can be added together, or superposed, to produce additional valid solutions. Like the velocity potential, the *stream function*, ψ , is another scalar parameter that relates the components of the velocity field and identically satisfies Laplace's equation. The 2-D velocity components expressed in terms of the stream function are obtained by differentiating ψ .

$$u_x = \frac{\partial \psi}{\partial y} \quad (1-11)$$

$$u_y = -\frac{\partial \psi}{\partial x} \quad (1-12)$$

These components can also be of practical use when they are defined in polar coordinates.

$$u_r = \frac{1}{r} \frac{\partial \psi}{\partial \theta} \quad (1-13)$$

$$u_\theta = -\frac{\partial \psi}{\partial r} \quad (1-14)$$

The stream function is of particular importance to inviscid analysis because it is used to determine the *streamlines* of a flow. A streamline is a line of flow characterized by its tangent being instantaneously parallel to \vec{u} at every point¹¹. This idea provides some practical use since it allows streamlines to be considered solid boundaries in an inviscid flow. The superposition of known stream functions for fundamental flows is often used to compose more complex inviscid solutions with a variety of interpretations. As an

example, the stream functions for a uniform flow and doublet flow can be superposed to produce a new solution that is commonly interpreted as the flow past a circular cylinder. A *uniform flow* is the simplest form of potential flow, and its stream function is given in cylindrical coordinates as

$$\psi_{uniform} = Ur \sin \theta \quad (1-15)$$

Another simple potential flow, called a *source flow*, occurs when fluid flows radially outward from a point source¹³. The stream function for a source flow is represented as

$$\psi_{source} = \frac{m}{2\pi} \theta \quad (1-16)$$

where m is the volumetric flow rate emanating from the point source. When m is negative, the flow is directed radially inward and represents a similar potential flow called a *sink flow*. A *doublet flow* is obtained by allowing the distance, a , between a source and sink to approach zero, and its stream function is given by

$$\psi_{doublet} = \frac{-K \sin \theta}{r} \quad (1-17)$$

where K is a constant known as the “doublet strength”. The superposed stream function for a uniform flow and doublet flow can be determined by simply adding the stream functions together.

$$\psi_{cylinder} = \psi_{uniform} + \psi_{doublet} = Ur \sin \theta - \frac{K \sin \theta}{r}$$

$$\psi_{cylinder} = \frac{\sin \theta}{r} [Ur^2 - K] \quad (1-18)$$

The physical results of adding these potential flows together are depicted in Figure 1-8. The streamline passing through the stagnation points forms the circular boundary that can be interpreted as a 2-D cylinder in cross flow.

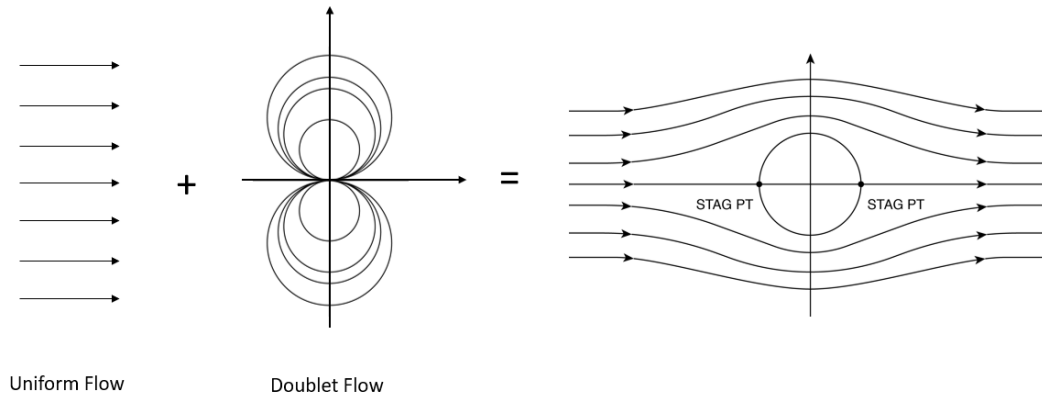


Figure 1-8: Superposition of Uniform and Doublet Potential Flows¹⁴.

Using equations (1-13) and (1-14), the velocity components for the combined flow can be obtained by differentiation of equation (1-18).

$$u_r = \frac{\cos \theta}{r^2} [Ur^2 - K] \quad (1-19)$$

$$u_\theta = -\frac{\sin \theta}{r^2} [Ur^2 - K] \quad (1-20)$$

The upstream C_P is of principle interest in the present work, and since potential flows are inviscid, Bernoulli's Equation may be used to obtain C_P in terms of the above velocity components. The resulting expression for C_P is given by equation (1-21).

$$C_p = 1 - \frac{\|\vec{u}\|^2}{U^2} \quad (1-21)$$

$$\|\vec{u}\|^2 = u_r^2 + u_\theta^2$$

In Figure 1-8, the superposed streamlines show that the stagnation streamline continues upstream and downstream of the cylinder. These sections of the stagnation streamline can be interpreted as a solid surface on which the upper half of the cylinder rests. Along the surface upstream of the fixed cylinder, $u_\theta = 0$ everywhere, and $\theta = \pi$. Applying these constraints to equations (1-13) and (1-14), the final expression for C_p along the solid boundary upstream of the cylinder can be obtained with equation (1-21).

$$C_p = \frac{1}{r^2} \left[2 - \frac{1}{r^2} \right] \quad (1-22)$$

By plotting C_p as a function of distance upstream from the stagnation point on the cylinder, the inviscid pressure disturbance upstream of the cylinder can be obtained. This method will be used to study the upstream pressure disturbance for excrescences of varying chord and half-widths as a precursor to the viscous computational model.

1.4 Computational Methods

Past Cal Poly student work with the BLDS housing geometry has relied on manufacturing many different models and running several separate wind tunnel tests. Wind tunnel testing is an essential part of aerodynamic design, and CFD methods cannot replace it. However, CFD is a powerful preliminary design tool when used properly. For the BLDS, a well-calibrated CFD model can be used to quickly alter the housing geometry

and understand how small changes will affect the flow structure without manufacturing multiple wind tunnel models. For this reason, one of the goals of the present work is to identify how well CFD can characterize the flow in the vicinity of small excrescences.

Like the continuity equation described in the previous section, another fundamental pillar in the analysis of fluid flow are the momentum-conservation equations known as the *Navier-Stokes Equations* (NS). The NS equations are a set of partial differential equations that describe the motion of viscous fluids, and they can be written in indicial notation as a single equation¹⁵. For a fluid of constant ρ and μ

$$\frac{\partial u_i}{\partial t} + \frac{\partial}{\partial x_j} (u_i u_j) = -\frac{1}{\rho} \frac{\partial p}{\partial x_i} + \nu \frac{\partial^2 u_i}{\partial x_j \partial x_j} \quad (1-23)$$

Reynolds decomposition refers to a method of separating fluid flow quantities into a mean value and a fluctuating value. When the above equations are time-averaged using Reynolds decomposition, the results are the *Reynolds-Averaged Navier-Stokes (RANS)* equations.

$$\frac{\partial \bar{u}_i}{\partial t} + \bar{u}_j \frac{\partial \bar{u}_i}{\partial x_j} = -\frac{1}{\rho} \frac{\partial \bar{p}}{\partial x_i} + \nu \frac{\partial^2 \bar{u}_i}{\partial x_j \partial x_j} - \frac{1}{\rho} \frac{\partial \tau_{ij}}{\partial x_j} \quad (1-24)$$

RANS modeling is the most common and widespread approach in industrial CFD applications¹⁶. The RANS equations alone provide for the components of *molecular* viscous stress, but most practical applications in aerodynamics involve turbulent flow, which introduces the idea of viscous stress due to *turbulent viscosity*. In the RANS

equations, the *Reynolds stress tensor*, τ_{ij} , incorporates these effects of turbulence on the mean stresses.

$$\tau_{ij} = \overline{u_i' u_j'} \quad (1-25)$$

In using the RANS equations to model turbulent flows, the problem of “closure” arises with the Reynolds stress tensor in the sense that it contains six additional independent unknowns that must be solved for¹⁵. The addition of unknown Reynolds stresses requires additional equations embodying what is called a *turbulence model*. The turbulence model used to close the RANS equations in this thesis is the Spalart-Allmaras (S-A) one-equation model.

The S-A turbulence model is a RANS approach that involves a single partial differential equation to solve for the turbulent kinematic (or “eddy”) viscosity. The S-A model was specifically derived in 1994 for use in aerodynamic applications involving wall-bounded systems¹⁷. The model includes several constant coefficients and semi-empirical intermediate functions, but because there is only one dynamic differential equation to solve, it is computationally much simpler than some other RANS turbulence models. For this thesis, all coefficients in the S-A model will be retained as their original default values¹⁷.

There are many commercial CFD codes that solve the RANS equations for turbulent fluid flow problems. For this thesis, Ansys FLUENT¹⁸ is used to solve the RANS equations using the S-A model. FLUENT is a general purpose CFD solver and post-

processing program that utilizes the finite-volume method. This solver was chosen for this application because it also allows for refinement or coarsening of a mesh based on the flow solution¹⁹ and is readily available for research activities through the Cal Poly Mechanical Engineering Department. Before the flow field quantities can be computed in FLUENT, the BLDS housing geometry and corresponding computational grid must be generated. In this thesis, Ansys ICEM CFD²⁰ is used to generate all 2-D and 3-D geometries and their corresponding meshes. ICEM is a well-established pre-processing program compatible with FLUENT and is used widely in industry for this purpose.

To consider a CFD model valid, the computed results must be compared to experimental measurements, observed flow phenomena, and be proven to agree reasonably well¹⁶. The present work includes experiments for direct comparison to the CFD solutions which will be discussed in detail in Chapter 2. The past student project work involving wake analysis⁸ provides ample estimates for the pressure drag on several different BLDS housing geometries without further experiments. A classic example of a small protuberance immersed in a turbulent boundary layer is the forward-facing step as depicted in Figure 1-9²¹. Like a forward-facing step, the BLDS housings are generally blunt with sharp corners (not considering the fairing), so it is expected that the computed flow over BLDS housing geometries will display many of the same features as the flow over a forward-facing step.

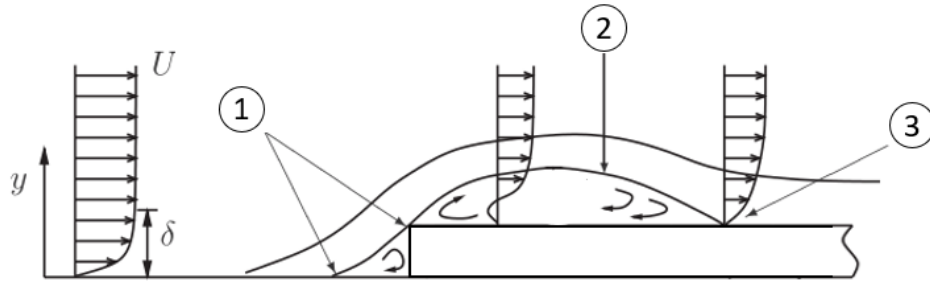


Figure 1-9: Flow Features Over a 2-D Forward-Facing Step. Adapted From Sherry Et.al, 200921.

Namely, the points of separation denoted by 1 in Figure 1-9 are expected to be observed in the CFD solutions and will be identified using plots of the skin friction coefficient, C_f . The region of recirculating flow at location 2 is expected to occur over the top of each excrescence and will be observed using C_f plots as well as particle pathlines in FLUENT. Finally, the flow may reattach somewhere along the flat top of each BLDS geometry as shown at 3. However, the BLDS housings have blunt trailing edges, so an additional region of separation, or wake, is expected to occur behind each excrescence⁵ as depicted in Figure 1-10 below.

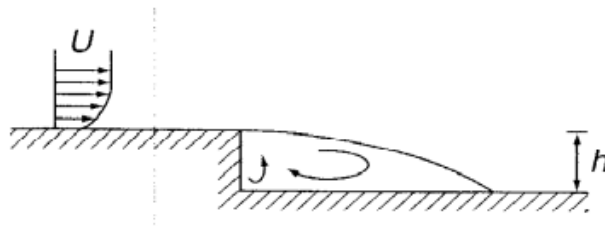


Figure 1-10: Flow Features Over a 2-D Backward-Facing Step. Adapted From White Fig. 6-3322.

There are two over-arching approaches for CFD computational grid generation: the structured mesh, and the unstructured mesh. Structured meshes often consist of orthogonal quadrilateral (2-D) or hexahedral (3-D) elements. Unstructured meshes have arbitrary structure consisting of non-orthogonal elements²³. The difference between a structured and unstructured mesh is depicted in Figure 1-11 for a 2-D airfoil.

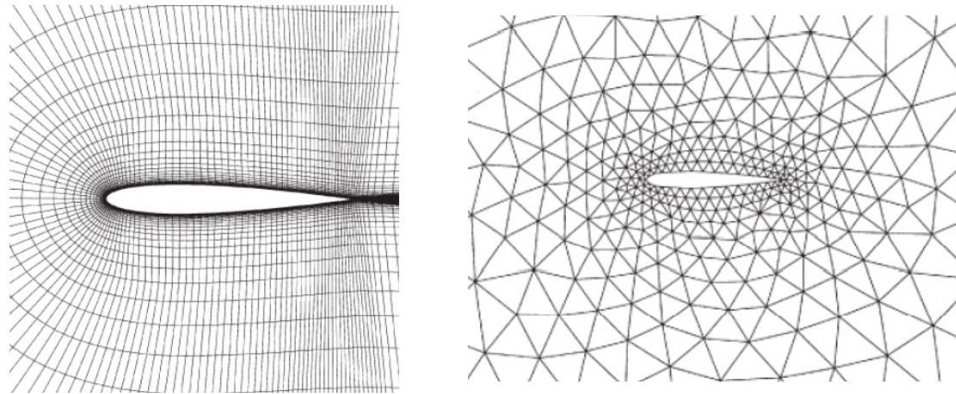


Figure 1-11: Structured (Left) & Unstructured (Right) 2-D Airfoil Mesh. From McLean Fig.

10.3.1¹⁶.

In general, unstructured meshes are used in situations where the solid bodies in the simulation have highly complex geometry. Due to the relative simplicity of BLDS housings, all meshes generated in the present work will be structured, multi-block grids. For simple flow problems, such as 2-D airfoil flow, structured grids fare much better than unstructured grids at producing an accurate solution¹⁶. The flow situation in this thesis does not include shocks, or any other compressibility effects, so the structured mesh approach will be sufficient for this work. A well-designed structured mesh typically leads to shorter calculation times, and fewer instances of numerical “noise”, or *grid dispersion* due to irregular element shapes and spacing²³.

In addition, it is important to understand and control the sources of error that can arise in a computational simulation. There are two main categories typically used to classify sources of error in computational simulations: modeling error and numerical error²⁴. Modeling errors are related to the simulation's inability to reproduce behavior observed in the real world. Modeling errors will be addressed in this thesis by comparing computed flow features to the expected behavior. Numerical errors are classified by three distinct types: round-off error, iteration error, and discretization error. Round-off error is the numerical error due to the finite number of significant digits used to store floating point numbers on digital computers²³. Using "double precision" on a 64-bit machine gives solutions with 15 significant digits²⁴ which reduces the round-off error. Iteration error arises when the governing equations are solved iteratively and is typically associated with using too few iterations. Iteration error is reduced by prescribing a low convergence tolerance for each governing equation. Discretization error is defined as the difference between the computed solution to the discretized equations (assuming zero round-off and iteration error) and the exact solution to the original (continuous) partial differential equations²⁴. All CFD solutions presented in this thesis utilize double precision and scaled residuals of 1×10^{-6} . Therefore, round-off error and iteration error are considered negligible, and the total error is expected to be driven by only discretization.

Discretization error can be driven towards zero by refining the mesh until the solution no longer depends on the grid size. The Journal of Fluids Engineering (JFE)²⁵ has standardized the practice of conducting Richardson extrapolation to provide an

estimate of the exact solution to be used for estimating the discretization error. The numerical uncertainty for solution parameters of interest is then reported as a *fine-grid convergence index* (GCI_{fine}) the calculation of which is well-established in the JFE Editorial Policy Statement on the Control of Numerical Accuracy²⁵. For this thesis, the GCI_{fine} , average apparent order, and difference between extrapolated and computed solutions will be presented to define the total numerical uncertainty in C_p .

Finally, an important aspect of CFD calibration for turbulent boundary layer flow is assessing the thickness and shape of the undisturbed boundary layer. To capture the undisturbed turbulent boundary layer as it appears directly at the leading edge of the BLDS housings, each mesh will be designed to include a solid boundary that exists beneath the BLDS. This approach will allow for the BLDS geometry to be turned “on or off” by adjusting its boundary conditions to *no-slip wall* or *flow-through* types²⁶. When the BLDS boundaries are flow-through, the boundary layer profile can be computed as if it grew on the flat surface without the BLDS present. This approach has been demonstrated with ICEM as a practical method for computing incremental drag due to small excrescences²⁶.

The objective of this thesis is to use Ansys ICEM CFD and FLUENT to model and compute air flow as it appears in the vicinity of BLDS housing geometries with the intent of capturing, and comparing, the upstream pressure disturbance and pressure drag incurred on the different BLDS housing geometries. In that, there are two main questions that drive the present work:

1. Can CFD methods accurately compute the flow near small excrescences like the BLDS?
2. How effective are the current BLDS housings at limiting pressure field disturbance and imposed pressure drag?

The general approach for addressing these driving questions will consist of the following distinct activities:

1. Conduct wind tunnel tests in Cal Poly's 2 x 2-foot wind tunnel with 2-D and 3-D BLDS housing models to obtain measurements of the upstream C_p (Chapter 2).
2. Calibrate ICEM mesh parameters and FLUENT computational case set-up in 2-D by comparing computed results to wind tunnel measurements (Chapter 3).
3. Extend calibrated 2-D geometry, mesh parameters, and case set-up to 3-D and compare FLUENT results to wind tunnel measurements (Chapter 4).
4. Examine 2-D and 3-D computed flow features and compare to classic principles (Chapters 3 and 4).
5. Explore how changing BLDS housing geometry alters the pressure disturbance in the vicinity of the excrescence and imposed pressure drag (Chapter 4).

2. EXPERIMENTAL PRELIMINARIES

Whenever a fluid flow simulation is created, it is important to compare the results against a wide range of experimental test cases. This identifies how physically accurate the solutions are likely to be and what kinds of biases to expect for different situations. This is often called *CFD validation* or less commonly, *CFD calibration*¹⁶. The wake analysis⁸ discussed in Chapter 1 provides reasonable estimates for the drag coefficients of different BLDS housings, therefore the experiments presented in this chapter are solely concerned with characterizing the upstream pressure disturbance induced by different BLDS housings. Upstream surface pressure data was collected in each experiment and used to compute upstream surface pressure coefficients to calibrate the FLUENT models. For the present work, four experiments were conducted in the Mechanical Engineering Fluids Lab's 2 x 2-foot wind tunnel to calibrate the CFD models. A diagram of the general test set-up is shown in Figure 2-1 below.

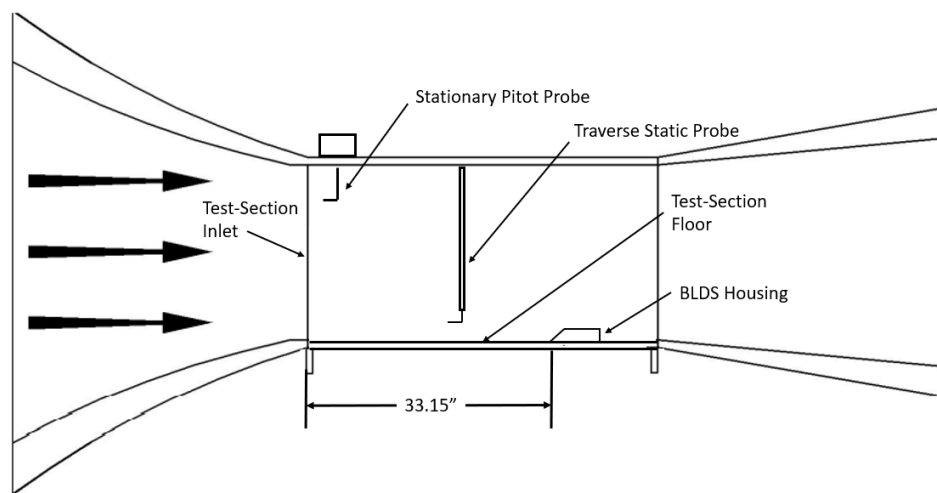


Figure 2-1: Diagram of BLDS Model in 2 x 2-Foot Wind Tunnel.

All wind tunnel models were positioned 33.15 inches aft of the test-section inlet making the local Reynolds number $Re_{x_{le}} \approx 2.18 \times 10^6$. The four test cases are listed in Table 2-1 below. For all test cases, the Mach number and Re/L are 0.12 and $7.90 \times 10^5 \text{ ft}^{-1}$, respectively. A rake measurement of the undisturbed boundary layer profile at the leading edge location ($x_{le} = 33.15$ inches) was also collected for comparison to the boundary layer computed in FLUENT.

Table 2-1: Experimental Cases

Test Case	Excrescence Evaluated	<i>Re</i> Based on Model Height Re_h
1	2-D Tall Model	9.88×10^4
2	2-D Short Model	4.69×10^4
3	3-D Enclosure	4.82×10^4
4	3-D Fairing	4.50×10^4

2.1 Two-Dimensional Experiments

To calibrate the two-dimensional (2-D) CFD models, a set of purely 2-D wind tunnel tests were conducted to determine the upstream surface pressure coefficients of two test objects. To enforce 2-D flow in the wind tunnel, the test objects were manufactured to have constant cross-section, and span the width of the 2-foot test-section. Two different model heights were manufactured with a cross section designed to resemble the classic BLDS ramped-front enclosure. Each model was cut on a table saw from a 2-foot-long piece of 2 x 4 wood to have a 45° ramp along its length, and all

frayed edges after cutting were sanded down. The 2-D wind tunnel models as positioned on the test-section floor and their critical dimensions are in Figure 2-2.

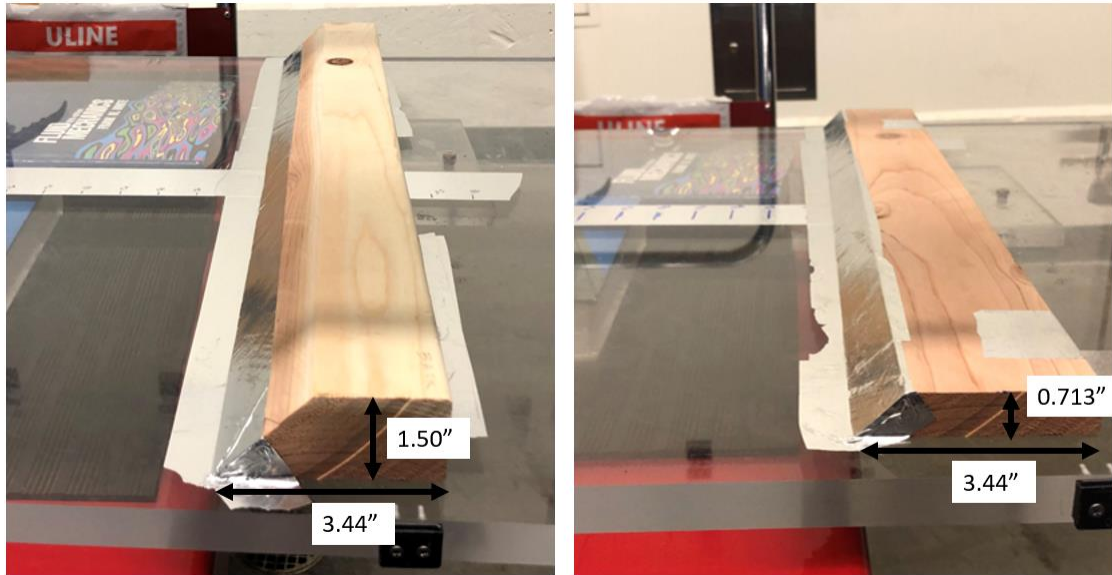


Figure 2-2: Tall (Left) and Short (Right) 2-D Wind Tunnel Models in 2 x 2-Foot Wind Tunnel.

Each model was secured to the test-section floor using 0.005-inch-thick aluminum foil tape. To aid in upstream distance measurement, a piece of tape marked with 1-inch increments leading away from the model leading edge was secured to the wind tunnel floor and used as the x -direction measurement scale for all experiments discussed in this chapter. The wind tunnel is equipped with a traverse Pitot-static probe that can be moved along the streamwise length (x -direction) of the test-section. The probe can also be raised and lowered along the height (y -direction) of the test-section, perpendicular to the direction of flow. A stationary Pitot probe was fitted through a slot on the upper test-section surface as shown in Figure 2-3. Once the model was secured, the traverse

probe was positioned at the center of the model port hole, approximately 12 inches above the test-section floor and 8 inches downstream of the test-section inlet.

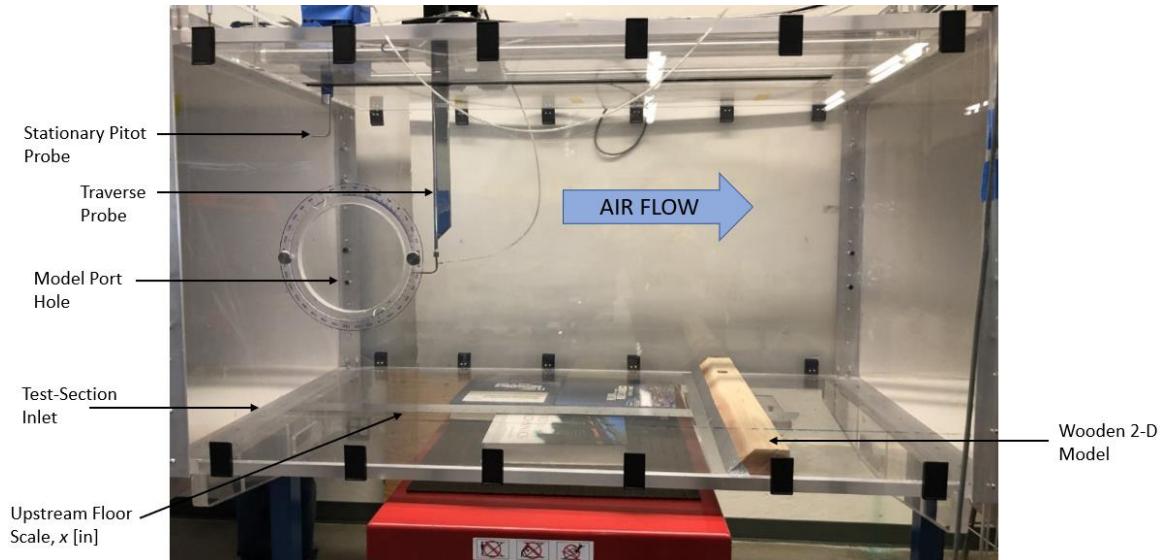


Figure 2-3: Wind Tunnel Test Set-Up Used for 2-D Experiments.

The ambient pressure and temperature in the lab were recorded before the wind tunnel was turned on. For all experiments, the nominal room pressure and temperature were approximately 14.64 psia and 71°F, respectively.

Upstream pressures were measured as a total-static pressure differential using a Setra 239 pressure transducer with a range of 0-15 inH₂O. The pressure transducer was powered by a constant voltage power supply and read using a Fluke 179 digital multimeter. The data was averaged over a duration of 5-10 seconds using the multimeter at each measurement location. With the static traverse probe at the model port, the wind-off tare was recorded to be approximately -0.013 VDC, then the wind tunnel was powered on at blower drive frequency of 50 Hz (approximately 89 mph).

Between all test cases in this thesis, the wind-off tare ranged from -0.011 VDC to -0.013 VDC. A reference total-static value was measured at the model port once the wind tunnel reached 50 Hz. The center of the model port was chosen as the reference pressure location because it is well outside the boundary layer growing on any of the test-section walls. Once the reference pressure was collected, the traverse probe was lowered until it was roughly 0.25 inches above the test-section floor as depicted in Figure 2-4. During all tests, the static pressure on the traversing probe was read relative to the total pressure collected from the stationary Pitot probe.

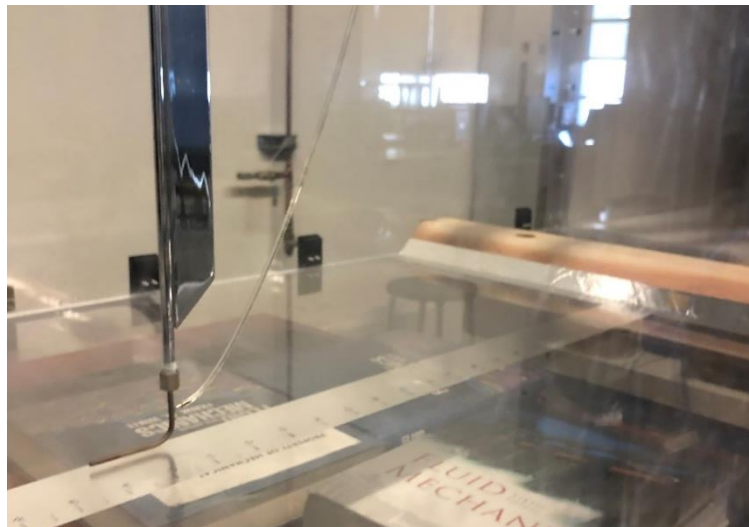


Figure 2-4: Static Traverse Probe 0.25 Inches Above the Test-Section Floor.

Differential pressure measurements were taken along the center of the test-section floor using the x-direction floor scale upstream of each model. Care was taken to ensure that the static port on the static traverse probe was aligned with the tick mark on the floor scale at each measurement location as shown in Figure 2-5.

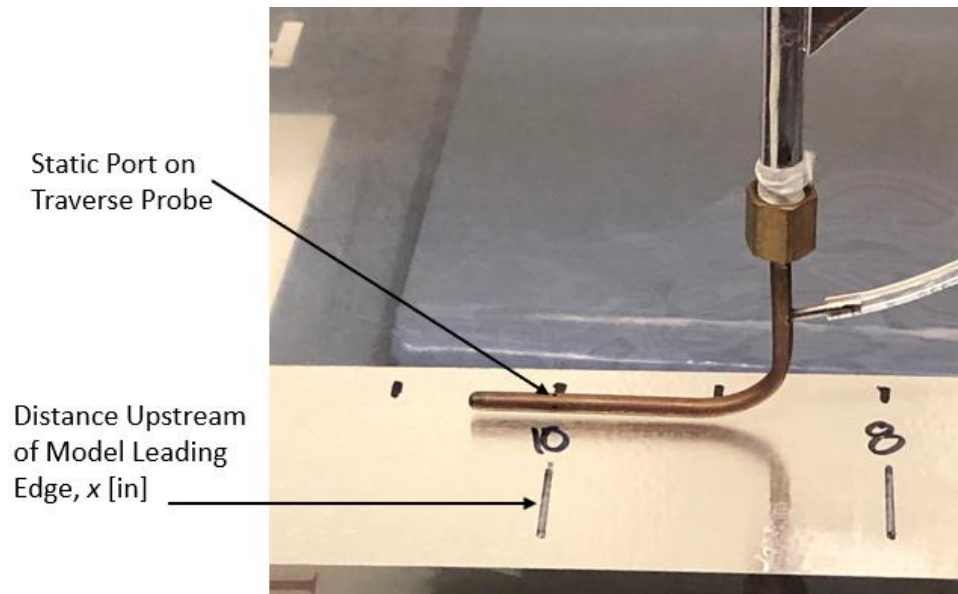


Figure 2-5: Traverse Probe Aligned With Upstream Floor Scale.

The wind-off tare was subtracted from each total-static measurement and the data was converted from the measured units of VDC to inH₂O. The total surface static pressure distribution is presented in Figure 2-6 for Test 2 (short model) only. The raw data collected for Tests 1 and 2 can be seen in Appendix B.

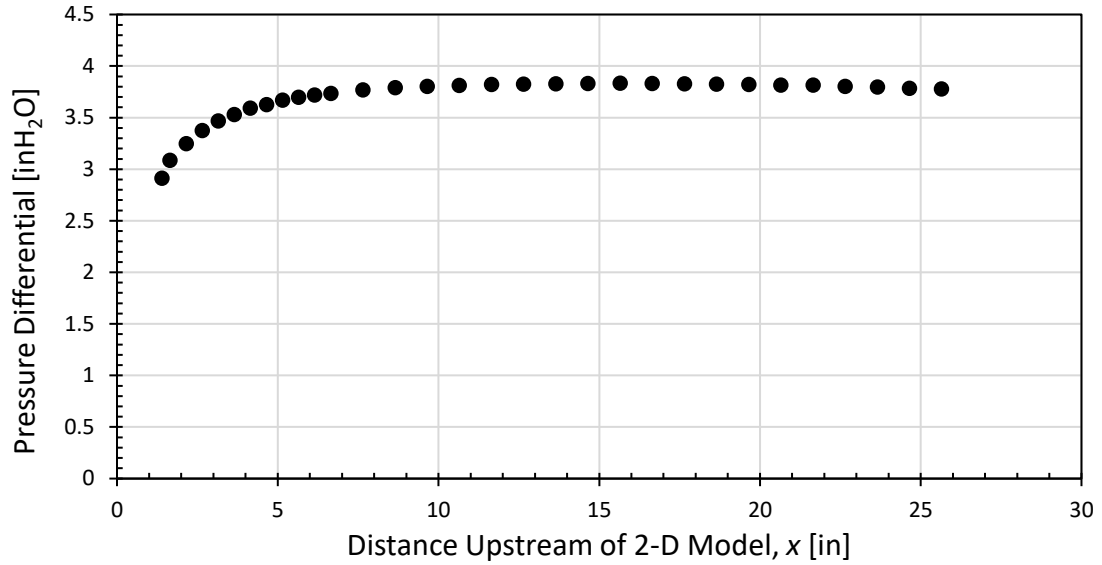


Figure 2-6: Total-Static Pressure as a Function of Upstream Distance, x , for Test 2 (Short Model).

The test set-up affords only differential pressure measurements, so the pressure coefficients were computed using equation (2-1) below.

$$C_p = \frac{(p_0 - p)_{ref} - (p_0 - p)_x}{(p_0 - p)_{ref}} \quad (2-1)$$

The subscript *ref* denotes the differential pressure measurement taken at the model port, and the subscript x , refers to the measurement taken near the surface at each x location. The total pressure, p_0 , comes from the stationary Pitot probe and is constant everywhere in the wind tunnel, so the numerator in equation (2-1) reduces to $p_x - p_{ref}$. Using Bernoulli's Principle, the denominator in equation (2-1) can be represented as the reference dynamic pressure measured at the model port, q_{ref} , and the pressure coefficient becomes

$$C_p = \frac{p_x - p_{ref}}{q_{ref}} \quad (2-2)$$

where p_x is the static pressure at any x -location along the wind tunnel floor and p_{ref} is the reference static pressure measured from the model port. Figure 2-7 shows the pressure coefficient at each x -location.

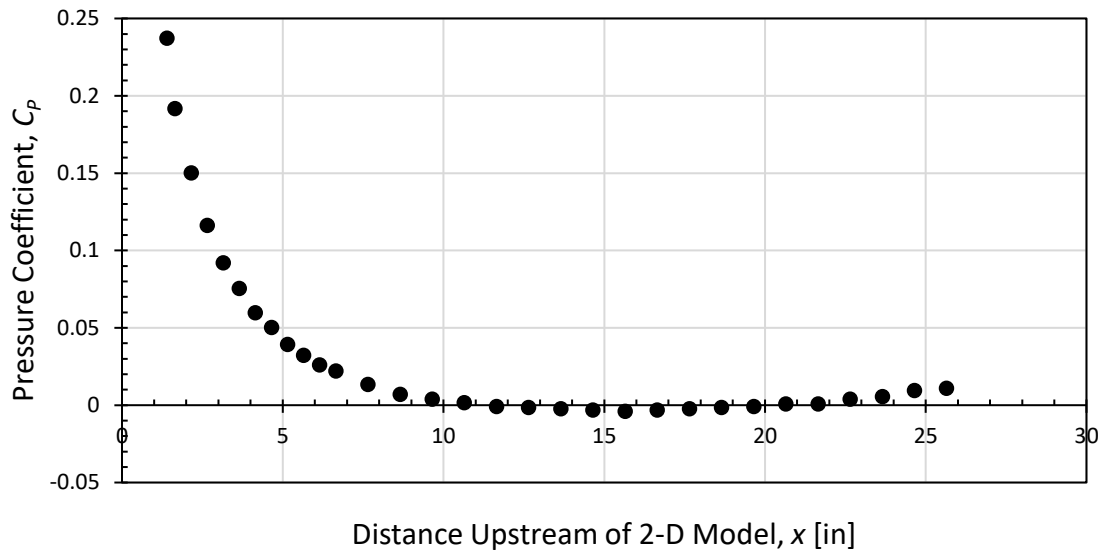


Figure 2-7: Pressure Coefficients as a Function of Upstream Distance, x , for Test 2 (Short Model).

The focus of the present thesis is to characterize how the pressure is disturbed upstream of the excrescence, and ultimately to compare the disturbance to that of different excrescence geometries. Therefore, a more appropriate independent variable for Figure 2-7 would be the distance upstream of the model leading edge normalized by the model height. Normalizing the independent variable by the height of each model allows for the upstream pressure coefficients for models of different heights to be

directly compared on the same axes. Figure 2-8 shows C_p plotted as a function of normalized distance upstream of the model leading edge, x/h .

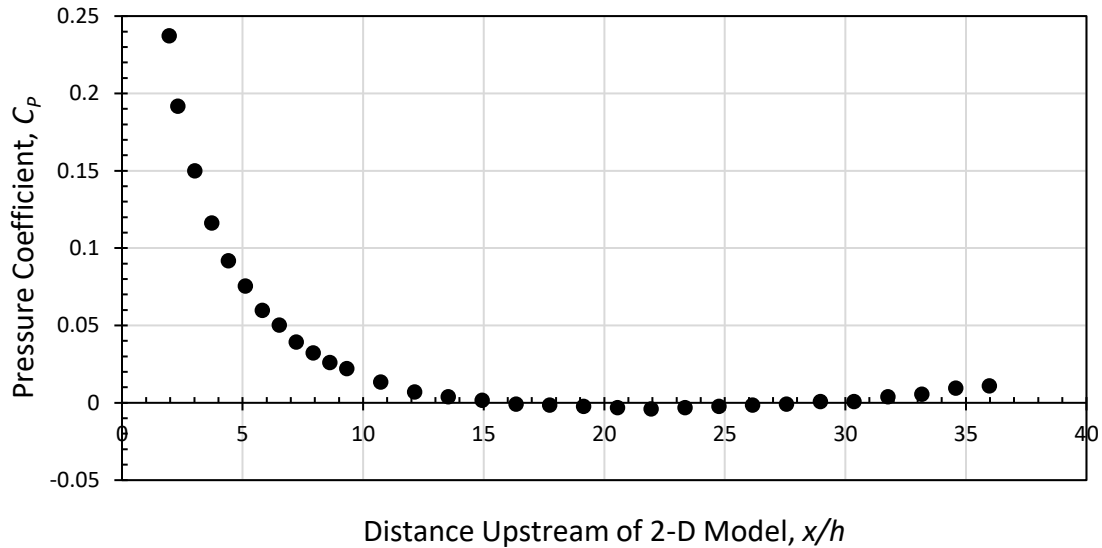


Figure 2-8: Surface C_p as a Function of x/h for 2-D Wind Tunnel Test 2 (Short Model).

It became apparent that the wind tunnel may possess inherent biases that affected the results in Figure 2-7. The pressure coefficient should be near zero until the flow is disrupted by the model at which point it should increase. The negative pressure coefficients at about $16 < x/h < 28$ in Figure 2-8 indicate an increase in centerline flow velocity that is expected due to negative buoyancy effects in the wind tunnel²⁷. To remove the bias from the results, the surface pressure coefficients along the floor of the wind tunnel *without* the models were collected at 50 Hz. The empty tunnel pressure coefficients are shown in Figure 2-9 below, and the raw data collected from the empty tunnel can be seen in Appendix C.

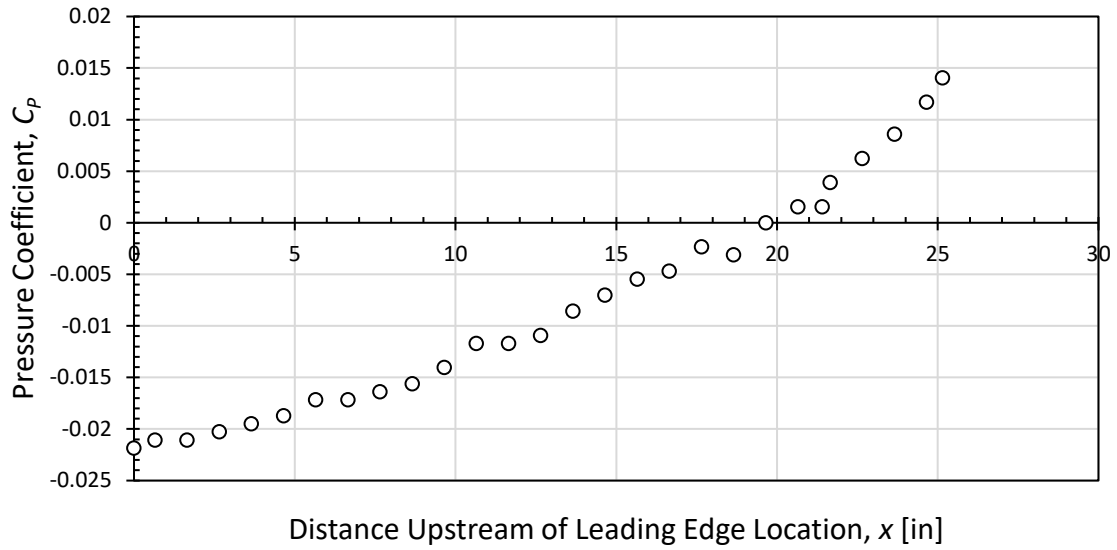


Figure 2-9: Empty Tunnel C_p as a Function of Upstream Distance, x , at 50 Hz.

The empty tunnel pressure coefficients were subtracted from the pressure coefficients shown in Figure 2-8 at each upstream x -location producing corrected pressure coefficients. The corrected results are compared to the uncorrected results for Test 2 (short model) in Figure 2-10.

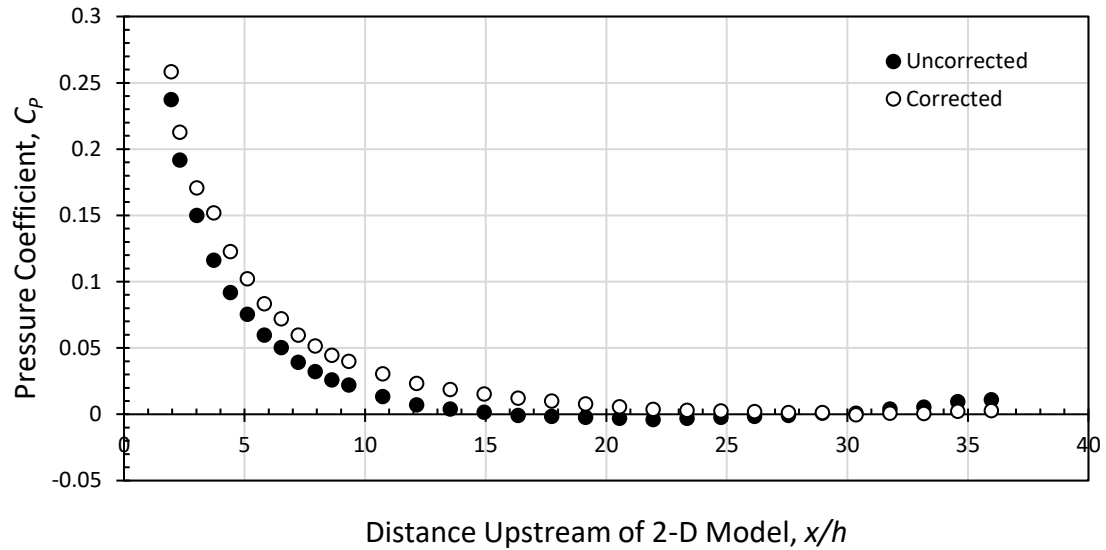


Figure 2-10: Corrected and Uncorrected C_p as a Function of x/h for Test 2 (Short Model).

For all experiments conducted in the Cal Poly 2 x 2-foot wind tunnel, the same empty tunnel data was used to correct the measured pressure coefficients. The corrected results from Tests 1 and 2 are compared to each other in Figure 2-11. The corrected C_p data for both cases presented in Figure 2-11 is compared to the FLUENT results in Chapter 3.

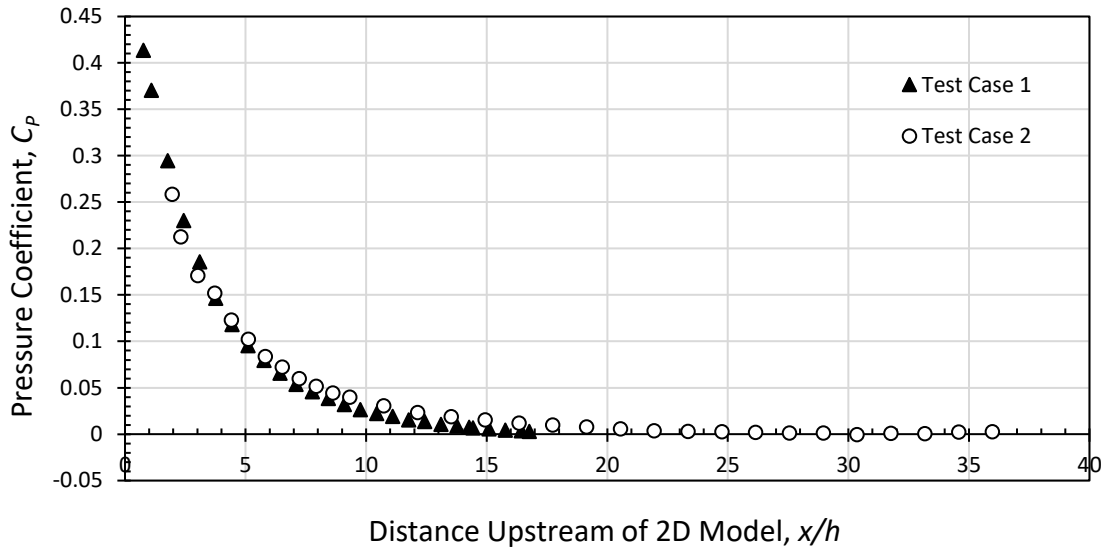


Figure 2-11: Corrected C_p as a Function of x/h for Tests 1 (Tall Model) and 2 (Short Model).

There is a second bias that cannot be corrected out by collecting and subtracting empty tunnel pressures. The wind tunnel used in these experiments has a test-section with constant cross-sectional area of 4 ft². Therefore, the presence of a model in the test-section reduces the area through which air can flow and, by continuity and Bernoulli's equation, causes a local increase in air velocity over the model. This increase in velocity is called *solid blockage* and is typically a function of model cross-sectional area²⁷. A separate correction would have to be applied to remove any biases in the experimental data caused by solid blockage, but no such correction is considered for the present work. Instead, the ability of FLUENT to simulate blockage effects will be explored in more detail in Chapter 3.

Finally, equation (2-1) shows that C_p depends on three separate differential pressure measurements. As with any measurement scheme, these three measured quantities provide another source of uncertainty to any calculations involving their use. As such, it was necessary to quantify the propagated uncertainty involved with computing C_p from p_x , p_{ref} and q_{ref} . For this work, a general uncertainty propagation approach was taken involving partial differentiation of equation (2-2) with respect to each measured quantity, followed by a root sum square of the contribution from each measured quantity. The uncertainty in experimental C_p values was found to be approximately ± 0.005 based on the systematic uncertainty contributions from the Setra 239 transducer, Fluke 179 multimeter, and pitot-static probes. The propagated uncertainty in the x/h values was found by the same method to be ± 0.1 in. These uncertainty estimates apply to all measured pressure disturbance values in this thesis.

2.2 Three-Dimensional Experiments

Test Cases 3 and 4 were conducted to collect upstream pressure disturbance data to calibrate the three-dimensional (3-D) blunt and streamlined CFD models. The experimental method used for the 3-D tests was largely the same as the method described above for the 2-D test cases. Nuances and experimental results are discussed and presented in the sections that follow.

2.2.1 Blunt Body Experiment

The aluminum ramped-front enclosure designed to house BLDS electronics was selected for the blunt body experiment². The enclosure includes a 45° ramp at the leading edge and a blunt trailing edge as depicted in Figure 2-12.

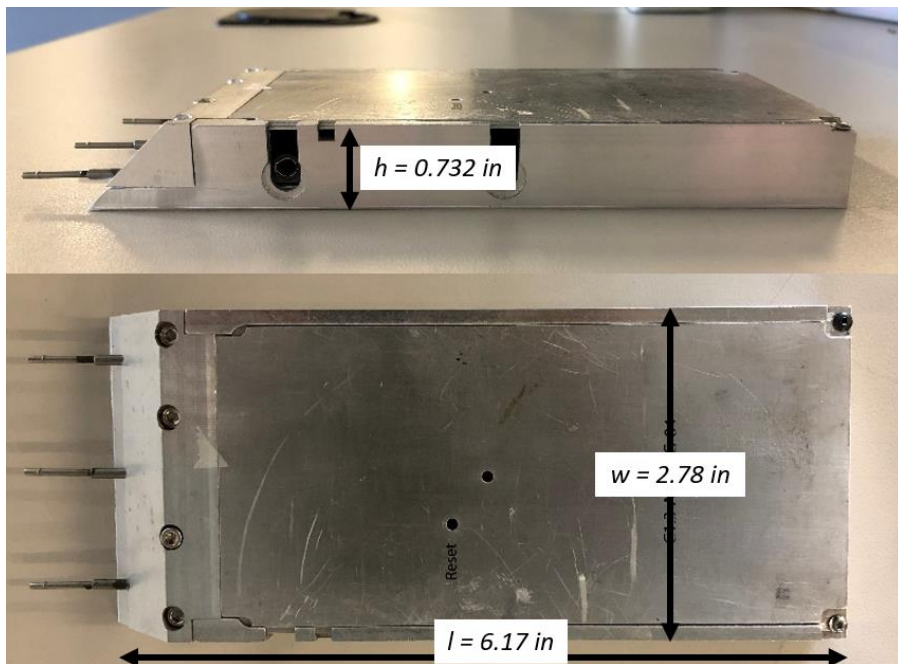


Figure 2-12: BLDS Ramped-Front Enclosure With Critical Dimensions.

The enclosure was secured 33.15 inches downstream of the test-section inlet, providing about 20 inches of upstream travel for the static traverse probe. The wind tunnel was run at a blower drive frequency of 50 Hz and Figure 2-13 shows the test set-up.

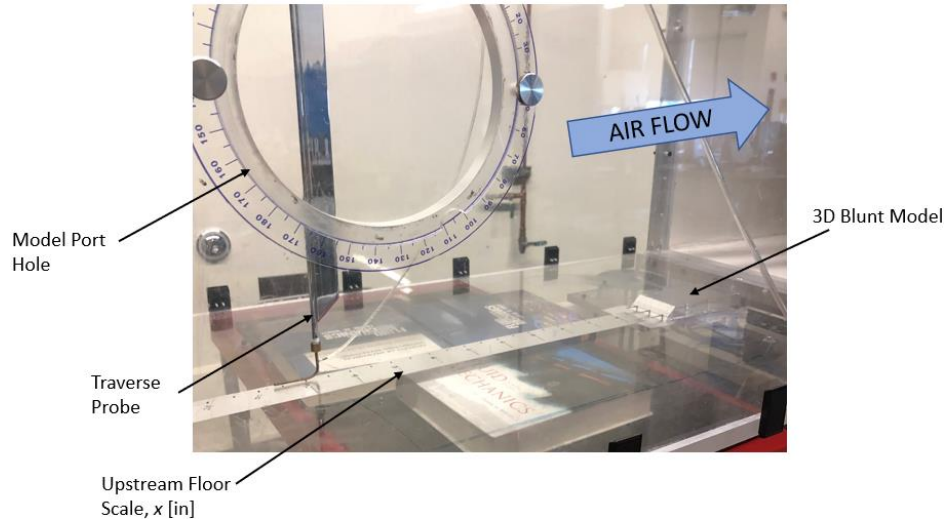


Figure 2-13: Wind Tunnel Test Set-Up Used for 3-D Blunt Body Experiment.

The surface pressure coefficients were corrected with the same empty tunnel data presented previously and are plotted as a function of normalized upstream distance in Figure 2-14. The raw pressure differential data can be seen in Appendix D.

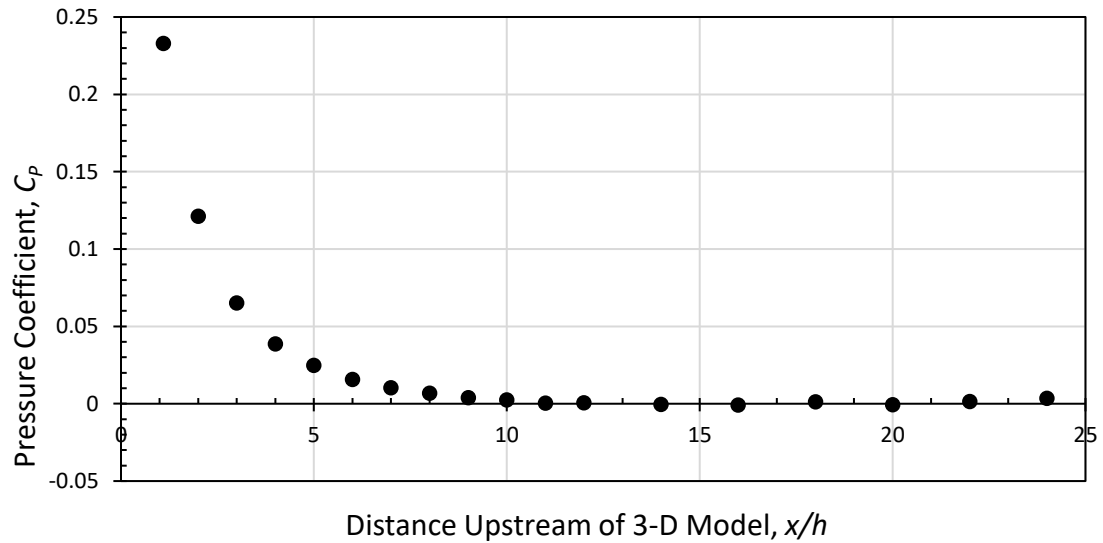


Figure 2-14: Upstream C_p as a Function of x/h for Test 3 (Ramped-Front Enclosure).

2.2.2 Streamlined Body Experiment

A half-scale version of the BLDS Fairing previously used by other student project teams⁷ was used for the streamlined body experiment. The full-scale fairing was developed at the request of Boeing and used for BLDS applications on the 2018 ecoDeomstrator flight test⁴. The 3-D printed half-scale version used for the present experiment is depicted in Figure 2-15.

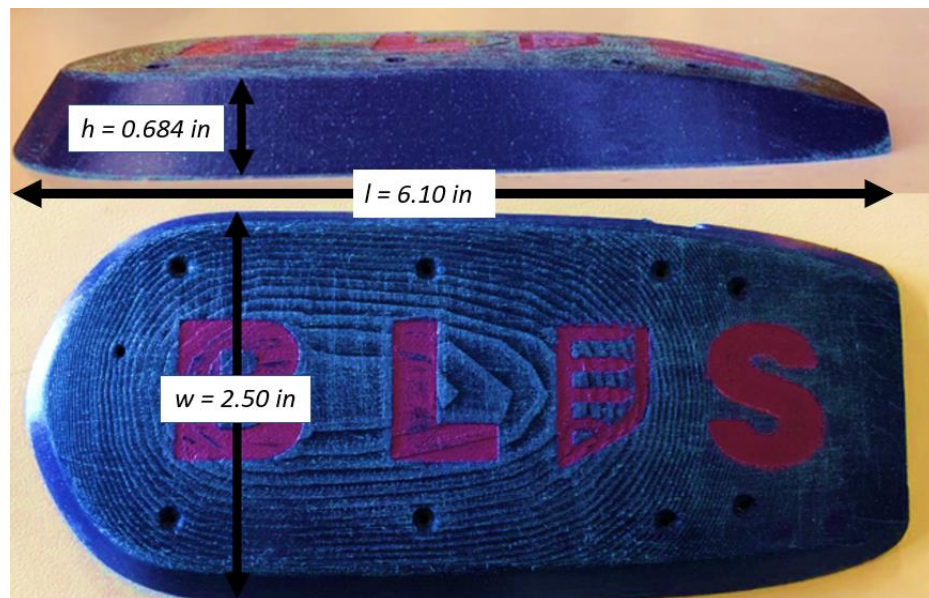


Figure 2-15: BLDS Half-Scale Fairing With Critical Dimensions.

The half-scale fairing was mounted with the tip of its nose located 33.15 inches downstream of the test-section inlet. As in the blunt body experiment, the wind tunnel was run at a blower drive frequency of 50 Hz and Figure 2-16 shows the test set-up.

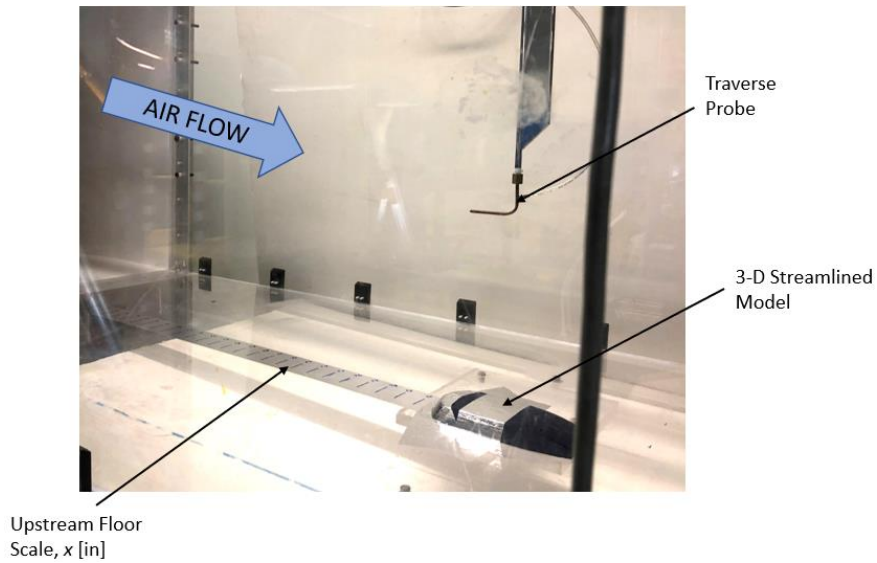


Figure 2-16: Wind Tunnel Test Set-Up Used for 3-D Streamlined Body Experiment.

The surface pressure coefficients were corrected with the same empty tunnel data presented previously and are plotted as a function of x/h in Figure 2-17. The raw pressure differential data can be seen in Appendix D. The pressure coefficients for each 3-D model are compared to each other in Figure 2-18.

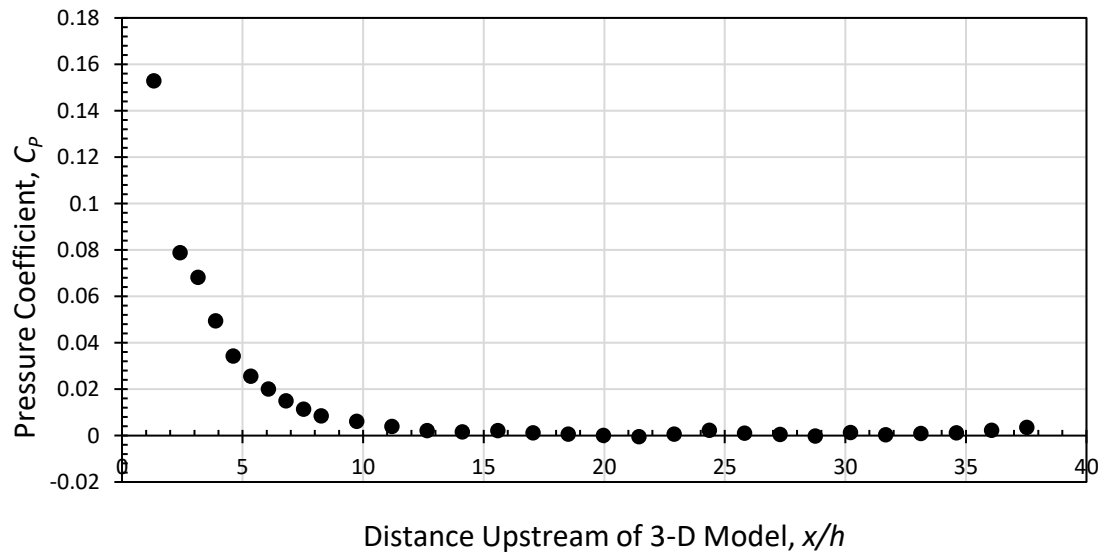


Figure 2-17: Upstream C_p as a Function of x/h for Test 4 (Half-Scale Fairing).

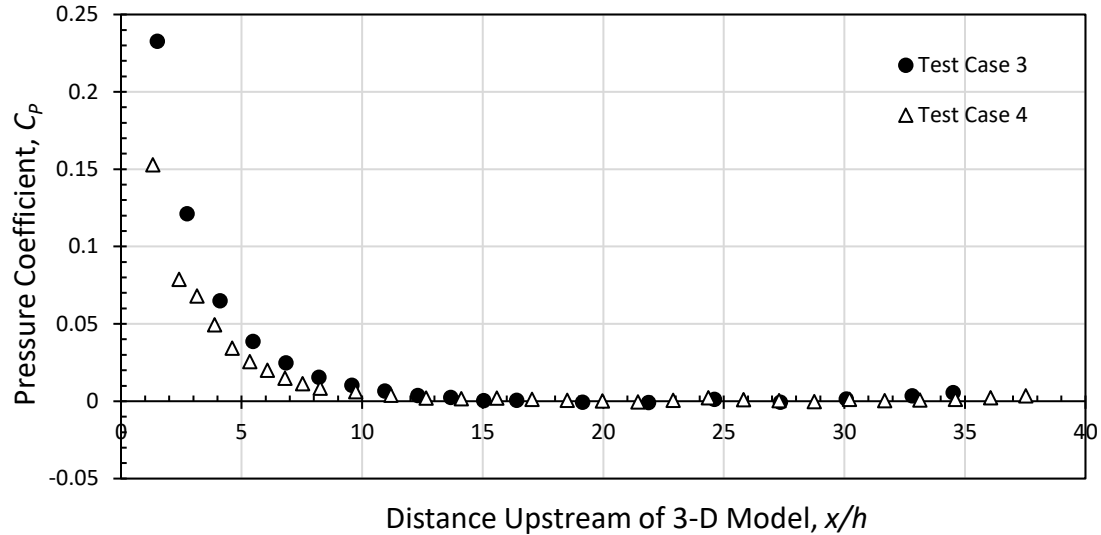


Figure 2-18: Corrected Upstream C_p Versus x/h for Tests 3 (Ramped-Front Enclosure) and 4 (Half-Scale Fairing).

2.3 Boundary Layer Measurement

In addition to the specific excrescence test cases, it was desired to measure an undisturbed local boundary layer profile at the model leading edge. The purpose of this measurement was to compare the turbulent boundary layer computed in FLUENT to the real boundary layer growing on the floor of the wind tunnel. A boundary layer *rake* is a tool often employed in the measurement of boundary layers on aerodynamic surfaces, and it consists of an array of total pressure probes fixed to a support². The total pressure probe rake array used in this experiment is depicted in Figure 2-19.

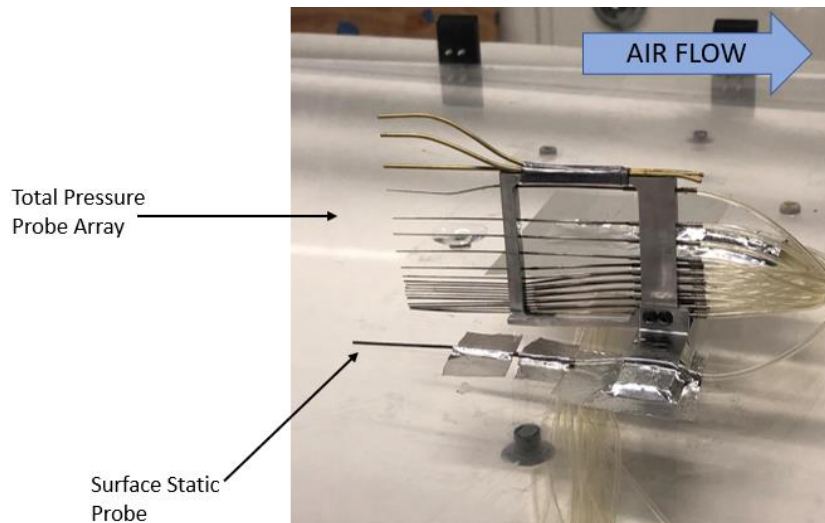


Figure 2-19: Test Set-Up for Undisturbed Boundary Layer Profile Measurement.

Using the set-up shown in Figure 2-19, measurements of the Pitot tube pressures for each rake tube were recorded using the same pressure measurement equipment described in section 2.1. The wind tunnel was run at a blower drive frequency of 50 Hz. The static pressure was collected using a surface static probe, or Sproston-Goksel probe²⁸, that was secured to the wind tunnel floor using aluminum foil tape. The distance from the floor of the wind tunnel to the midpoint of each tube inlet was carefully measured and recorded. The raw pressure differential data collected from the rake at each tube location can be seen in Appendix E. The ambient pressure and temperature were also recorded and used to determine the air density and viscosity for the conditions on the day of the measurement. Bernoulli's principle and the air density were then used to compute the streamwise velocity at each rake tube height. The boundary layer thickness, δ , was determined to be approximately 0.89 inches (0.023 m), or the height at which the pressure differential measurements became nearly constant.

The free stream velocity outside the boundary layer, U , was determined to be 39.6 m/s.

The nondimensionalized velocity profile from the rake is shown in Figure 2-20 below.

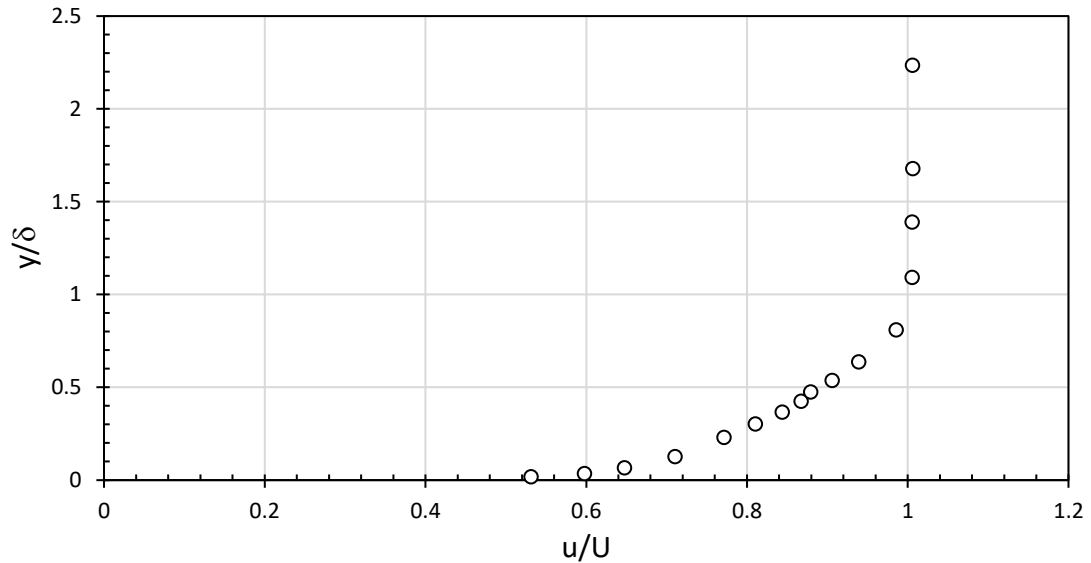


Figure 2-20: Velocity Profile Taken 33.15 Inches Downstream of the Test-Section Inlet.

The velocity profile in Figure 2-20 is that of a fully turbulent boundary layer in that the first data point collected 0.016 inches from the floor of the wind tunnel was already 52% of the free stream velocity. This suggests that the boundary layer is fully turbulent at the leading edge of each model for a blower drive frequency of 50 Hz. It was important to determine the real flow regime of the boundary layer at the leading edge of each excrescence to ensure the FLUENT simulation will be appropriately representing the air flow. This will be discussed in more detail in the following chapters. Finally, integral boundary layer parameters were computed from the discrete profile data using trapezoidal approximation and are shown in Table 2-2 below.

Table 2-2: Boundary Layer Parameters Computed From Collected Profile Data

Free stream Velocity	Boundary Layer Thickness	Displacement Thickness	Momentum Thickness	Shape Factor
U [m/s]	δ [in]	δ^* [in]	θ_m [in]	H
39.6	0.89	0.13	0.09	1.4

3. 2-D CFD CASES AND CALIBRATION

To produce a high-fidelity 3-D CFD model, it is best practice to begin designing the model in two dimensions, then extend the domain into three dimensions only after details of the mesh and flow features have been proven to produce reasonable results in 2-D²³. The 2-D results from experiments discussed in Chapter 2 are used in the following sections to assess the validity of 2-D CFD models created with ICEM and FLUENT. This chapter will detail the design of the 2-D computational domain in ICEM, the case set-up parameters that were used in the FLUENT simulations, and the comparison between the experimental upstream pressure disturbance and results from CFD. The viscous results from FLUENT will also be compared to an inviscid analysis done with superposition of potential flows.

3.1 2-D Inviscid Analysis

This thesis aims to characterize upstream pressure disturbances for small excrescences as they are positioned on flat walls in *viscous* flow. A natural preliminary step in analyzing any viscous flow is to conduct an *inviscid* analysis to understand the basic flow structure. For the present work, a *Rankine oval*¹¹ was generated using potential flow theory with the superposition of a uniform flow, source flow, and sink flow. When the sink flow is located directly downstream of the source flow, and given the same magnitude as the source, a streamline pattern with one closed, oval-shaped streamline is obtained. The MATLAB version of the *Ideal Flow Machine* (IFM), developed

by Dr. William Devenport²⁹ at Virginia Polytechnic Institute and State University was used to create a schematic of a generic Rankine oval potential flow.

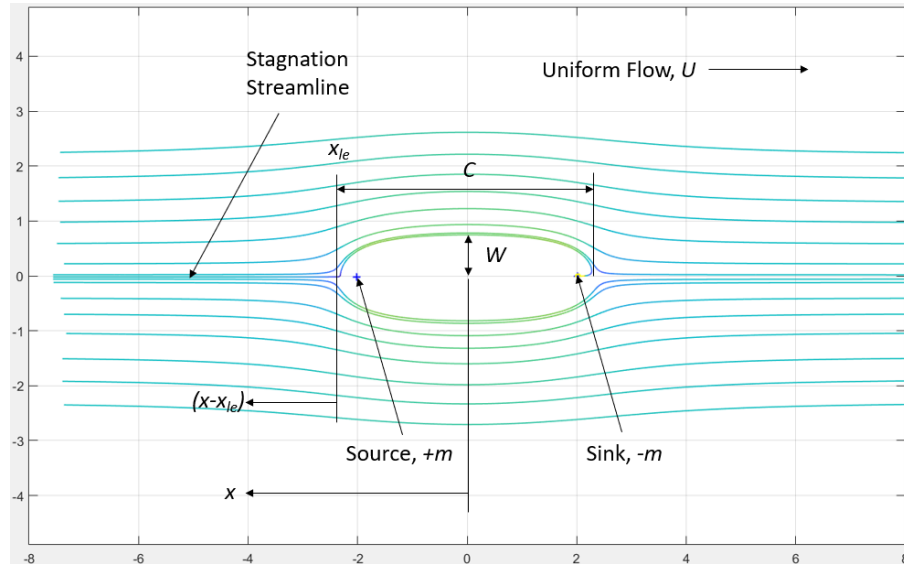


Figure 3-1: Generic Rankine Oval Potential Flow Created in IFM²⁹.

There are many useful interpretations for potential flow solutions like the one shown in Figure 3-1. For this inviscid analysis, the oval region was first interpreted as a 2-D body in cross flow, then a solid “bump” on an impermeable flat surface defined by the stagnation streamline. A MATLAB program was written to compute the pressure coefficients along the stagnation streamline for Rankine ovals of different chord to half-width (C/W) ratios. The MATLAB scripts for all inviscid analyses in this thesis can be seen in Appendix F. Interpreting the potential flow as a 2-D oval in cross flow, the inviscid solution was compared to a past Cal Poly student experiment using 2-D Rankine oval models in the 2 x 2-foot wind tunnel³⁰. In the past experiment, pressure measurements were taken along the upstream centerline of the wind tunnel as depicted in Figure 3-2.



Figure 3-2: Rankine Oval Pressure Disturbance Experiment. Private Communication, 2014³⁰.

The MATLAB program was used to compute the pressure coefficients along the stagnation streamline for a circular cylinder, and Rankine ovals with equivalent C/W ratios seen in the experiment. The inviscid analysis is compared to the experimental measurements in Figure 3-3.

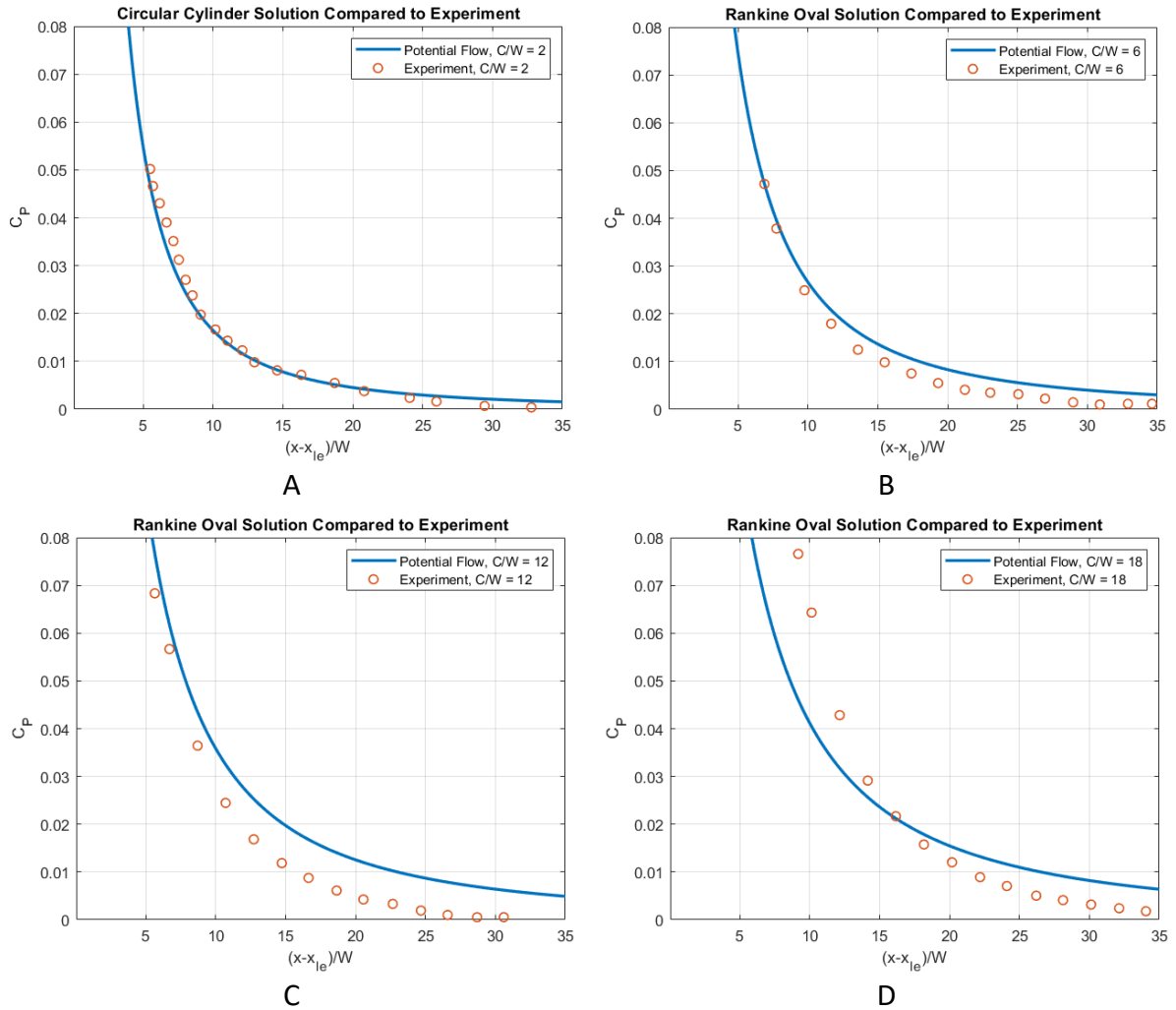


Figure 3-3: Potential Flow Analysis Compared to Past Experimental C_p Measurements.

For chord to half-width ratios between 2-6, the inviscid solution is a reasonable approximation for the experimental upstream pressure disturbance. Specifically, Figure 3-3A shows that the experimental C_p values for the 2-D circular cylinder are essentially the same as those from the potential flow solution. Likewise, Figure 3-3B shows that for an oval with $C/W = 6$, the difference in C_p between the experiment and analysis is no more than about 0.003. However, the inviscid solution becomes a less reliable estimate of the upstream centerline pressure disturbance for larger C/W ratios.

The 2-D experimental models discussed in Chapter 2 have chord to half-width ratios of 2.33 and 4.91 for the tall and short models respectively where the chord and width are defined as shown in Figure 3-4.

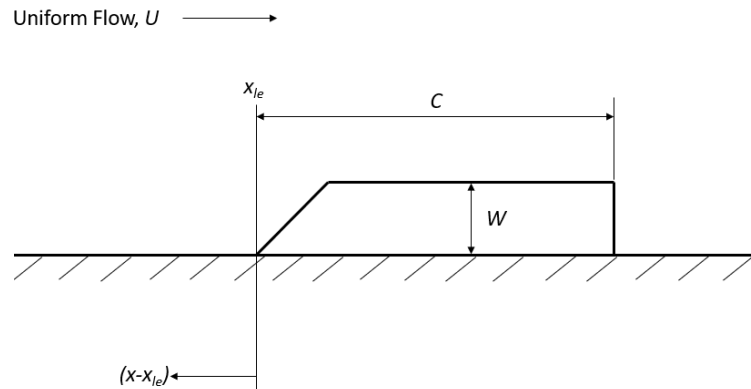


Figure 3-4: Schematic of 2-D Wind Tunnel Model for Comparison to Inviscid Analysis.

Since these wind tunnel models have C/W ratios between 2-6, it is expected that the 2-D experimental results be well matched by the inviscid solution. Interpreting the Rankine oval potential flow as that of a solid bump on a flat surface, the MATLAB code was used to produce Rankine ovals of $C/W = 2.33$ and $C/W = 4.91$. The computed upstream surface pressure coefficients are compared to the experimental measurements in Figures 3-5 and 3-6.

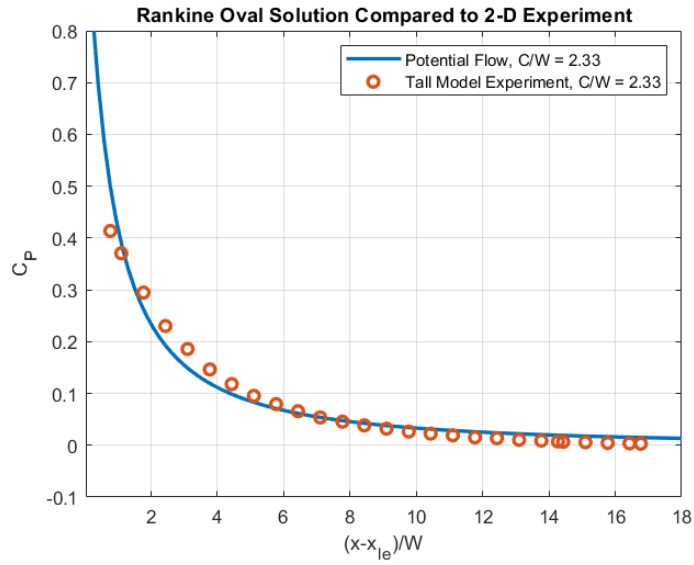


Figure 3-5: C_p From Tall ($h = 1.50$ in) 2-D Wind Tunnel Experiment Compared to Inviscid Analysis.

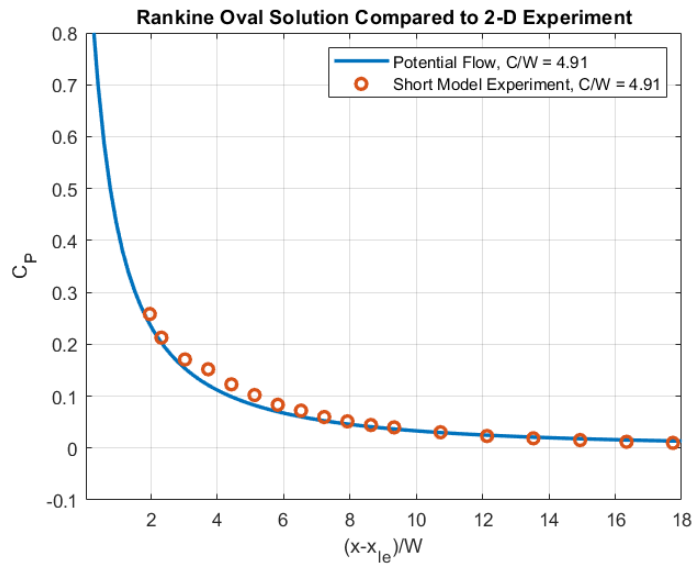


Figure 3-6: C_p From Short ($h = 0.713$ in) 2-D Wind Tunnel Experiment Compared to Inviscid Analysis.

As expected, the experimental results are well matched by the inviscid solution, especially far upstream of each model nose. The free stream C_p curves in Figure 3-3 show that the inviscid solution has better agreement when bodies have smaller C/W . However, the surface C_p curves in Figures 3-5 and 3-6 show slightly better agreement for the larger C/W . In addition, the experimental C_p measurements “lift up” above the inviscid solution on approach to the nose of the body, which is likely due to the viscosity present in the real flow. Since potential flows are inviscid, irrotational, and incompressible, there is no boundary layer present in the analytical solution. However, in the experiment a boundary layer exists along the wind tunnel floor and solid surfaces of the excrescence. The boundary layer appears to the oncoming flow as a solid boundary that displaces the streamlines producing a local deceleration that in turn increases the local value of C_p . This behavior could also be explained by a small region of separated flow upstream of the model. Upstream separation will be explored in more detail in section 3.3.

In summary, the inviscid analysis shows that for models of this scale ($C/W = 2-6$), potential flow theory gives a good estimate of the actual upstream pressure disturbance. Only minimal effects of viscosity are seen near the nose of each 2-D wind tunnel model from Chapter 2. In section 3.3, the 2-D CFD solution will be compared to the inviscid MATLAB analysis to assess the ability of FLUENT to accurately incorporate viscous effects in the simulated flow. The expectation is that the observations for the inviscid solution compared to the experiments will be replicated by the viscous CFD solution.

3.2 2-D Model Design and Case Set-Up

The 2-D computational domain was created in Ansys ICEM CFD which is a commercial meshing package widely used in the aerospace industry, and readily available through the Cal Poly Mechanical Engineering Department. Once the excrescence geometry and associated mesh were produced in ICEM, the mesh was output to Ansys FLUENT where the flow was solved using the RANS equations, and S-A turbulence model. In particular, the 2-D test objects discussed in Chapter 2 were directly modelled in a wall-bounded domain to represent the wind tunnel, and flow parameters were set to mimic air flow in the test section. The results from these “bounded” models were compared to the experimental data to validate the mesh and FLUENT case set-up. After achieving reasonable model validation, the bounded domain was altered to represent the same excrescence scenario in “free-air” flow. This section details the design process for the 2-D structured meshes and fluid flow parameters used in the FLUENT case set-up.

3.2.1 2-D Model Design in ICEM CFD

Several different meshes will be discussed in this chapter, and Table 3-1 lays out identifiers that will be used to distinguish each domain and mesh type. As an example, a mesh titled “TB” represents a mesh created for the tall 2-D model whose boundary conditions (BC’s) represent the wall-bounded 2 x 2-foot wind tunnel test section.

Table 3-1: 2-D Domain/Mesh Identifiers

Domain/Mesh Identifier	Description
T	2-D domain used to simulate tall model positioned on a flat wall
S	2-D domain used to simulate the short model positioned on a flat wall
A	Mesh with free-air dimensions and BC's
B	Mesh with wall-bounded dimensions and BC's
M	Mesh used for grid independence study
H	Mesh used to optimize the domain height

The 2-D geometry was developed using measurements taken from the 2-D wind tunnel models discussed in Chapter 2 and recorded using ICEM's replay control feature for later automation. The first model was created manually with the ICEM user interface using points, curves, and a partitioning method called *blocking*. The points and curves created for a domain meant to represent the tall 2-D model in the 2 x 2-foot wind tunnel and critical dimensions are shown in Figure 3-7.

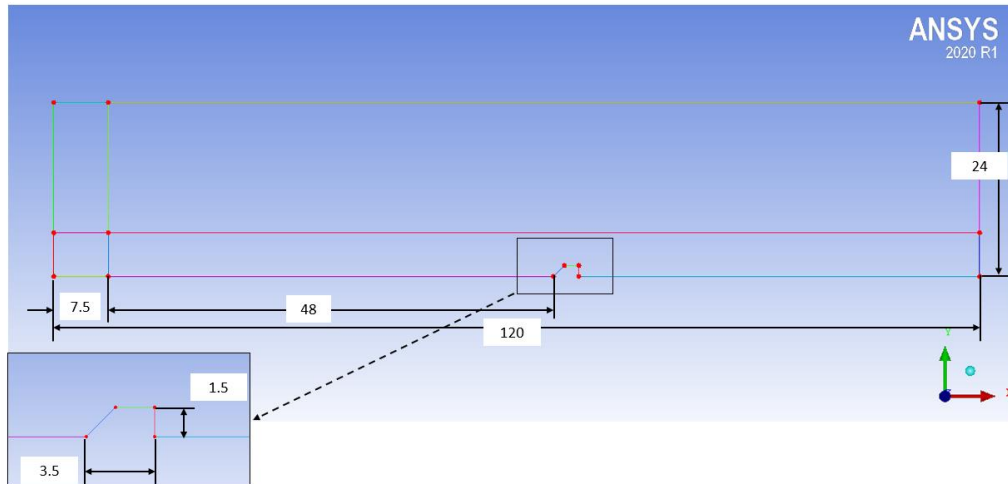


Figure 3-7: ICEM Geometry for 2-D TB Model. Dimensions are in Inches.

The outlet of the domain at the far right of Figure 3-7 was positioned approximately 16 body lengths downstream of the excrescence to allow a separated wake structure to develop before any outlet boundary condition is imposed. Additionally, the 7.5-inch curve furthest to the left of the domain was created with the intent of imposing a *symmetry*, or “slip wall”, boundary condition to ensure proper boundary layer growth upstream of the excrescence. The distance upstream of the 2-D excrescence was chosen to be 48 inches to best replicate the boundary layer thickness captured in the wind tunnel experiment based on turbulent boundary layer growth along a flat plate²².

Blocking is a useful tool for creating 2-D and 3-D structured grids for complex geometries. The blocking process begins by creating a *block* around the entire geometry that consists of *edges* and *vertices*. Next, the single block can be split into several sub-blocks depending on the requirements of the geometry. Some sub-blocks can be deleted to represent impermeable boundaries in the domain. For the present model, a 2-D planar block was applied around the entire domain and split twice horizontally, and three times vertically to produce twelve separate blocks. The bottom block representing the 2-D excrescence was deleted to represent the solid body, and the remaining eleven blocks were left to represent the fluid above and around the body as shown in Figure 3-8.

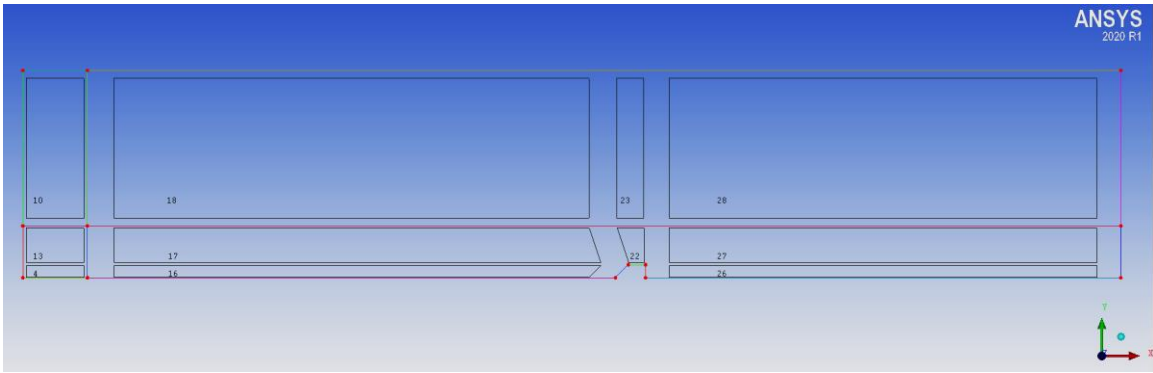


Figure 3-8: Blocking Geometry for 2-D TB Model.

Once the blocks were created, each block's edges and vertices were carefully associated to the actual curves and points that represent the excrescence geometry and wind tunnel extents. Splitting the domain into discrete sections allows for the gridding scheme to be unique to each area of the domain. In particular, the blocks nearest the excrescence will have a very different grid pattern than that of the free stream fluid.

Up to this point, every command executed in the geometry creation and blocking processes was recorded in a *replay script*. The replay script was later edited using the general-purpose multi-paradigm system programming language, *Tcl/Tk*, to automatically reproduce the same domain geometry for the short excrescence. The *Tcl/Tk* script used to do this can be seen in Appendix G. Finally, the distribution of grid points along each block edge was specified, and a structured mesh was generated for each block and mapped to the actual geometry. Grid point distributions were copied to all parallel edges in the domain producing the structured grid shown in Figure 3-9.

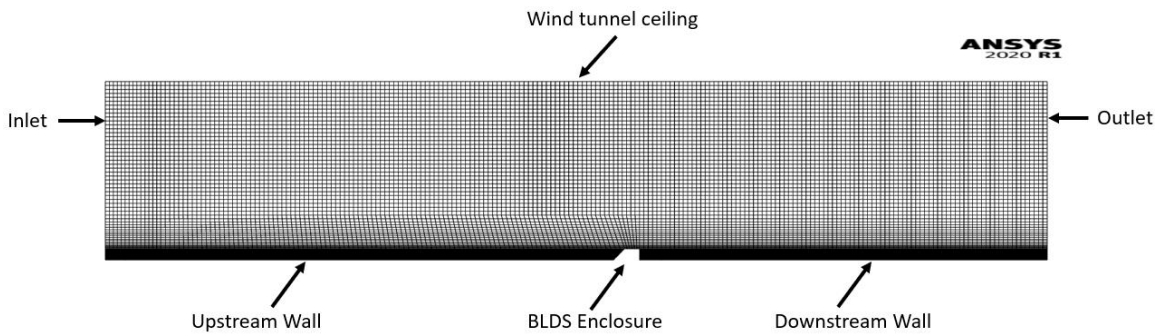


Figure 3-9: Mesh Pattern for 2-D TB Model.

As previously stated, the grid pattern nearest the wall and excrescence boundaries is far denser with cells than the rest of the grid. For this thesis, the upstream wall, excrescence, and downstream wall will be considered “no-slip” walls. This means that the velocity of the air right against these edges will be zero, and the velocity very near them will change rapidly until the free-stream velocity is reached. Accurate calculations in the near-wall region are paramount to the success of each simulation because the goal of this work is to report pressures and forces as they appear on the upstream wall and excrescence surfaces. To accomplish near-wall accuracy, a “viscous sublayer resolution” approach was taken in the design of the 2-D models¹⁹. In brief, resolving the viscous sublayer involves adding a significant number of grid points near the walls, and reducing the number of grid points with distance away from the wall. Figure 3-10 gives a cartoon depiction of what a near-wall structured mesh could look like with (right) and without (left) viscous sublayer resolution.

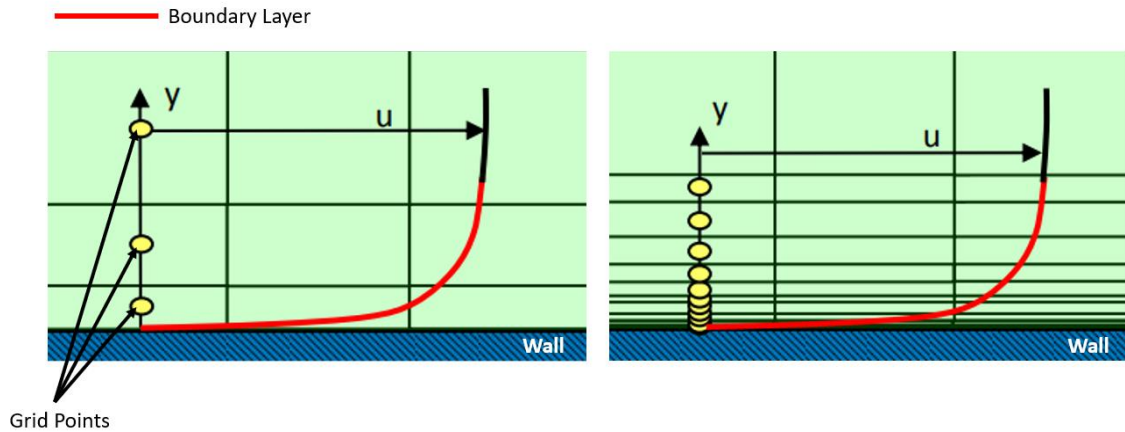


Figure 3-10: Viscous Sublayer Resolution Technique. Adapted From Ansys Theory Guide¹⁹.

To ensure careful resolution of the viscous sublayer, Ansys FLUENT recommends locating the first grid cell well within the log-layer to produce a y^+ value of approximately 1. Additionally, the growth rate of cells adjacent to the first grid cell, or *growth ratio*, should be no larger than 1.2¹⁹. For $y^+ \approx 1$, the distance that the first cell must be located away from the wall, or *spacing*, was calculated to be approximately 0.0004 inches. The initial spacing was applied to the ICEM model using a *bunching law* on the inlet and outlet edges. Particularly, the *Geometric 1* built-in bunching law was used to concentrate nodes at the bottom of the domain, and the growth ratio was specified to be 1.1.

The BC's were specified in ICEM using the built-in edge BC types. The boundary conditions were applied to the structured grid as shown in Figure 3-11.

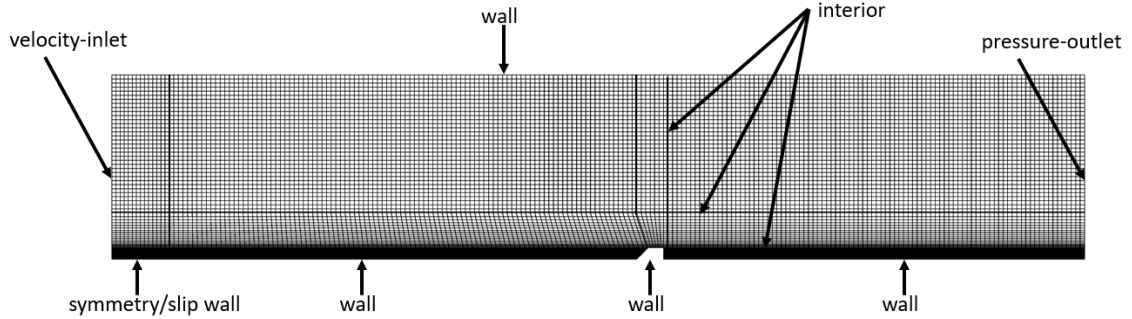


Figure 3-11: Structured Mesh for 2-D TB Model Including BC's.

The inlet to the domain was given a *velocity-inlet* condition which allows the user to specify a uniform velocity normal to the inlet boundary. Likewise, the *pressure-outlet* allows for the pressure at the exit of the domain to be specified at the outlet boundary. The no-slip *wall* condition was applied to the upstream wall, downstream wall, wind tunnel ceiling, and all BLDS excrescence surfaces. The curves partitioning the grid in Figure 3-11 represent the edges of the fluid blocks that were given *interior* conditions. Interior BC's are sometimes called *flow through*. These conditions will encourage FLUENT to treat the interior boundaries as if they are not there provided that the grid pattern transitions smoothly across them¹⁹. Finally, the first 7.5 inches of the domain were given a symmetrical boundary condition. For the present work, a symmetry boundary condition is imposed ahead of the upstream wall to act as a *slip wall* ensuring that the boundary layer begins growing exactly 48 inches upstream of the excrescence.

CFD solutions are highly dependent on the structure of the computational grid. For this reason, it is imperative to perform a *mesh independence* study on any computational grid prior to collecting results for comparison to experimental data. Three meshes with the TB geometry and BC's discussed above were generated with

increasing numbers of grid points. Each grid was output to Ansys FLUENT and run with the case parameters discussed in the following section. A solution is considered fully “mesh independent” when it appears to no longer depend on cell density which is typically measured by how much results of interest change between successive meshes¹⁹. The results of interest for the present work are surface static pressures and a free stream reference static pressure because these values will be used to calculate the upstream surface C_p . Three meshes with increasing numbers of grid points were produced for the TB domain, and they are described in Table 3-2 below. A reference static pressure located at $(x, y) = (8 \text{ in}, 12 \text{ in})$ and a surface static pressure located at $(x, y) = (8 \text{ in}, 0 \text{ in})$ were collected from each successive grid and plotted against the number of grid points. The results of the grid independence study are shown in Figure 3-12.

Table 3-2: 2-D Mesh Independence Study Case Identifiers

Mesh	Grid Points	Reference Dynamic Pressure [Pa] <i>q_{ref}</i>
TB-M-1	3880	1031.8
TB-M-2	5840	1031.1
TB-M-3	15978	1030.1

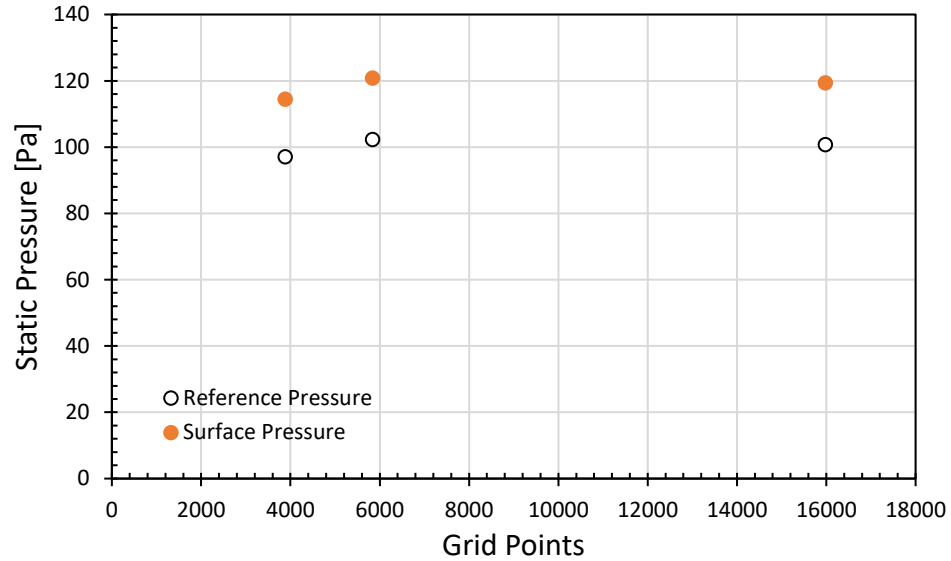


Figure 3-12: 2-D TB Mesh Independence Study.

Mesh independence was achieved with mesh TBM-2 that contains about 6000 grid points. The surface and reference static pressures changed by 1.51% and 1.25% between TB-M-2 and TB-M-3, respectively. The fine-grid convergence index for C_p was computed with TB-M-1, TB-M-2, and TB-M-3 using the Richardson extrapolation method outlined in the JFE Statement on the Control of Numerical Accuracy²⁵. The computed GCI_{fine} for the 2-D mesh was found to be 0.9 % with an average order of accuracy of 1.7. This corresponds to an uncertainty in upstream C_p of ± 0.005 which varies slightly with upstream position as determined by computing GCI_{fine} at three different upstream locations. The details of the calculation at each upstream position are presented in Appendix H for reference. The number of grid points specified along each edge of the converged domain was documented and carried through all 2-D CFD cases that will be discussed in section 3.2.2.

To modify the wall-bounded domain to a “free-air” domain, a height independence study was conducted for the 2-D domain in a similar fashion to the mesh independence study. First, the BC at the top of the domain was changed from no-slip wall to a different BC that allows the velocity at the boundary to be about the same as the free stream velocity. In most pre-processing programs, there are three BC’s that will achieve this: fixed velocity, pressure outlet, or symmetry. Typically, the symmetry BC is best to ensure the boundary layer is unconstrained, so a symmetry BC was chosen for the top boundary in this thesis. However, if the extent of the domain is sufficient, the BC type should have no effect on the solution. Using the replay script in Appendix G, four meshes with increasing domain height were produced for the TB domain. Height independence mesh identifiers and results are shown in Table 3-3 and Figure 3-13. The results of the height independence study show that $h_D \geq 108$ inches is sufficient to conduct a free-air calculation.

Table 3-3: 2-D Height Independence Study Case Identifiers

Mesh	Domain Height [in] h_D	Reference Dynamic Pressure [Pa] q_{ref}
TB-H-1	24	1030.1
TB-H-2	60	1029.3
TB-H-3	84	1028.6
TB-H-4	108	1028.1

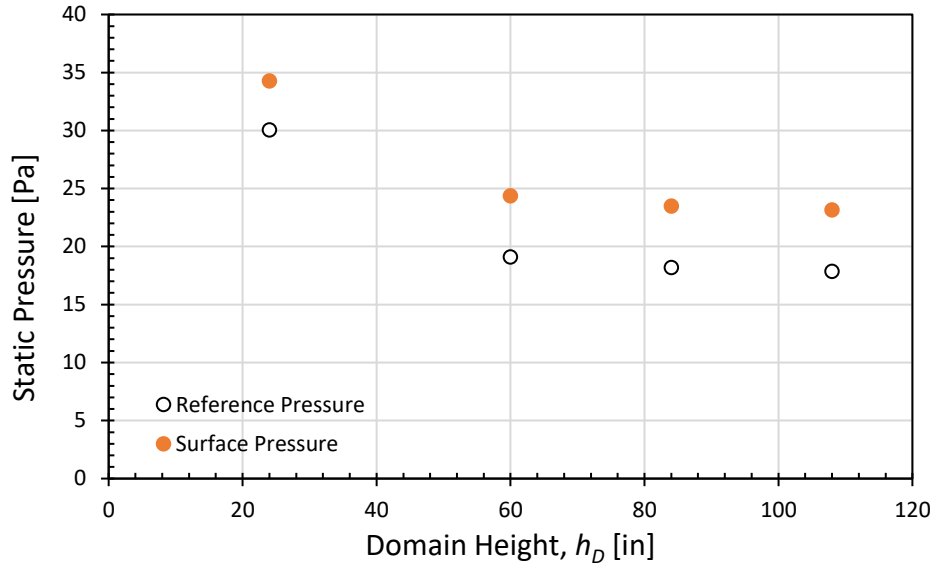


Figure 3-13: 2-D TB Height Independence Study.

It is important to note that the free-air domain height is expected to scale with the height of the BLDS excrescence modeled. However, the height independence study above was conducted with the taller 2-D excrescence. Therefore, reducing the BLDS excrescence height to model the smaller profile will not require adjustment of the free-air domain height.

3.2.2 2-D Case Set-Up in FLUENT

A successful CFD simulation includes three general activities: preprocessing, processing, and postprocessing. This section details the steps taken to produce a high-fidelity flow simulation using Ansys FLUENT and the 2-D structured grid discussed above. Six different cases described by Table 3-4 were run using the same FLUENT case set-up. The Mach number and Reynolds number per unit length for all 2-D CFD cases were maintained as 0.12 and $8.56 \times 10^5 \text{ ft}^{-1}$, respectively.

Table 3-4: 2-D CFD Cases

Case	Mesh	Excrescence	Characteristic Height [in]
1	TB	Tall Model	1.50
2	SB	Short Model	0.71
3	TA	Tall Model	1.50
4	SA	Short Model	0.71
5	TB	Removed	-
6	SB	Removed	-

For Cases 3 and 4, the distance between the floor and ceiling of the domain was adjusted to 108 inches allowing the solution no longer depended on domain height thereby representing the free-air flow. In addition, Cases 5 and 6 were run with meshes whose BC's for the 2-D excrescence were changed from *wall* to *flow-through* in order to capture the boundary layer profile as it appears at the nose of each 2-D excrescence. The following case set-up discussion applies to all meshes listed in Table 3-4.

Preprocessing

Once each mesh file was read into FLUENT, a built-in mesh check routine was run to ensure that the imported mesh did not contain any irregularities. FLUENT allows for a choice between two numerical methods: a *pressure-based solver* or a *density-based solver*. From a historical perspective, the pressure-based solution approach was designed for low-speed incompressible flows, and the density-based solver for high-speed compressible flows¹⁹. All simulations for the present work will be run with an inlet velocity of 41 m/s to best replicate the wind tunnel velocity at a blower drive frequency

of 50 Hz. At sea level, the resulting Mach number for this inlet velocity is 0.12 which is well within the subsonic regime where the flow can be considered incompressible⁹. Since compressibility is not being considered in this work, the pressure-based solver was selected for use in all simulations. The remaining solver settings were left as the FLUENT software default shown below.

Table 3-5: 2-D Simulation Solver Settings.

Setting	User Specification
Solver Type	Pressure-Based
Velocity Formulation	Absolute
2-D Space	Planar
Time	Steady

Next, the turbulence model was set to the S-A one-equation model and all model constants were left as the standard default values¹⁷. The fluid in all cases was set to be standard air at a constant temperature of 15°C (288.15 K), constant density of $\rho = 1.225 \text{ kg/m}^3$, and constant molecular viscosity of $\mu = 1.7894 \times 10^{-5} \text{ kg/m-s}$. A solid material was not specified for the 2-D simulations because the mesh was designed by removing the block that represents the solid BLDS excrescence. Additionally, the simulations do not involve conduction heat transfer, so it is not imperative to specify the material at solid boundaries.

The BC's described in the model design section were given specific parameters in FLUENT. The symmetry and interior BC's do not require further specification, but the modifications made to the wall, velocity-inlet, and pressure-outlet BC's are given in Table 3-6.

Table 3-6: Boundary Conditions (BC's) for 2-D FLUENT Cases.

BC	Momentum		Thermal
	Setting	User Specification	User Specification
wall	Wall Motion	Stationary	No Heat Flux
	Shear Condition	No-slip	
	Roughness Model	Standard	
velocity-inlet	Specification Method	Normal to Boundary	Constant $T = 288.16$ K
	Velocity Magnitude (m/s)	41	
pressure-outlet	Specification Method	Normal to Boundary	Constant $T = 288.16$ K
	Gauge Pressure (Pa)	0	

For all no-slip walls in the 2-D CFD cases, the wall roughness was set to *standard*. The standard roughness model uses a default roughness height of 0 meters which corresponds to smooth walls. To compute C_p , FLUENT requires a user input *reference value* for the reference static pressure, p_{ref} . The reference static pressures for each case were collected from the free stream of each domain once they were determined to be fully mesh independent. A table of p_{ref} values for all 2-D and 3-D cases can be seen in Appendix K.

The final step in preprocessing is selecting the solution methods and controls. The solution methods selected for all 2-D FLUENT cases are shown in Table 3-7 below.

Table 3-7: Solution Methods for 2-D CFD Cases

Solution Method	Setting	User Specification
Pressure-Velocity Coupling	Scheme	SIMPLE
Spatial Discretization	Gradient	Least Squares Cell Based
	Pressure	Standard
	Momentum	QUICK
	Modified Turbulence Viscosity	QUICK

In the pressure-based solver, FLUENT offers four types of pressure-velocity coupling methods. For steady state flows involving turbulence, the SIMPLE and SIMPLEC algorithms¹⁹ are recommended with no significant difference in convergence rates. For the present work, the SIMPLE algorithm was selected and used for all 2-D CFD cases. The least squares cell based gradient method, and QUICK upwinding scheme¹⁹ were chosen because they are considered least computationally expensive for 2-D flows. A standard pressure discretization was chosen because no strong body forces are included in these analyses, and there is no natural convection occurring. The mesh is also packed tightly in regions of high gradient to resolve the pressure variation adequately without any advanced pressure discretization. The solution controls for all 2-D CFD analyses were left as the default values provided by the SIMPLE algorithm and are shown in Table 3-8.

Table 3-8: Solution Under-Relaxation Factors for Pressure-Based SIMPLE Algorithm

Solution Control	Under-Relaxation Factor
Pressure	0.3
Density	1.0
Body Forces	1.0
Momentum	0.7
Modified Turbulence viscosity	0.8
Turbulence viscosity	1.0
Energy	1.0

Processing

Before running each case, residual monitors for continuity, x-velocity, y-velocity, and turbulence viscosity, were set to 1×10^{-6} and each calculation was run with 3000 iterations. Convergence for all bounded 2-D models was reached in approximately 1400 iterations, and an example of the scaled residuals from processing Case 2 are shown in Figure 3-14. Scaled residuals for the momentum equations, continuity equation, and turbulence viscosity transport underwent approximately five orders of magnitude of reduction over the course of the calculation. All 2-D models had a similar smooth convergence process like that shown in Figure 3-14.

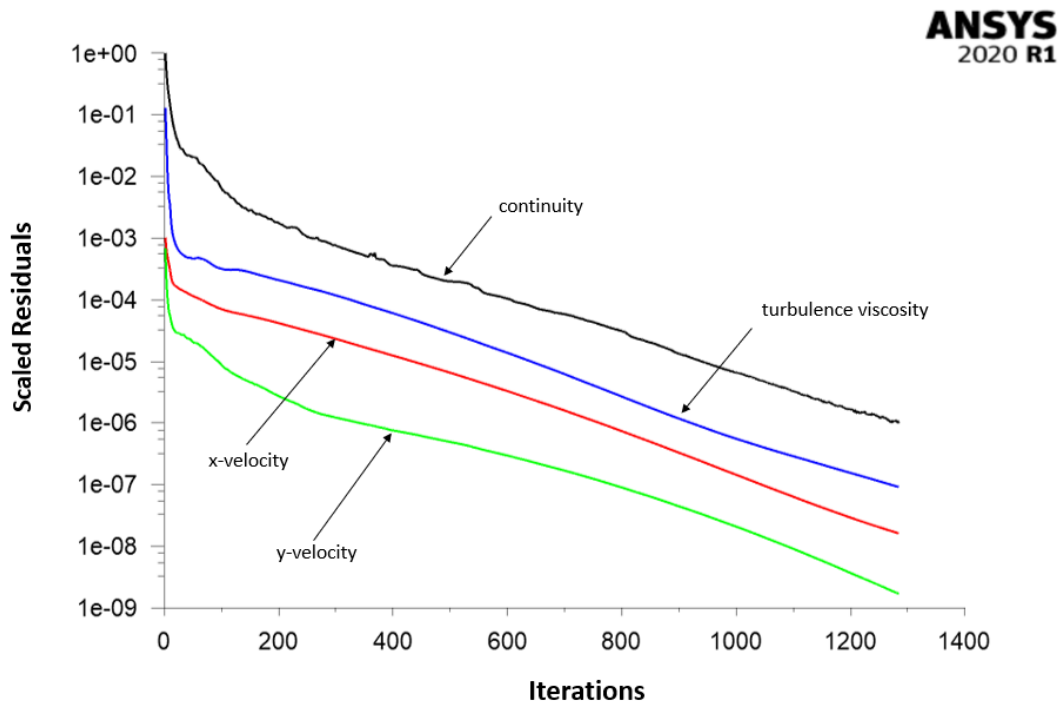


Figure 3-14: Scaled Residual Monitor From Processing 2-D CFD Case 2 (SB Model).

Postprocessing

After each FLUENT simulation reached convergence, several checks were done to see how closely the CFD results align with engineering judgements. First, the net imbalance of mass flow rate between the inlet and outlet boundaries was checked to ensure that it was less than 1% of mass flow through the inlet¹⁹. All 2-D models had approximately 1.4×10^{-6} % of net mass flow rate imbalance at the conclusion of each calculation meaning mass conservation was achieved. Additionally, Reynolds numbers based on excrescence height, Re_h , boundary layer thickness, Re_δ and leading edge location, $Re_{x_{le}}$ were computed and shown to agree well with the same from the 2-D experiments.

Table 3-9: Reynolds Numbers From 2-D CFD Cases and Wind Tunnel Experiments

	Re_h Short Model	Re_h Tall Model	Re_δ Short Model	Re_δ Tall Model	$Re_{x_{le}}$
Experiment	4.69×10^4	9.88×10^4	5.85×10^4	5.85×10^4	2.02×10^6
2-D FLUENT	5.08×10^4	1.07×10^5	6.56×10^4	5.92×10^4	3.42×10^6

Other flow structures and phenomena were checked to ensure the model was behaving as would a real viscous flow. For instance, it is expected that the boundary layer will separate from the surface very close to the leading edge of each excrescence. To measure this, C_f was plotted against distance upstream of the 2-D excrescences and the results for Cases 1 and 2 are shown in Figure 3-15.

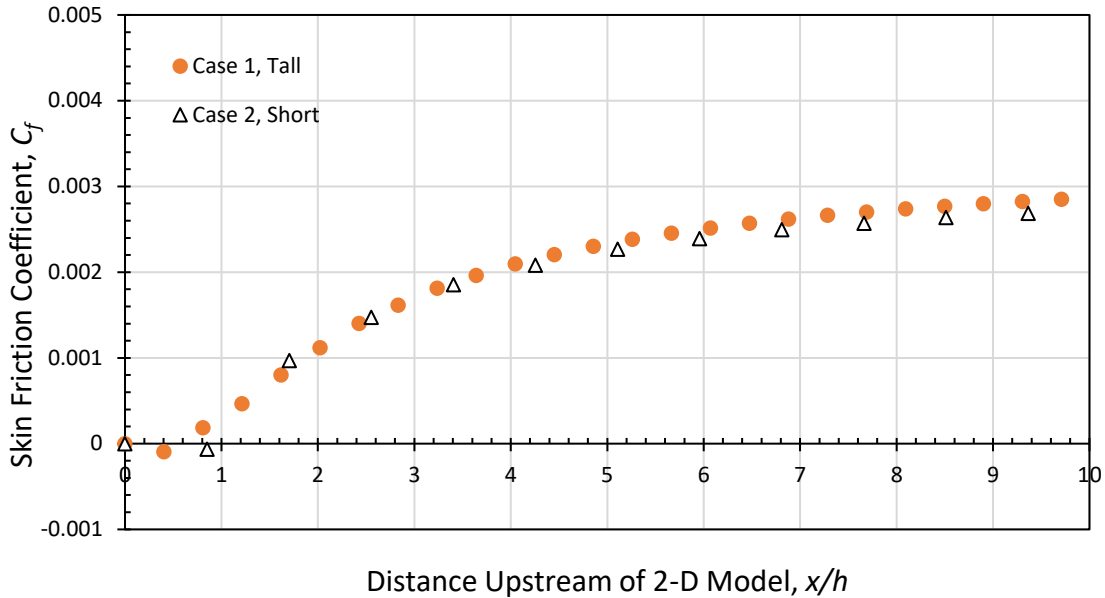


Figure 3-15: Upstream C_f for 2-D CFD Cases 1 and 2.

Case 1 saw a C_f of zero at approximately 0.6 body heights upstream of its leading edge suggesting that separation does occur very slightly upstream of the excrescence. For Case 2, $C_f = 0$ around 0.9 body heights upstream. In addition, the C_f has a very small negative magnitude about 0.4 body heights upstream of the tall excrescence, and 0.8 body heights upstream of the short excrescence. This indicates that the wall shear stress has reversed direction and there exists a small region of reversed flow as expected. Similarly, since the excrescences have blunted trailing edges, it is expected that a low-pressure wake structure will occur off the back of each excrescence⁵. The velocity vector fields shown in Figure 3-16 show flow structures that indicate the presence of a wake behind each excrescence. Upon closer inspection, the dark regions behind each excrescence show velocity vectors pointing against the direction of flow, displaying the presence of a reversed flow.

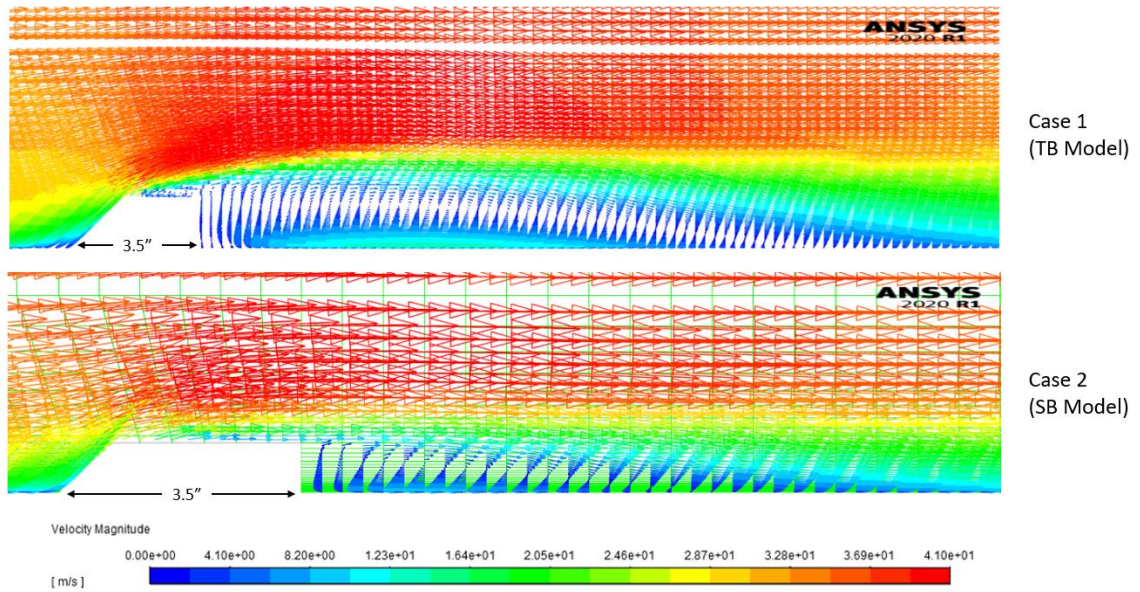


Figure 3-16: Velocity Vector Plots for Cases 1 and 2.

To validate the FLUENT case set-up, the upstream pressure coefficients extracted from the CFD results were directly compared to the experimental data collected from the wind tunnel. The comparison for the tall and short excrescences can be seen in Figures 3-17 and 3-18, respectively.

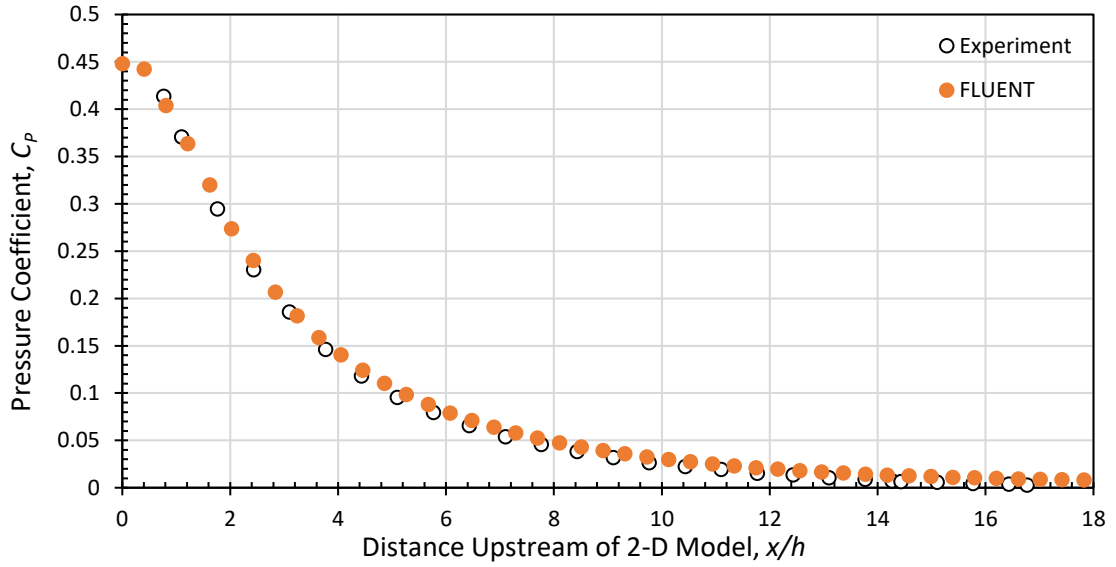


Figure 3-17: Computed Upstream C_p From 2-D Case 1 (Tall) Compared to Experiment

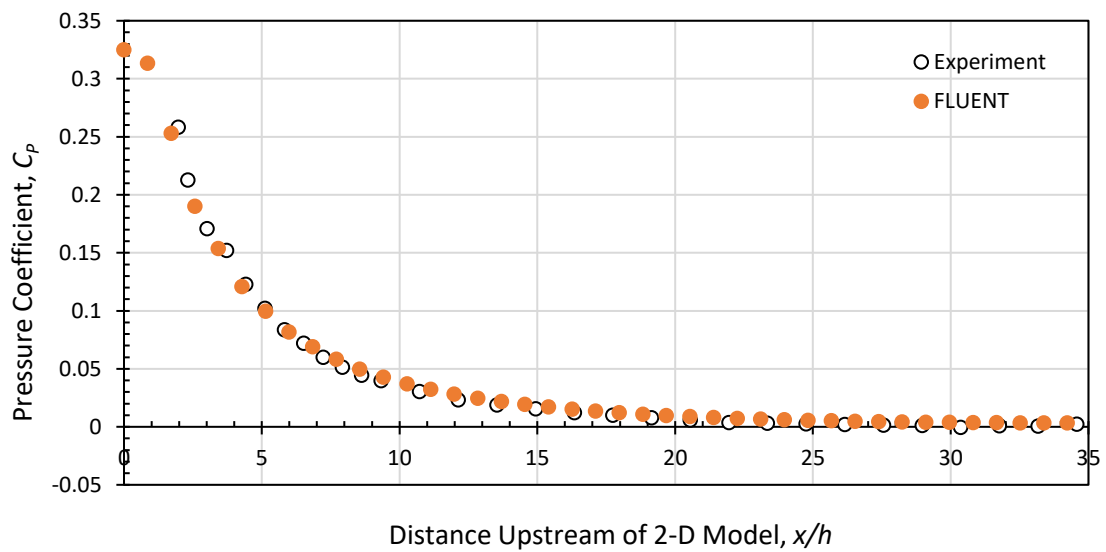


Figure 3-18: Computed Upstream C_p From 2-D Case 2 (Short) Compared to Experiment

Clearly, the FLUENT results were able to achieve excellent agreement with the experimental data confirming that the boundary layer has been well resolved in the

region upstream of the excrescence. The results from Chapter 2 displayed in Figure 2-11 were replicated using the computed results from FLUENT for further comparison.

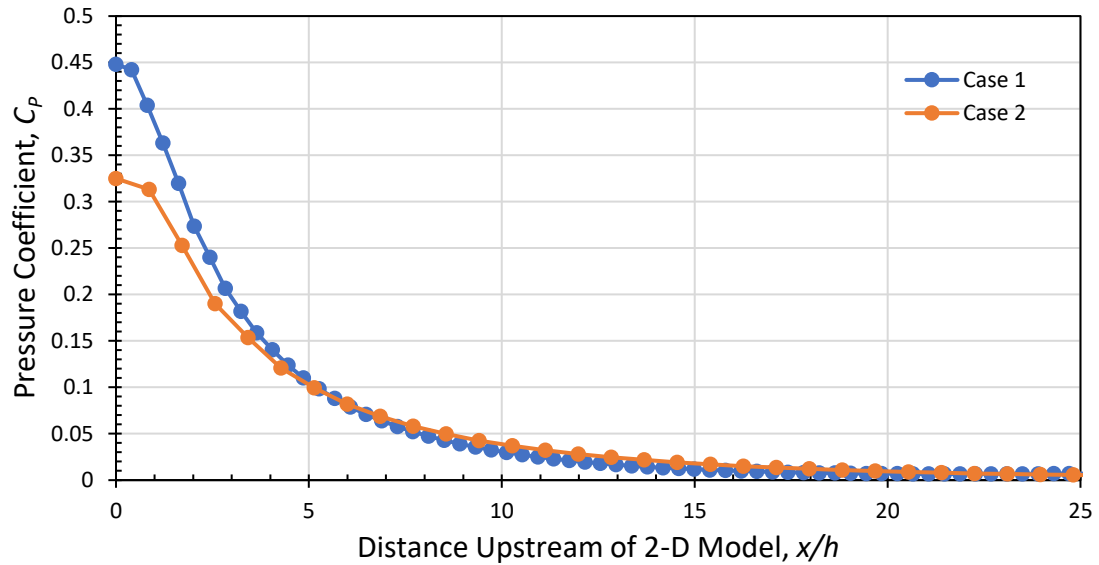


Figure 3-19: 2-D CFD Upstream C_p for Cases 1 (Tall) and 2 (Short).

The location upstream at which the experimental data suggests C_p reaches a negligibly small value appears to be well replicated by the CFD. The experiment showed that both excrescence heights reached a C_p value of 0.05 around 7 body heights upstream of each model nose. The FLUENT results very closely match this with $C_p \approx 0.05$ occurring around 6.8 and 6.5 body heights upstream for Cases 1 and 2, respectively. Figure 3-20 also shows that there is no significant difference in C_p between Cases 1 and 2 upstream of $x/h \approx 4$. Most of the influence on the pressure field due to the change in excrescence height occurs within 4 body heights of the excrescence leading edge.

The shorter 2-D model's presence in the wind tunnel produced 2.97% solid blockage based on the test section cross-sectional area, and the taller model produced 6.25%. Both values are below the maximum ratio of model frontal area to test section cross-sectional area suggested by Rae and Pope²⁷, however, if there is any effect of solid blockage it will be present in the wind tunnel measurements. For that reason, it is important to identify if solid blockage effects are present in the computed results. The free-air CFD models are considered blockage free as the ratio of domain height to excrescence height are 0.66% and 1.4% for the short and tall models respectively. Therefore, to identify solid blockage effects, the computed pressure disturbance from the free-air FLUENT models (TA and SA) were compared to the same from their wall-bounded counterparts (TB and SB).

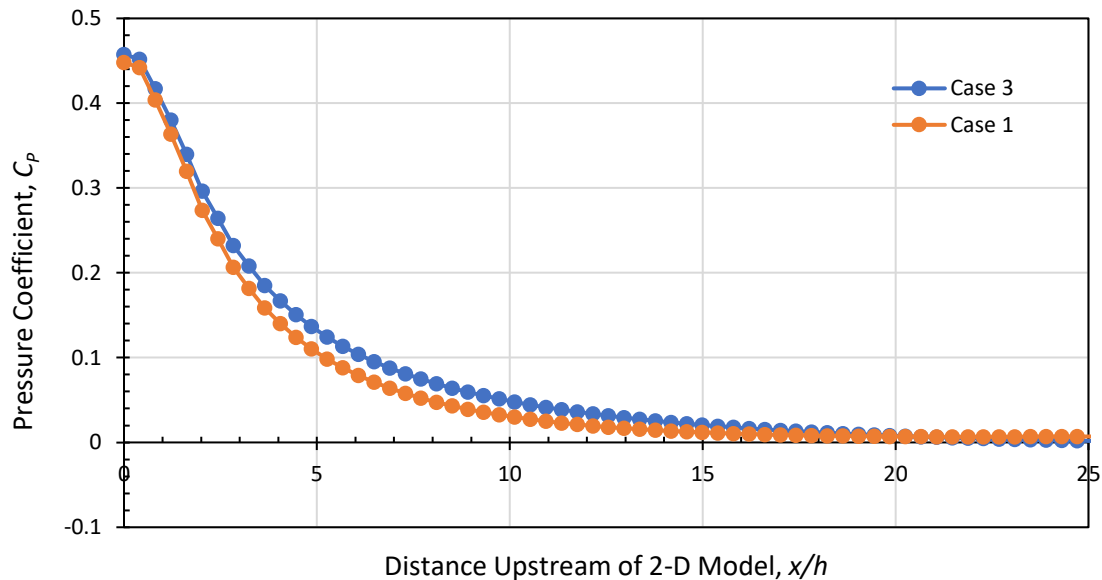


Figure 3-20: Wall-Bounded (Case 1) and Free-Air (Case 3) Upstream C_p for the Tall Excrescence.

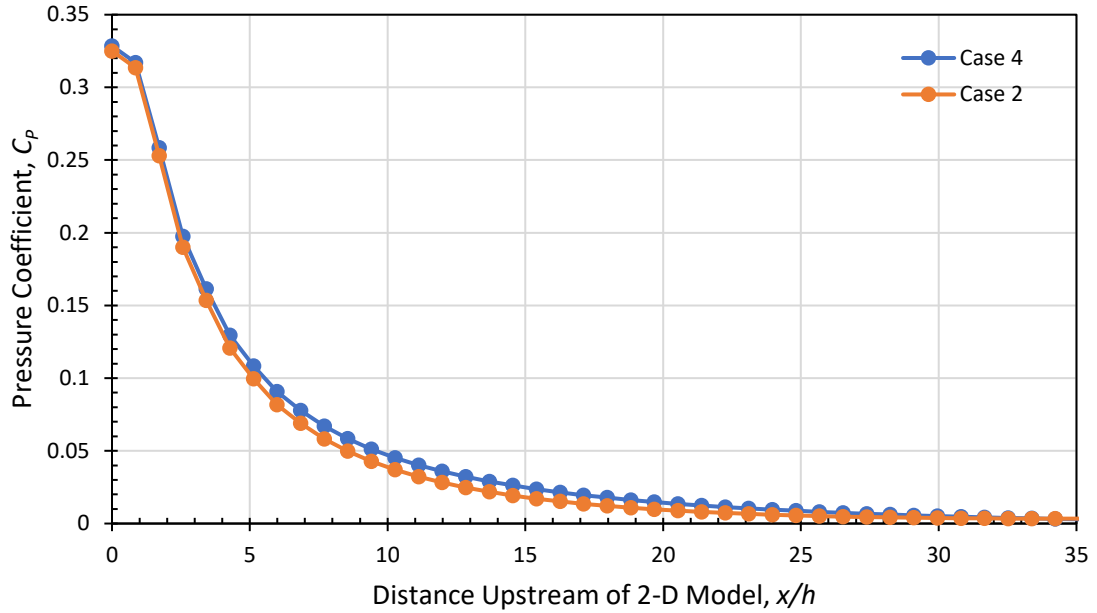


Figure 3-21: Wall-Bounded (Case 2) and Free-Air (Case 4) Upstream C_p for the Short Excrescence.

The C_p values for Cases 1 and 2 appear to be pushed down against the horizontal axis when compared with the free-air results from Cases 3 and 4. This is due to the solid blockage of the 2-D excrescences. The increased velocity of the air as it flows over the excrescence causes the local dynamic pressure to increase, and the pressure coefficients to decrease. It is expected that the taller model will have more solid blockage than the shorter model, and this is shown by comparing the results of Figures 3-20 and 3-21. At about 10 body heights upstream, the shorter excrescence shows $\Delta C_p \approx 0.008$ between the wall-bounded and free-air domain whereas the taller model sees upwards of $\Delta C_p \approx 0.02$ at this location. These differences are small, but larger than the discretization error in C_p (± 0.005) therefore significant enough to consider in wall-bounded modeling.

From the inviscid analysis, it is also expected that the upstream pressure disturbance curves from the viscous CFD models will resemble the inviscid upstream pressure disturbance. The C_p curves computed from FLUENT Cases 3 and 4 were compared to the inviscid analysis discussed previously.

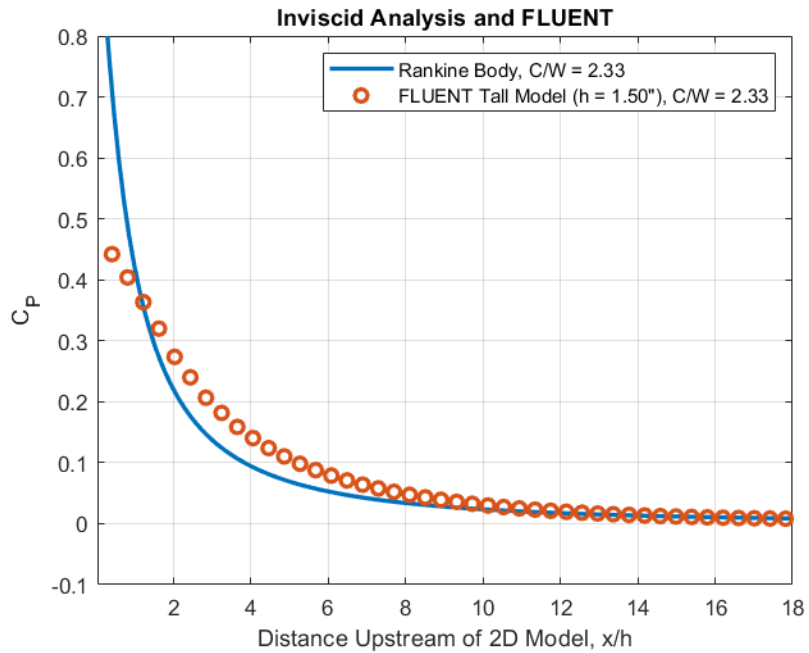


Figure 3-22: 2-D CFD Case 3 Upstream C_p Compared to Inviscid Analysis.

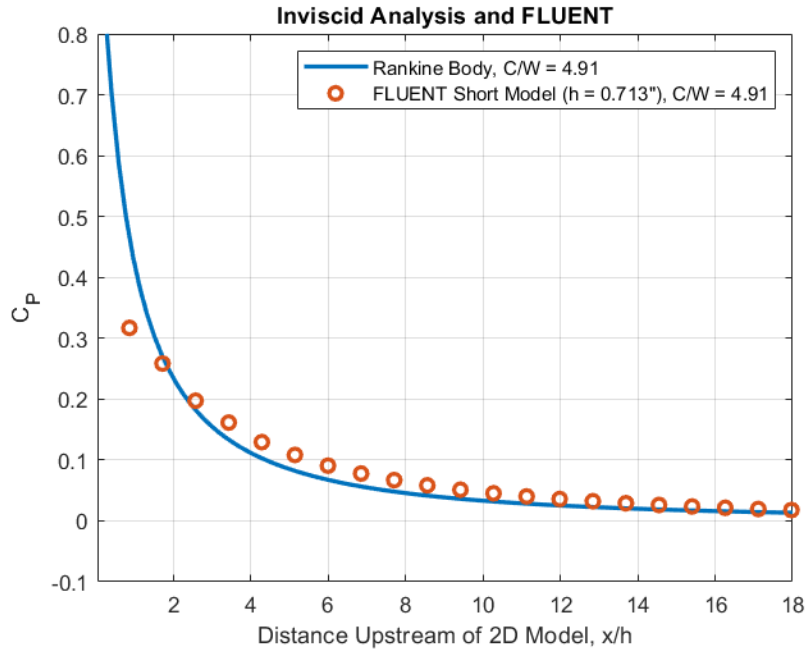


Figure 3-23: 2-D CFD Case 4 Upstream C_p Compared to Inviscid Analysis.

As expected, the computed results align well with the inviscid solution, especially far upstream of each model nose, and the C_p values appear to be slightly larger than the predictions from the inviscid solution. At about 5 body heights upstream, the tall model sees a $\Delta C_p \approx 0.05$ between the inviscid analysis and viscous CFD solution. At the same location, the short model sees $\Delta C_p \approx 0.03$. The taller excrescence experiences a larger displacement upstream than the short model which also aligns well with the inviscid comparison to the experimental data in section 3.1.

Cases 5 and 6 were used to compare the velocity profile and boundary layer thickness simulated in FLUENT to that of the experimentally measured boundary layer. The velocity profile comparison is shown in Figure 3-24.

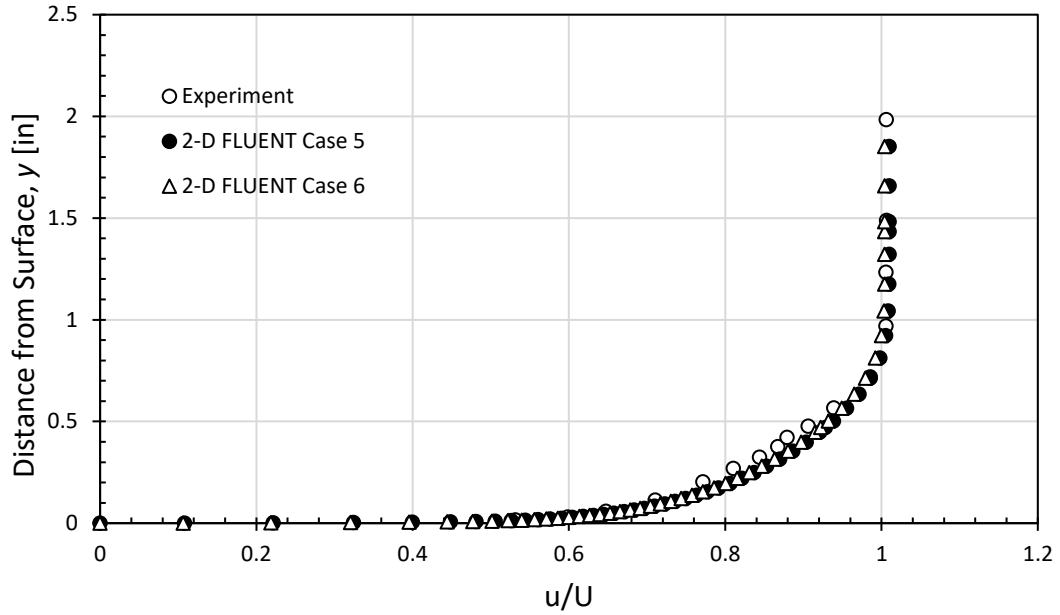


Figure 3-24: Boundary Layer Velocity Profiles for Cases 5 and 6 Compared to Experiment.

The boundary layer thicknesses collected from FLUENT at the leading edge location of the 2-D excrescences were found to be approximately 0.83 inches for Case 5 (TB), and 0.92 inches for Case 6 (SB) which are 6.9 % and 3.7 % different from the boundary layer thickness measured in the wind tunnel experiment, respectively. From Figure 3-24, the undisturbed boundary layer shape appears to be very well-replicated by the CFD as well. The wall-bounded and free-air FLUENT cases resulted in the following height to boundary layer thickness ratios, h/δ , presented in Table 3-10.

Table 3-10: Height to Boundary Layer Thickness Ratios, h/δ , for 2-D CFD Cases

Excrescence Height [in]	Experiment h/δ	Wall-Bounded (Cases 1, 2) h/δ	Free-Air (Cases 3, 4) h/δ
1.5	1.689	1.812	1.626
0.713	0.803	0.861	0.773

Finally, the dimensionless pressure drag force imposed on each 2-D excrescence was calculated using the surface integral function in FLUENT. Specifically, the static pressure was integrated along the curves that compose the front and back solid boundaries of each 2-D excrescence as depicted by curves 1 and 2 in Figure 3-25.

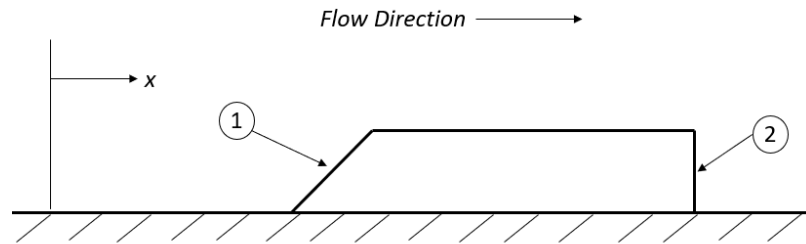


Figure 3-25: Curves Over Which Static Pressure is Integrated for 2-D Computation of C_{DP} .

To compute the dimensionless pressure drag coefficient, the sum of the integrated pressure on the front and back was divided by the characteristic height (see Table 3-1) and the reference dynamic pressure for each excrescence. The computed C_{DP} values for the free-air flow cases are shown in Table 3-11.

Table 3-11: Pressure Drag Coefficients for 2-D Cases 3 and 4

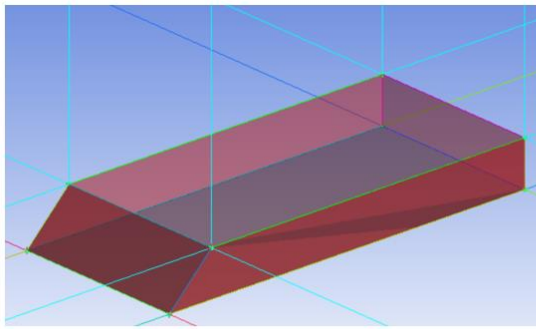
Case	Excrescence	Pressure Drag Coefficient
		C_{DP}
3	Tall Model	0.70
4	Short Model	0.48

The C_{DP} values computed in FLUENT appear to increase with an increase in excrescence height. However, the computed boundary layer thicknesses from the TB and SB meshes were not the same, nor were the local Reynolds numbers. Therefore, a more accurate observation is that the pressure drag coefficient increased with the increase in h/δ between Cases 3 and 4 which agrees well with the expectation described in Hoerner's *Fluid Dynamic Drag*⁵.

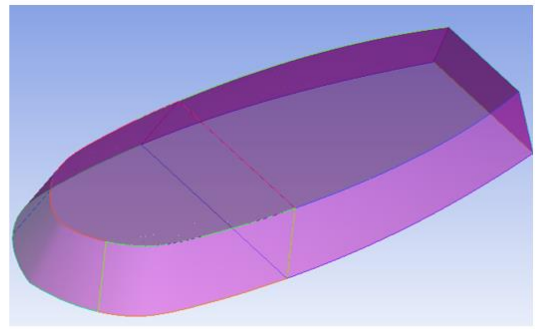
The expected flow features have been shown to exist in the 2-D CFD results and the computed upstream pressure disturbance agrees well with the experimental data. The undisturbed boundary layer thicknesses computed in each 2-D model are within 10% of the measured thickness, and the shape of the computed boundary layer agrees well with that of the measured turbulent boundary layer. The FLUENT case set-up and model design methods discussed in the chapter will be mostly replicated for all 3-D CFD models.

4. 3-D CFD CASES

Once the details of the model design and FLUENT case set-up were proven to produce reasonable results in 2-D, the 3-D domains were created. This chapter will detail the 3-D FLUENT case set-up and design of two 3-D domains that model the BLDS ramped-front enclosure and half-scale fairing as described in Chapter 2 and depicted in Figure 4-1.



BLDS Ramped-Front Enclosure Geometry



BLDS Half-Scale Fairing Geometry

Figure 4-1: BLDS Ramped-Front Enclosure and Half-Scale Fairing Housings as Modeled in ICEM.

Once the 3-D models were validated with experimental data, geometric characteristics of the BLDS ramped-front enclosure were changed and the impact on the upstream pressure disturbance and pressure drag were evaluated.

4.1 3-D Model Designs in ICEM CFD

All 3-D models discussed in this chapter were created to have free-air boundary conditions. Table 4-1 lays out a naming scheme that will be used to distinguish each domain and mesh type throughout this chapter.

Table 4-1: 3-D Domain/Mesh Identifiers

Domain/Mesh Identifier	Description
RFE	3-D domain used to simulate the BLDS ramped-front enclosure positioned on a flat wall
HSF	3-D domain used to simulate the BLDS half-scale fairing positioned on a flat wall
M	Mesh used for a grid independence study
A	Mesh with fully optimized free-air dimensions
H	Mesh used to optimize the domain height
W	Mesh used to optimize the domain width

As an example, a mesh titled “RFE-A” is a 3-D mesh created in the BLDS ramped-front enclosure domain whose dimensions have been optimized to represent free-air flow.

In CFD, it is often advantageous to only model half of a symmetrical flow, dividing it along its plane of symmetry by a “slip wall” boundary condition. While it is recognized that the BLDS housings in this work are symmetrical, this approach was not taken as simulation run times were found to be manageable without reducing the grid size by a factor of two.

4.1.1 3-D Ramped-Front Enclosure

The first model was created for the BLDS ramped-front enclosure (RFE). Height and width independence studies were required to simulate free-air flow, so the enclosure was first modeled in the 2 x 2-foot wind tunnel for simplicity and a replay script was later used to optimize the free-air domain. The points and curves created for the 3-D enclosure domain are shown in Figure 4-2. The h_D and w_D dimensions were optimized for the free-air model. The width of the enclosure itself is defined as w_e .

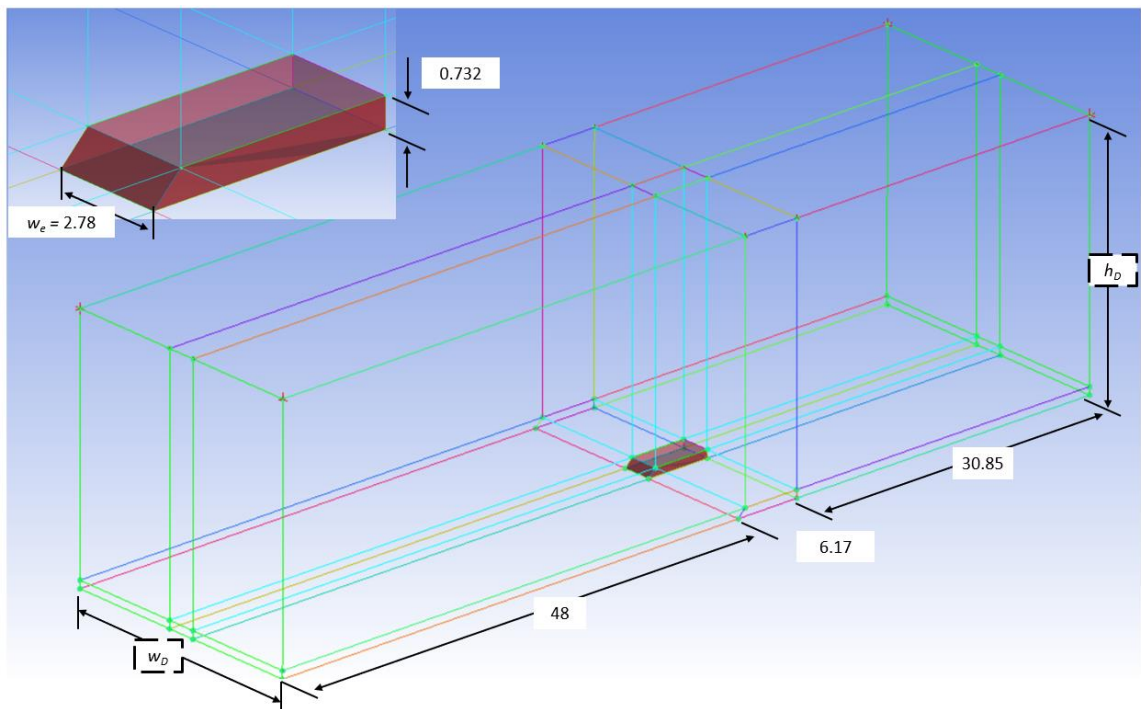


Figure 4-2: ICEM Geometry for 3-D RFE Model. Dimensions are in Inches.

The upstream wall is 48 inches to best replicate the experimental boundary layer thickness as described in Chapter 2. Surfaces for the inlet, outlet, walls, and interior were created and used to assign boundary conditions. The surfaces for the RFE domain and corresponding BC's are shown in Figure 4-3.

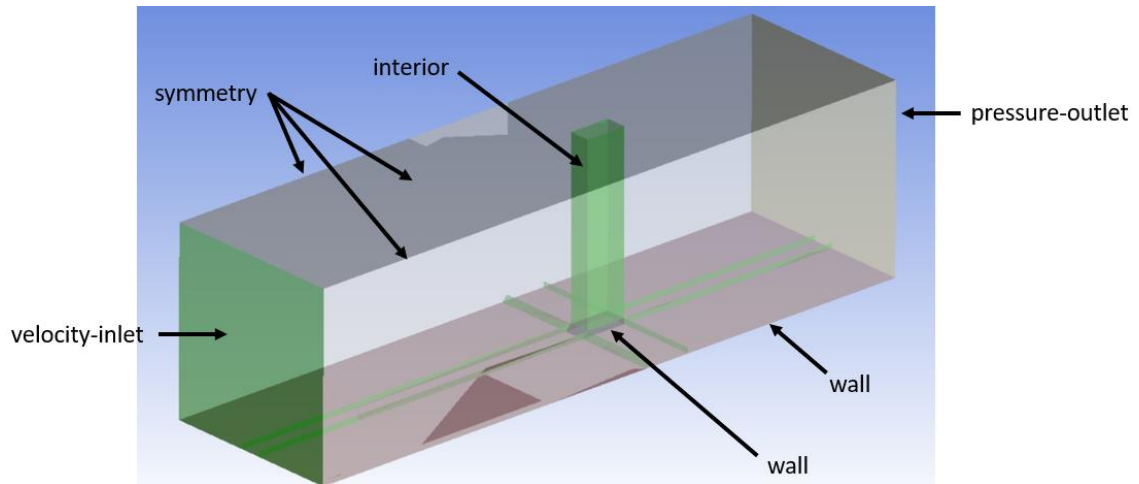


Figure 4-3: 3-D RFE Model Surface Boundary Conditions.

Material “bodies” were not necessary to create in 2-D because the only material used in the domain was the fluid, and the solid surfaces of the excrescence were modeled by simply deleting a block. In 3-D, a solid material family and fluid material family were created to separate the BLDS enclosure from the fluid. Additionally, the “solid” body can be readily changed to “fluid”, and its no-slip wall boundary conditions can be changed to interior for later simulation of boundary layer growth on the lower surface without any excrescence. A 3-D bounding box was applied around the entire domain, then split into 18 blocks as shown in Figure 4-4. The red block at the center of the domain was added to the solid material family and represents the RFE as it is positioned on the bottom wall of the domain. The blue blocks represent the surrounding fluid material family.

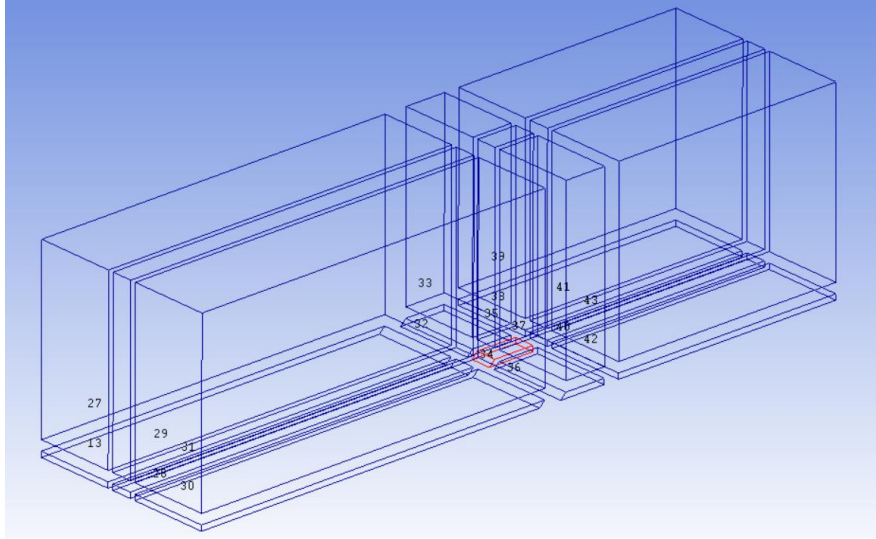


Figure 4-4: 3-D RFE Model Blocking and Material Families.

Using the mesh parameters from the 2-D domain as a starting point, a mesh independence study was conducted on the domain using the same reference and surface static pressure criteria described in Chapter 3. Four meshes with increasing numbers of grid points were produced for the domain shown above, and mesh independence was achieved with mesh containing about 600,000 grid points. Details of the mesh independence study are described in Appendix I. The resulting structured mesh is shown in Figure 4-5, with a clearer image of the mesh structure along the walls of the enclosure in the upper left.

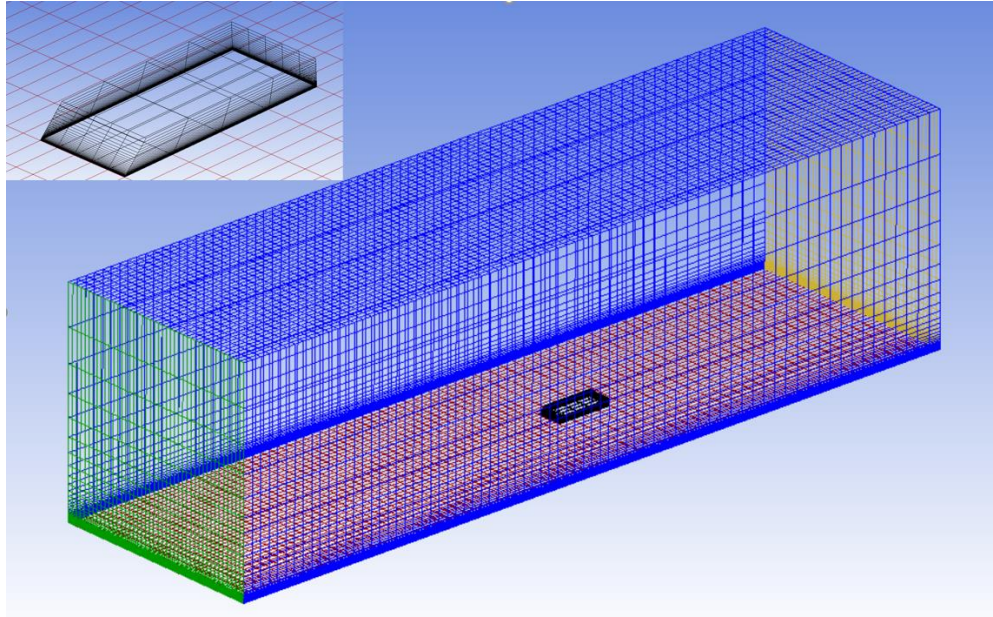


Figure 4-5: Converged Mesh Pattern for 3-D RFE Model.

The fine-grid convergence index, GCI_{fine} , was computed using three meshes of increasing grid density from the mesh convergence study. The computed GCI_{fine} for the 3-D enclosure mesh was computed using Richardson extrapolation²⁵ to be 1.2 % with an average order of accuracy of 1.3. This corresponds to an uncertainty in upstream surface C_p of ± 0.002 which varies slightly with upstream position as determined by computing GCI_{fine} at three different upstream locations. The details of the calculation at each upstream position are presented in Appendix H for reference.

The domain geometry, blocking and mesh patterns were recorded and rearranged in a working replay script that was used to alter h_D and w_D to achieve the desired free-air conditions. The converged mesh edge parameters were scaled with each change in h_D and w_D to maintain the converged mesh pattern shown in Figure 4-5. Several meshes with increasing domain height and width were produced and simulated

in FLUENT until the upstream surface static and reference static pressures no longer depended on those dimensions. The resulting free-air mesh, RFE-A, left the parameters of interest unconstrained by the boundaries of the domain with a height of $h_D \geq 108$ inches and width of $w_D \geq 60$ inches. Details of the height and width independence study as well as the free-air domain and its mesh edge parameters can be seen in Appendix I. As with the 2-D height independence, the free-air domain height and width are expected to scale with the excrescence height and width. However, the height of the ramped-front enclosure is not altered in the following 3-D simulations, so a height of 108 inches will be sufficient to model free-air in all cases. While the width of the enclosure is altered in section 4.2, it is only reduced from the value of w_e used in the width independence study. Therefore, a domain width of 60 inches is sufficient for all cases. The free-air domain was used to compute the upstream pressure disturbance and pressure drag coefficient for validation.

4.1.2 3-D Half-Scale Fairing

The second 3-D model was created for the BLDS half-scale fairing (HSF) positioned on a flat wall. A different approach was taken in the mesh structure for the fairing because it was imperative to capture the effect of the curvature on the upstream pressure disturbance and pressure drag. The blocking was first created in 2-D using a blocking style adapted from NASA Langley Research Center's turbulence modeling resource³¹. The blocking used for this study mimics geometry typically used to simulate free-air flow over a 2-D airfoil, but the trailing edge of the BLDS fairing is blunt rather than tapered to a point. The basic 2-D geometry is shown in Figure 4-6.

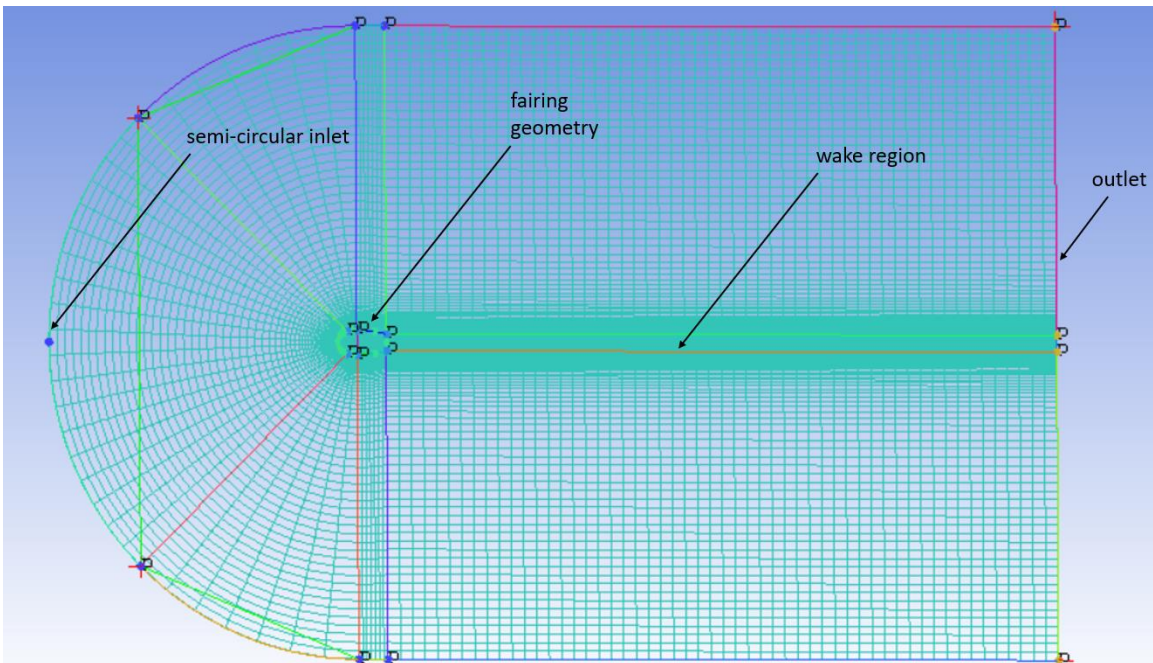


Figure 4-6: 2-D Fairing Domain Design Based on NASA Turbulence Modeling Resource³¹.

The blocking structure was extended into 3-D and largely created in the same fashion as the RFE model. The domain used for all 3-D HSF simulations is depicted below

with critical dimensions, and the surface boundary conditions are described in Figure 4-

8. The maximum width of the fairing is defined as w_f .

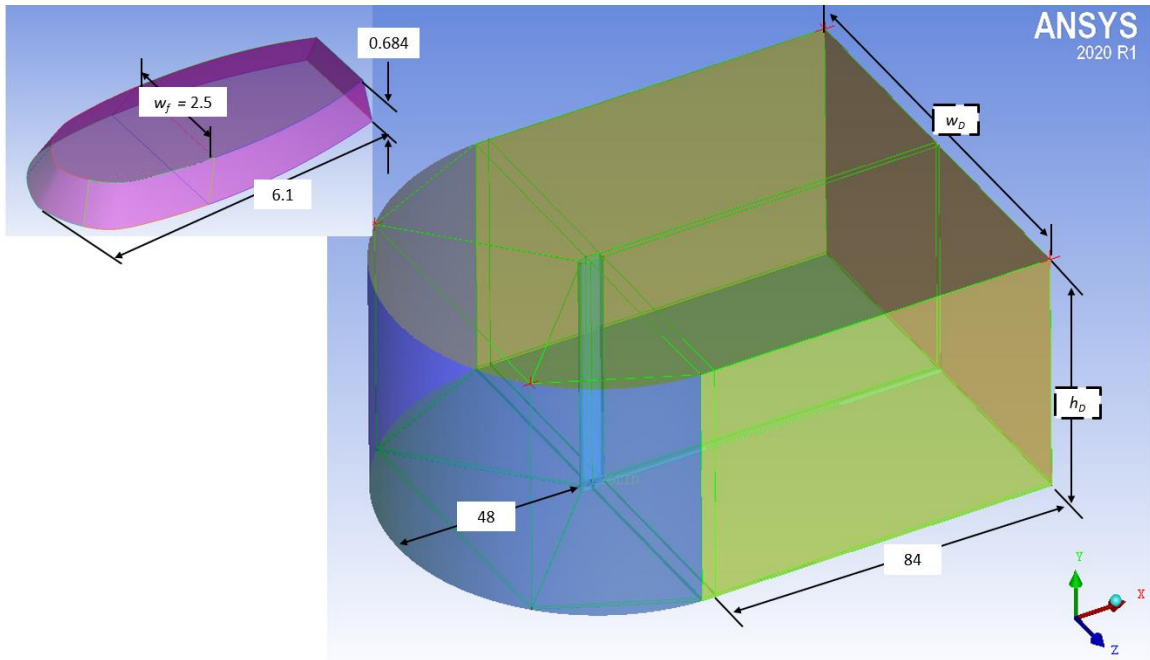


Figure 4-7: ICEM Geometry for 3-D HSF Model. Dimensions are in Inches.

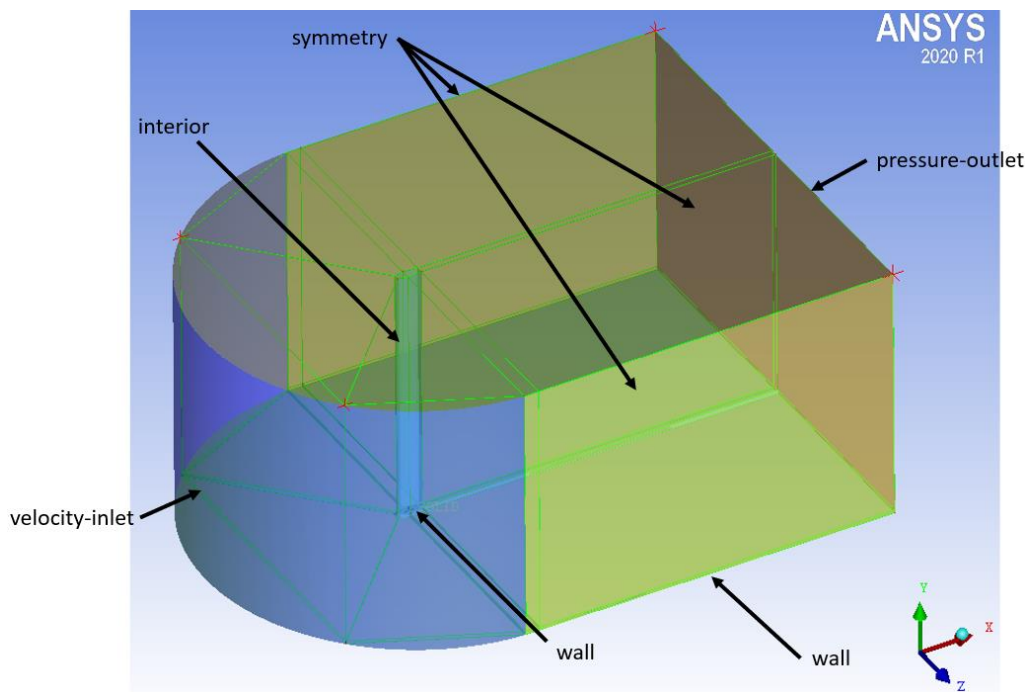


Figure 4-8: 3-D HSF Model Surface Boundary Conditions.

A mesh independence study was conducted for the HSF domain using three meshes with increasing numbers of grid points and mesh independence was achieved with a mesh containing about 1,000,000 grid points. Details of the mesh independence study are described in Appendix J. The GCI_{fine} for the 3-D HSF mesh was found to be 1.0 % with an average order of accuracy of 1.1. This corresponds to an uncertainty in upstream C_p of ± 0.0004 which varies slightly with upstream position as determined by computing GCI_{fine} at three different upstream locations. The details of the calculation at each upstream position are presented in Appendix H for reference.

The number of grid points specified along each edge of the converged domain was documented and carried through all 3-D CFD cases that include the BLDS half-scale fairing. The structured mesh output to FLUENT is shown in Figure 4-9, and a clearer image of the mesh structure along the sides of the fairing is at the lower right.

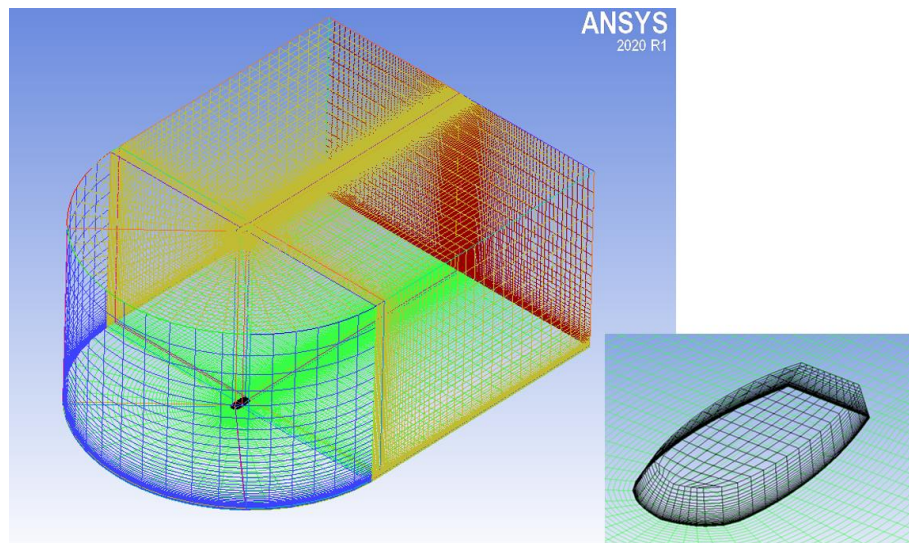


Figure 4-9: Converged Mesh Pattern for 3-D HSF Domain.

As with the 3-D RFE model, the HSF domain was optimized to simulate free-air flow, and the details of the height and width independence studies, the resulting HSF-A domain,

and its edge parameters can be found in Appendix J. The free-air domain was used to compute the upstream pressure disturbance and drag coefficient for validation.

4.2 3-D Case Set-Ups in FLUENT

Several different simulations were run in Ansys FLUENT using the free-air domains for the ramped-front enclosure and half-scale fairing. This section details the case set-up for the 3-D test cases and the results from each simulation. All FLUENT test cases are described in Table 4-2. The Mach number and Reynolds number per unit length for all 3-D CFD cases were maintained as 0.12 and $8.56 \times 10^5 \text{ ft}^{-1}$, respectively.

Table 4-2: 3-D CFD Cases

Case	Mesh	Excrescence	Excrescence Dimensions [in] <i>l x w x h</i>	Characteristic Area [in ²]	Ramp Angle [°]
1	RFE-A	Enclosure	6.17 x 2.78 x 0.732	2.03	45
2	HSF-A	Fairing	6.10 x 2.50 x 0.684	1.71	60
3	RFE-A	Removed	6.17 x 2.78 x 0.732	-	-
4	HSF-A	Removed	6.10 x 2.50 x 0.684	-	-
5	RFE-A	Enclosure	6.17 x 2.56 x 0.732	1.87	45
6	RFE-A	Enclosure	6.17 x 2.19 x 0.732	1.60	45
7	RFE-A	Enclosure	6.17 x 2.78 x 0.732	2.03	60
8	RFE-A	Enclosure	6.17 x 2.78 x 0.732	2.03	30

Cases 1-4 deal with validation of the 3-D CFD models, and Cases 5-8 are concerned with altering the RFE geometry to visualize its effect on the upstream pressure disturbance and pressure drag felt by the excrescence.

Preprocessing

Once each mesh file was read into FLUENT, a mesh check routine was run, and the steady state pressure-based solver was selected. The turbulence model was set to the S-A one-equation model and all model constants were left as the default values. The fluid in all cases is standard air as described in Chapter 3. The specific parameters assigned to each of the BC's from the model design section are described below.

Table 4-3: Boundary Conditions for 3-D RFE Cases

BC	Momentum		Thermal
	<i>Setting</i>	<i>User Specification</i>	<i>User Specification</i>
wall	Wall Motion	Stationary	No Heat Flux
	Shear Condition	No-slip	
	Roughness Model	Standard	
velocity-inlet	Specification Method	Normal to Boundary	Constant $T = 288.16$ K
	Velocity Magnitude (m/s)	41	
pressure-outlet	Specification Method	Normal to Boundary	Constant $T = 288.16$ K
	Gauge Pressure (Pa)	0	
	Prevent Reverse Flow	Yes	

Table 4-4: Boundary Conditions for 3-D HSF Cases

BC	Momentum		Thermal
	<i>Setting</i>	<i>User Specification</i>	<i>User Specification</i>
wall	Wall Motion	Stationary	No Heat Flux
	Shear Condition	No-slip	
	Roughness Model	Standard	
velocity-inlet	Specification Method	Components	Constant $T = 288.16$ K
	x-Velocity Magnitude (m/s)	41	
	y-Velocity Magnitude (m/s)	0	
	z-Velocity Magnitude (m/s)	0	
pressure-outlet	Specification Method	Normal to Boundary	Constant $T = 288.16$ K
	Gauge Pressure (Pa)	0	
	Prevent Reverse Flow	Yes	

Reverse flow was prevented on the pressure-outlets for both the fairing and enclosure models. Since the present work is not concerned with flow conditions far downstream, this was done to minimize convergence difficulties should the flow reverse direction at the outlet boundary. The HSF domain has a semi-circular inlet, so not all vectors normal to its boundary will be pointed in the x-direction. Therefore, the inlet velocity for the HSF domain was specified using velocity *components* in which only the x-velocity was specified instead of the normal to boundary specification method.

The solution methods used for the 3-D cases are slightly different than those used in the 2-D solution process. In particular, the pressure-velocity coupling scheme was changed from “SIMPLE” to “coupled” to aid in convergence.

Table 4-5: Solution Methods for 3-D CFD Cases

Solution Method	Setting	User Specification
Pressure-Velocity Coupling	Scheme	Coupled
Spatial Discretization	Gradient	Least Squares Cell Based
	Pressure	Second Order
	Momentum	Second Order Upwind
	Modified Turbulent Viscosity	Second Order Upwind

The pressure-based coupled algorithm solves the continuity and momentum equations simultaneously, which is often considered to have higher performance for 3-D flows than the SIMPLE algorithm and to be more robust and efficient for steady-state flows in general¹⁹. There are no strong body forces or natural convection in these analyses, and the mesh is packed tightly in regions of high gradient, so the solution is expected to be largely independent of pressure discretization. However, the second order pressure

discretization scheme was chosen for the 3-D test cases as it is considered more accurate than the standard or linear scheme should the pressure gradient at any cell face get too high¹⁹. Finally, the 3-D meshes, while still structured, are more irregular than the 2-D meshes from Chapter 3. For this reason, second order upwinding was chosen for discretization of momentum and the turbulence viscosity transport equation to avoid numerical diffusion²³.

Processing

Residual monitors for continuity, velocity components, and turbulence viscosity were set to 1×10^{-6} and each calculation was run with 3000 iterations. Convergence was reached for all 3-D cases within about 1500 iterations, and the scaled residuals for the velocity components and turbulence viscosity underwent more than five orders of magnitude of reduction over the course of each calculation. A well-converged solution was obtained for Cases 1 and 2 without making changes to the RFE-A or HSF-A meshes. However, the HSF-A mesh is much more irregular than the RFE-A mesh, so FLUENT'S solution-adaptive mesh refinement tool¹⁹ was used to iteratively refine the HSF-A mesh in regions of high pressure gradient. Very small pressure disturbances are of particular interest for the present work, so resolving areas in which there is a large change in pressure between cell volumes is critical to solution accuracy. Cells in which the pressure gradient was greater than 10% of the maximum pressure gradient¹⁹ in the domain were refined every 20 iterations. The mesh adaptation routine was run until no cells had pressure gradients higher than the specified value, then the mesh adaptation

tool was disabled, and the solution converged smoothly. The original free-air model including the fairing contained roughly 1.5 million cells (see Appendix J), and the adapted mesh included over 3 million cells. The resulting mesh pattern near the excrescence resulting from mesh adaptation is shown in Figure 4-10.

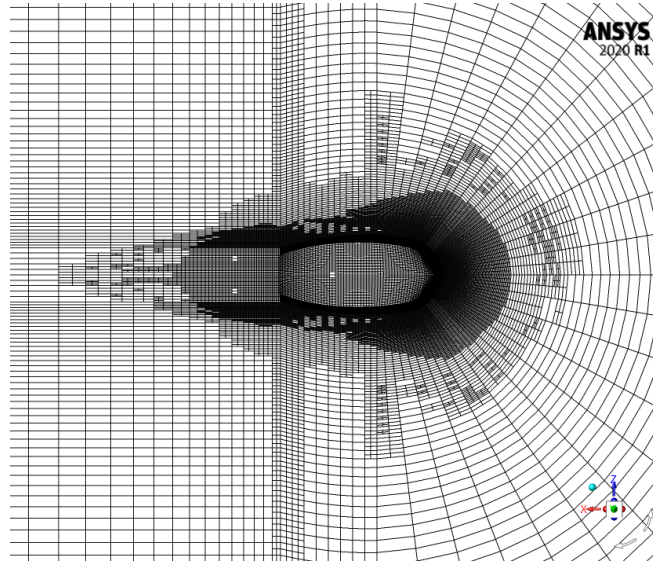


Figure 4-10: Adapted HSF-A Mesh.

Postprocessing

After each case was run in FLUENT the net mass imbalance between the inlet and outlet boundaries was checked, and the Reynolds numbers based on excrescence height, h , boundary layer thickness at the excrescence leading edge, δ , and excrescence leading edge location relative to the inlet, x_{le} , were compared for the 3-D computational domains and experiments from Chapter 2.

Table 4-6: Reynolds Numbers From 3-D CFD Cases and Wind Tunnel Experiments

		<i>Re based on Excrescence Height</i> Re_h	<i>Re based on Leading Edge δ</i> Re_δ	<i>Re based on Leading Edge Position</i> $Re_{x_{le}}$
Experiment	<i>Fairing</i>	4.50×10^4	5.85×10^4	2.18×10^6
	<i>Enclosure</i>	4.82×10^4	5.85×10^4	2.18×10^6
FLUENT	<i>Case 1</i>	5.22×10^4	6.81×10^4	3.42×10^6
	<i>Case 2</i>	4.88×10^4	6.35×10^4	3.42×10^6
	<i>Case 3</i>	5.22×10^4	6.81×10^4	3.42×10^6
	<i>Case 4</i>	4.88×10^4	6.35×10^4	3.42×10^6
	<i>Case 5</i>	5.22×10^4	6.81×10^4	3.42×10^6
	<i>Case 6</i>	5.22×10^4	6.81×10^4	3.42×10^6
	<i>Case 7</i>	5.22×10^4	6.81×10^4	3.42×10^6
	<i>Case 8</i>	5.22×10^4	6.81×10^4	3.42×10^6

As described in Chapter 2, the experimental measurements represent the difference between the surface C_p values with and without the excrescence in the tunnel, meaning some of the effects of the tunnel walls have been eliminated from the data. Therefore, comparing the results of “free-air” simulations to the experimental measurements should still show a high level of agreement. To assess the accuracy of the 3-D simulations, the upstream pressure disturbance from Cases 1 and 2 were compared to experimental measurements as shown in Figures 4-11 and 4-12.

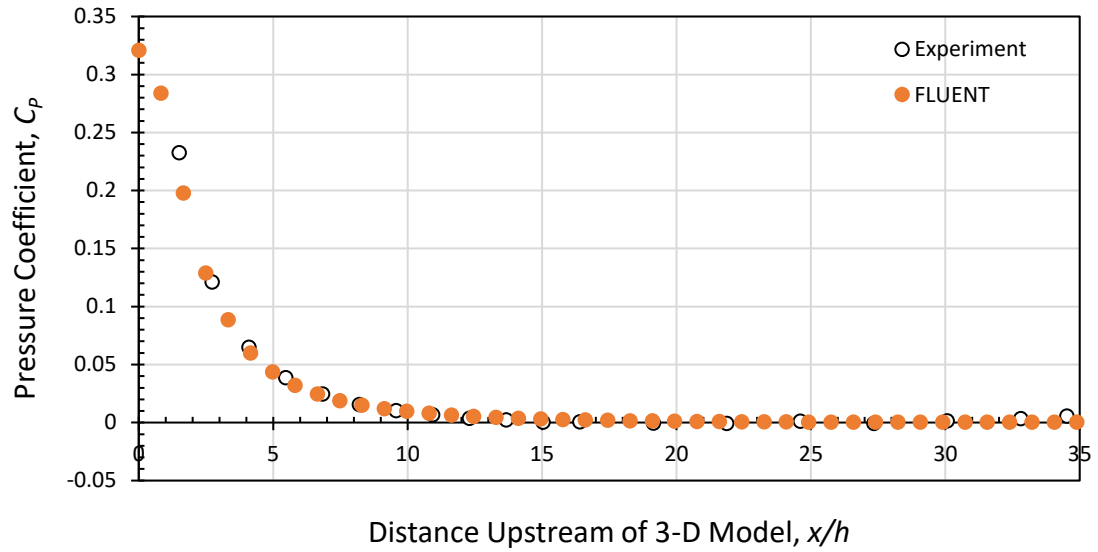


Figure 4-11: Computed Upstream C_p From 3-D Case 1 (RFE) Compared to Experiment.

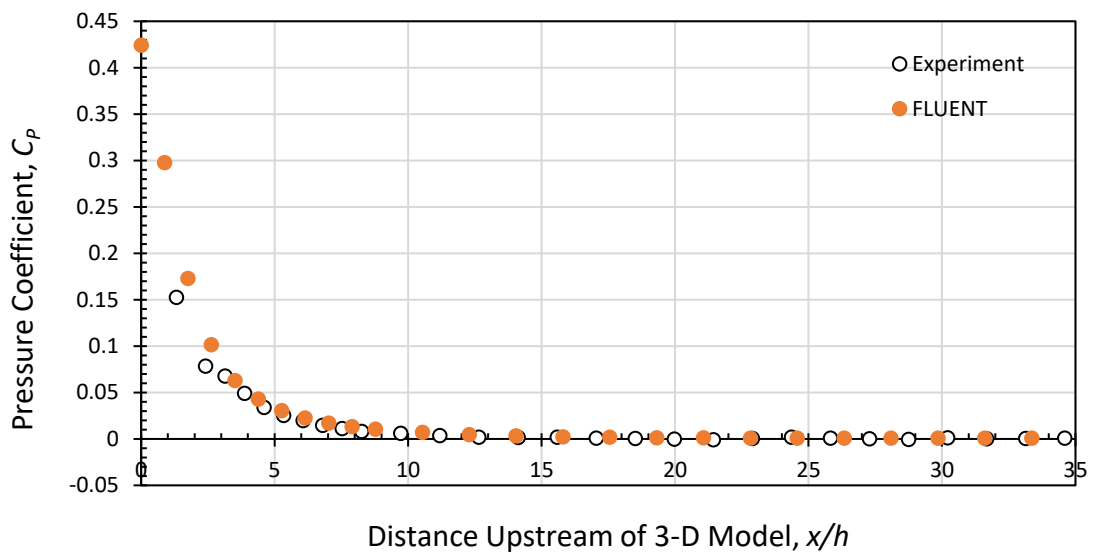


Figure 4-12: Computed Upstream C_p From 3-D Case 2 (HSF) Compared to Experiment.

The boundary layer thickness at the leading edge of the RFE was determined to be, $\delta \approx 0.84$ inches for Case 3. This is 0.05 inches thinner than the experimental $\delta \approx 0.89$ inches, even so, the S-A turbulence model produced a very comparable turbulent boundary layer shape.

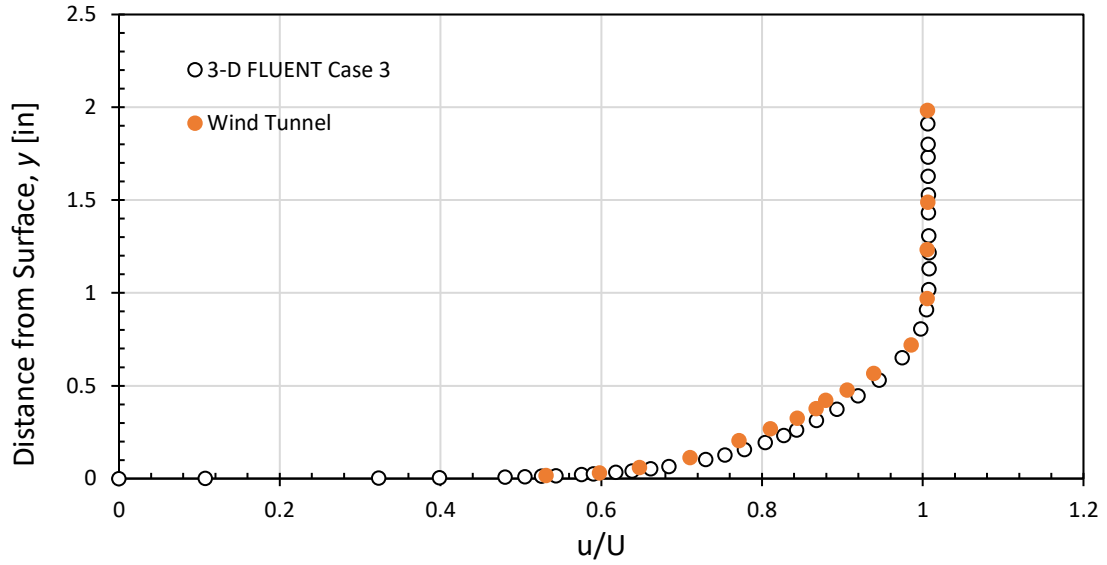


Figure 4-13: Boundary Layer Velocity Profile for Case 3 (RFE) Compared to Experiment.

The undisturbed boundary layer profile computed in Case 4 is shown in Figure 4-14, and the boundary layer thickness at the leading edge location without the HSF present was found to be $\delta \approx 0.90$ inches.

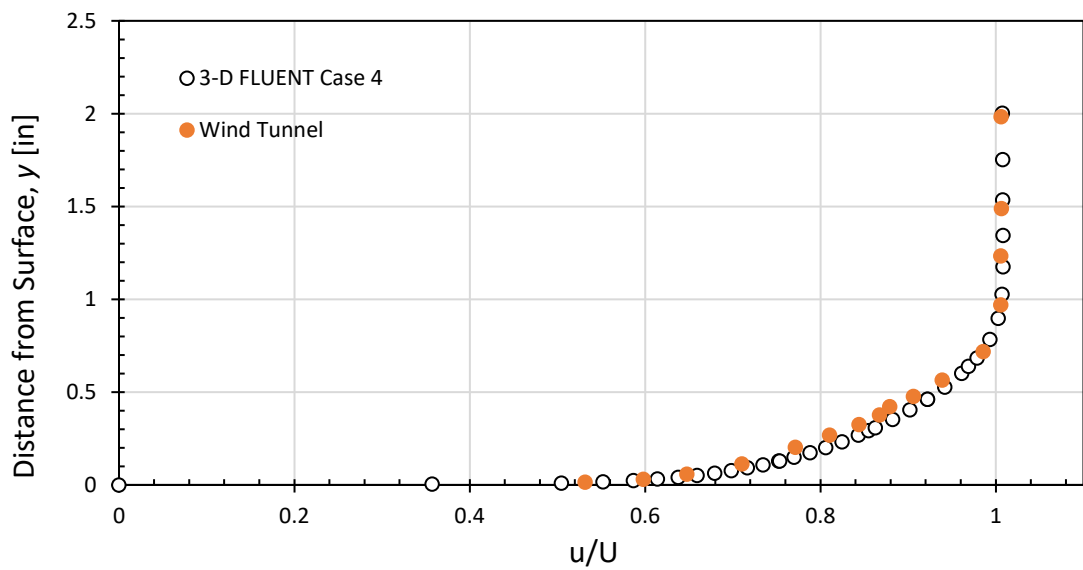


Figure 4-14: Boundary Layer Velocity Profile for Case 4 (HSF) Compared to Experiment.

The height of the enclosure and fairing are not changed throughout the following analyses, so the h/δ values presented in Table 4-7 can be considered constant for all enclosure and fairing cases.

Table 4-7: Height to Boundary Layer Thickness Ratios, h/δ , for 3-D CFD Cases

Excrescence	Experiment h/δ	FLUENT h/δ
RFE	0.824	0.869
HSF	0.770	0.762

In addition to validating the upstream pressure disturbance and boundary layer profiles, it was desired to validate the general 3-D flow characteristics as being realistic. This will help ensure no irregular mesh artifacts are skewing the results. For an object joined to a flat surface, the expectation is that the flow will be displaced away from the floor of the domain as the body is approached and a very small region of separated flow will appear upstream of the excrescence. Particle pathlines were generated in FLUENT along the center-plane for Case 1 to showcase this phenomenon. The small upstream region is enlarged in Figure 4-15B to show where the boundary layer separates from the upstream wall.

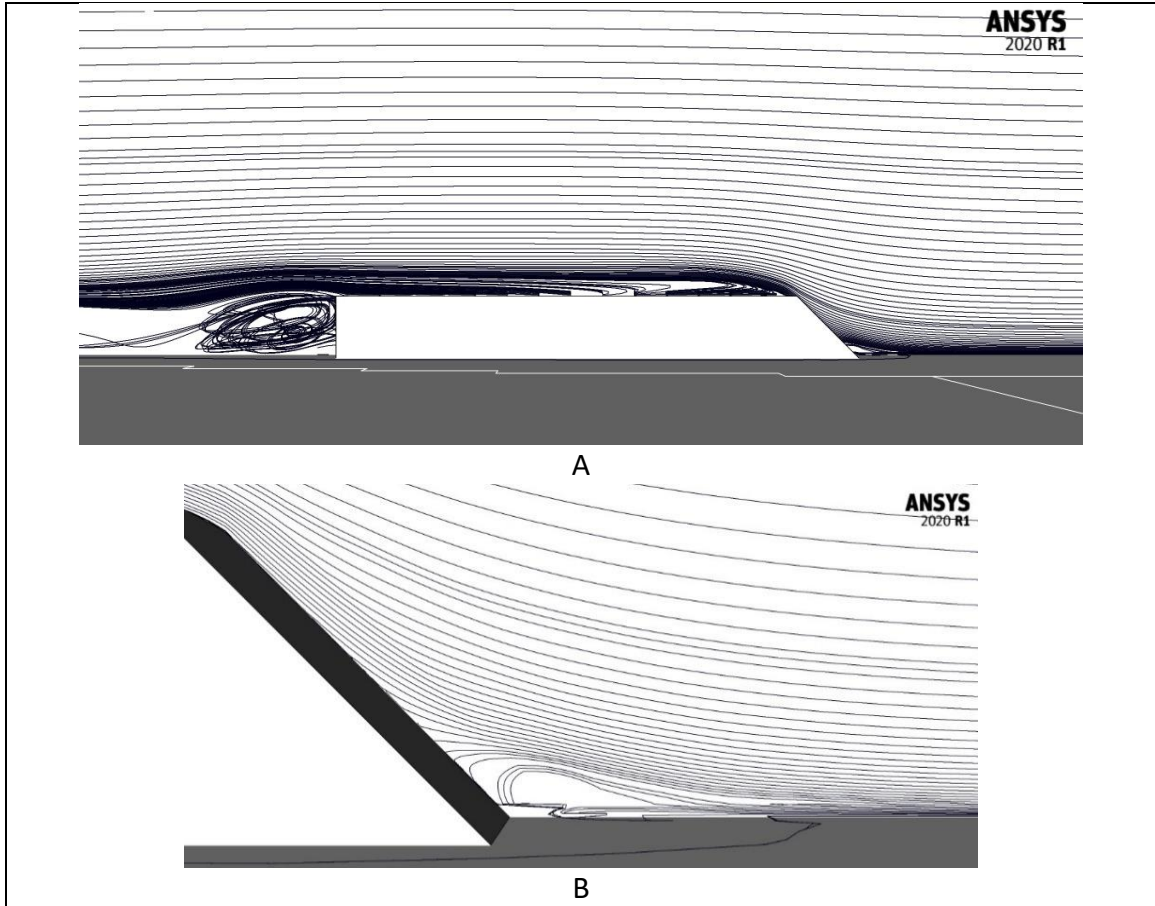


Figure 4-15: Center-Plane Particle Pathlines for Case 1 (RFE).

The particle pathlines upstream of the enclosure nose indicate that the boundary layer separates slightly less than 1 body height upstream. To showcase this, the upstream centerline C_f based on x -direction wall shear stress is plotted for several body heights upstream of the enclosure.

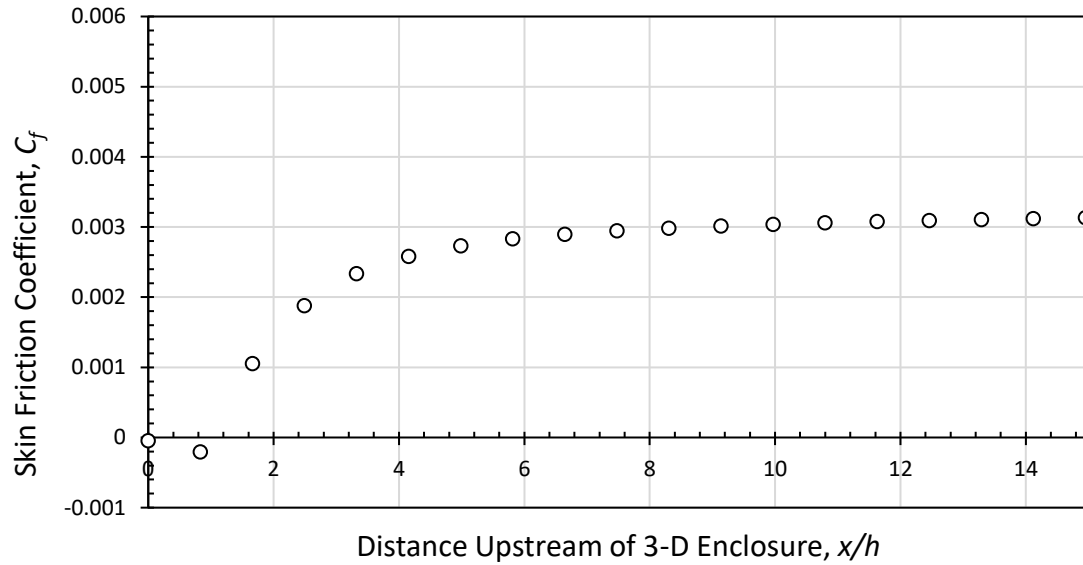


Figure 4-16: Upstream C_f From 3-D Case 1 (RFE).

Figure 4-16 shows $C_f = 0$ at about $x/h = 0.8$ which aligns well with expectations from fluid dynamic principles²¹. Additionally, it is expected that a second region of reversed flow occurs over the top of the excrescence²¹, and the pathlines in Figure 4-15A seem to depict that flow feature. The centerline C_f plotted in Figure 4-17 over the top surface of the RFE shows that there is indeed another small zone of separated flow. The flow appears to reattach about 3 inches aft of the leading edge of the enclosure and the C_f plot begins to have a negative slope near the trailing edge in anticipation of separation off the back of the excrescence. A similar trend occurs for the half-scale fairing geometry in Case 2.

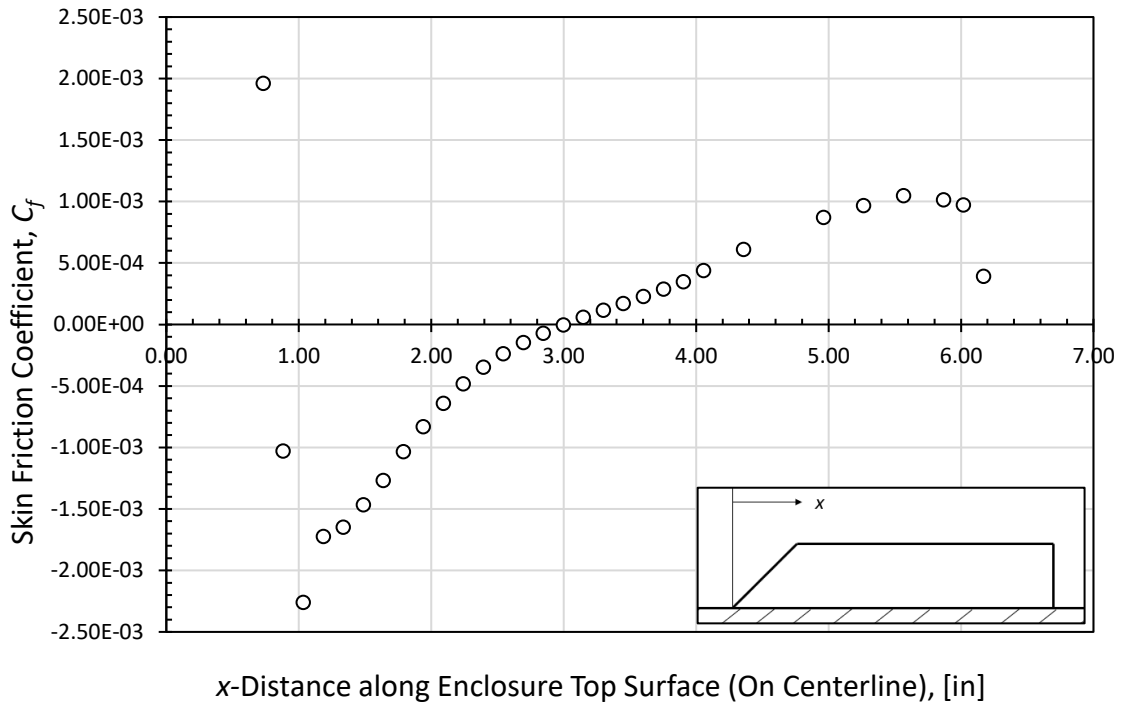


Figure 4-17: Surface C_f Along Top of RFE for 3-D Case 1.

The same flow visualization technique was used for Case 2 and the center-plane particle pathlines are presented in Figure 4-18 below. In Figure 4-18B, the sheet of fluid closest to the wall upstream of the half-scale fairing nose is reduced to zero velocity and subsequently reverses direction. The fluid particles flowing in reverse accumulate, the boundary layer thickness increases, the flow separates from the surface, and a vortex fills the resulting “dead” space⁵. As with Case 1, the flow appears to officially separate about 0.8 body heights upstream of the nose of the half-scale fairing as shown in Figure 4-19. The increasingly negative C_f values with proximity to the nose further demonstrate the vortex structure that appears in Figure 4-18B.

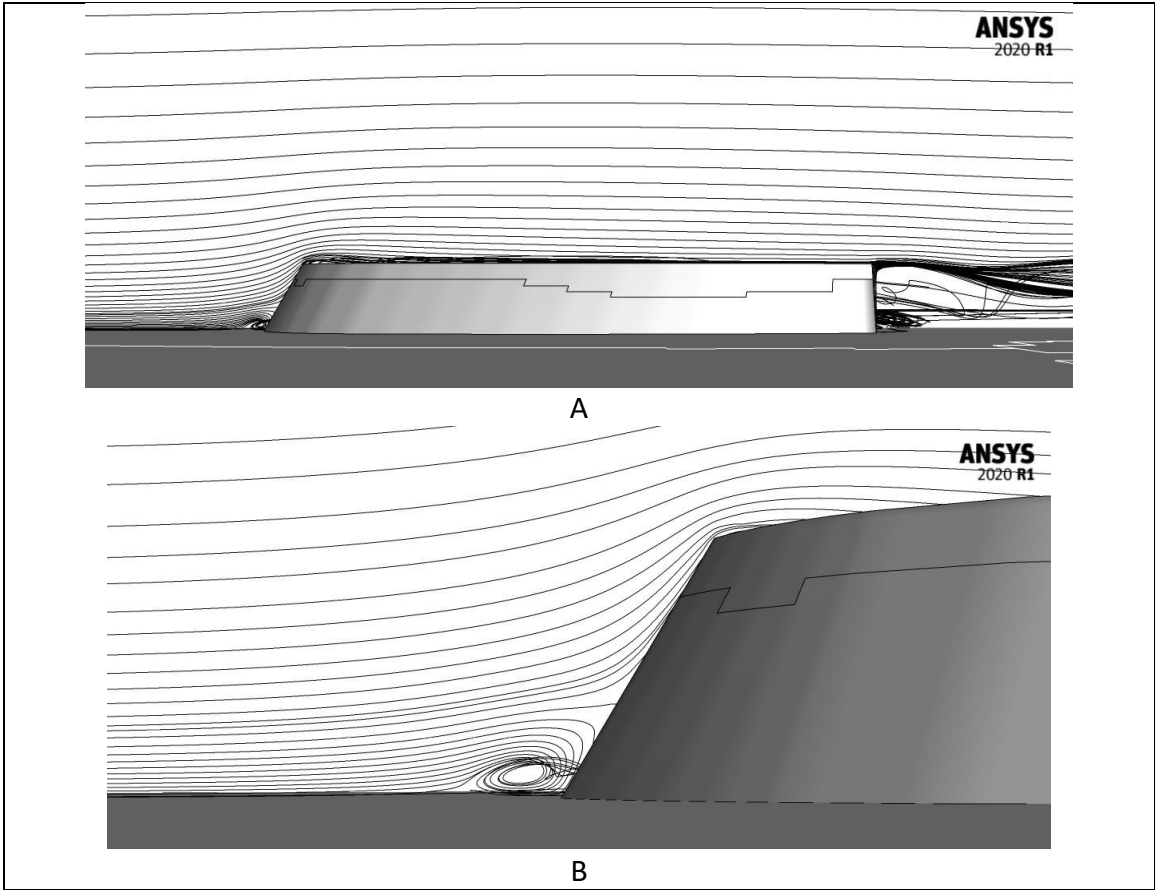


Figure 4-18: Center-Plane Particle Pathlines for Case 2 (HSF).

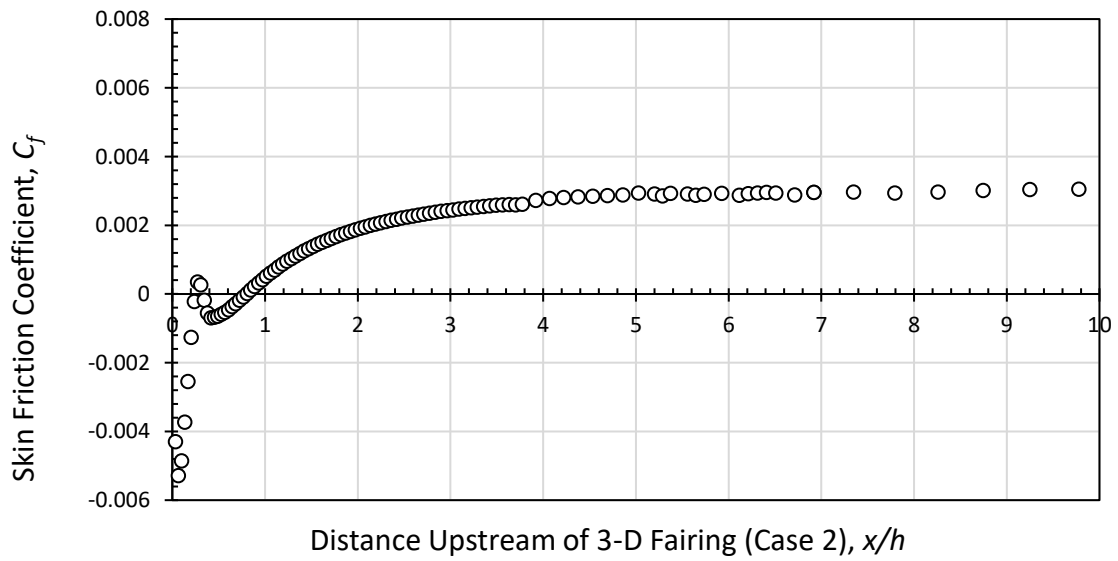


Figure 4-19: Upstream C_f From 3-D Case 2 (HSF).

For both Cases 1 and 2, the particle pathlines above also provide evidence that the computed flows captured a wake structure at the trailing edge of each excrescence. Just aft of each excrescence in Figures 4-15A and 4-18A the flow appears to be separated with a strong region of reversed flow along the centerline. In visualizing the particle pathlines for Case 1, a pair of vortices were observed in the wake region behind the enclosure. The pattern shown in Figure 4-20 aligns well with the classic flow pattern observed in the wake of blunt bodies, such as circular cylinders¹¹. The streamlines in steady flow past a circular cylinder are reproduced from G.K. Batchelor's *An Introduction to Fluid Dynamics*¹¹ for comparison to the 3-D CFD solution.

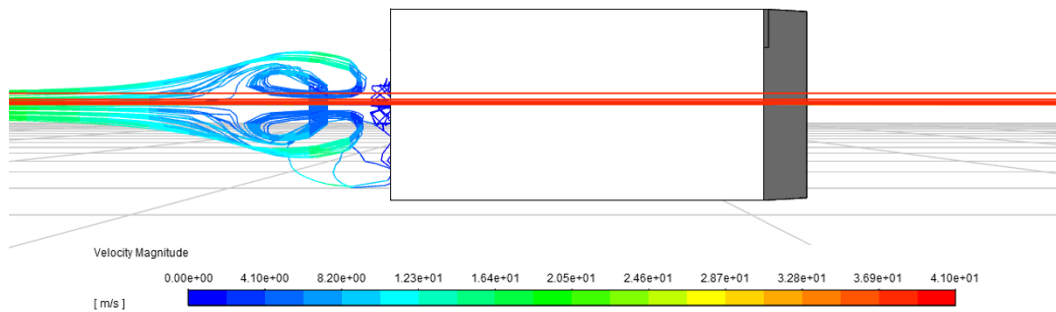


Figure 4-20: Pathlines Along the Center-Plane for Case 1 (RFE).

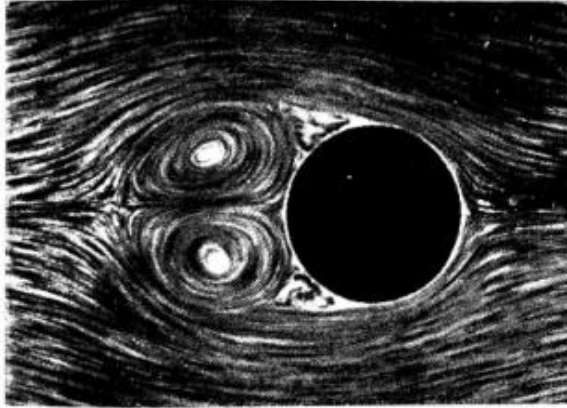


Figure 4-21: Streamlines Past a Circular Cylinder. Adapted From Batchelor¹¹ Figure 5.11.3.

A wholistic view of the flow pattern for the Case 1 ramped-front enclosure is depicted in Figure 4-22. The vortex behavior stops about 1 body width (2.78 inches) behind the enclosure, and the pathlines bend around the sides of the body and curve over its top as expected.

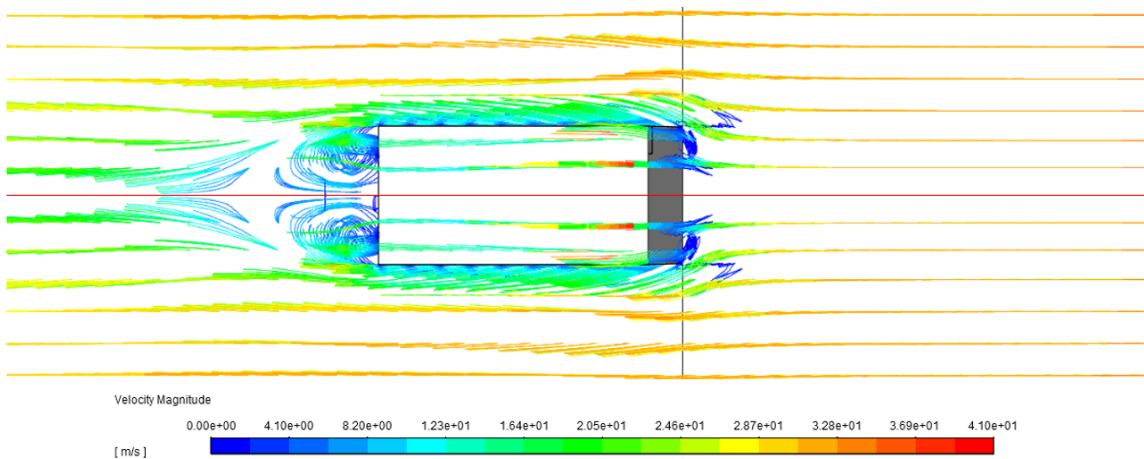


Figure 4-22: Top View of Case 1 Pathlines.

The pressure disturbance shown in Figures 4-11 and 4-12 above suggest that the pressure is highest right at the nose of each 3-D excrescence. The pressure contours for Case 1 substantiate this phenomenon. The contour lines are labelled with approximate values of upstream centerline C_p .

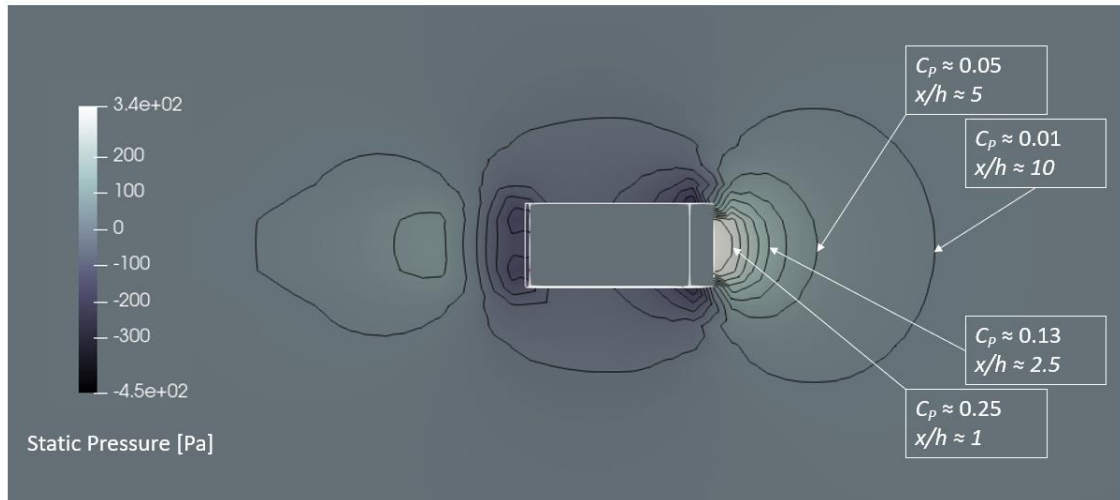


Figure 4-23: Contours of Surface Static Pressure for Case 1 (RFE).

The pressure coefficient at $x/h = 1$ shows that the pressure differential between p_x at the upstream surface and p_{ref} in the free stream is nearly 25% of the reference dynamic pressure. By $x/h = 2.5$, the disturbance to the pressure field has damped to about half of that. A C_p value of 5% or less may be used as a threshold at which the housing's disturbance to the pressure field becomes negligible⁶. As depicted in Figure 4-23, this occurs for the RFE at about 5 body heights upstream. However, for this thesis a C_p value of 1% or less will be used as the threshold to determine how far upstream a measurement device must be placed to be fully removed from the disturbed pressure

field. The 1% threshold appears to be reached for the RFE at about 10 body heights upstream. From Figure 4-12, the 1% threshold occurs for the HSF at about $x/h = 9$.

To assess the effect that the faired shape in Case 2 has on the upstream pressure disturbance compared to the original ramped-front enclosure from Case 1, the two sets of data were overlaid on the same axes.

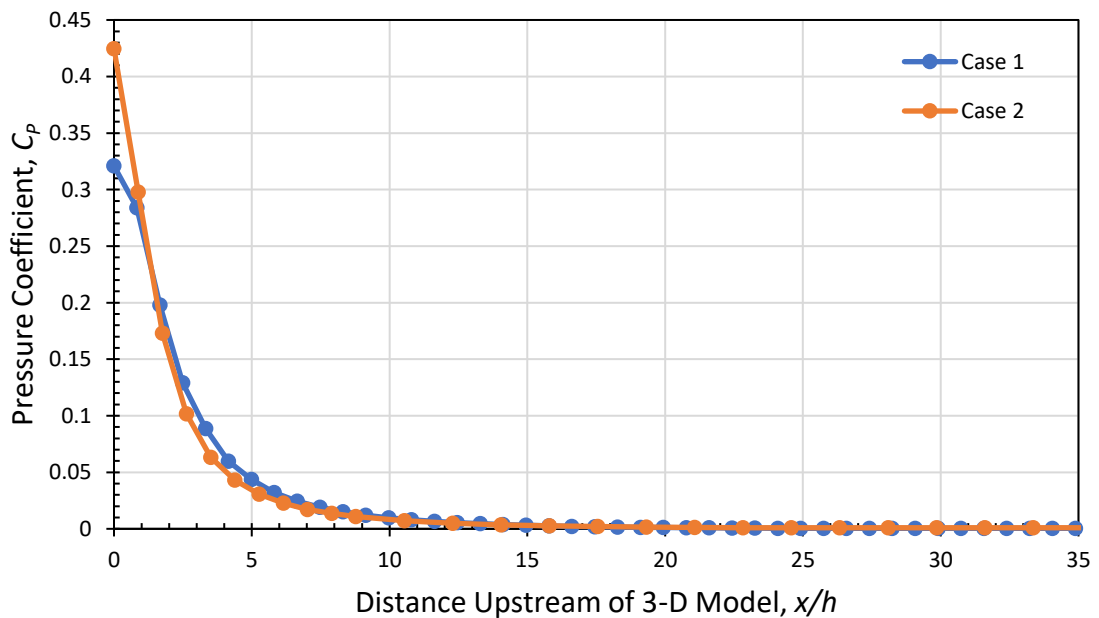


Figure 4-24: 3-D CFD Upstream C_p for Cases 1 and 2.

Figure 4-24 shows that there is no significant difference in the pressure disturbance caused by the enclosure (Case 1) and fairing (Case 2) upstream of $x/h \approx 6$. For about $1.5 \leq x/h \leq 6$, the difference in upstream C_p between that of the ramped-front enclosure and the half-scale fairing is larger than the previously reported uncertainty of ± 0.002 . In this region, the pressure disturbance caused by the enclosure is larger than that of the

fairing. However, for $0 \leq x/h < 1.5$, the HSF causes the larger pressure disturbance with a maximum C_p value at $x/h = 0$ of 0.42.

The experimental set-up described in Chapter 2 was not capable of capturing C_p values within 1 inch of the nose of each model because the distance between the static port on the traverse probe and the bend in the tube is approximately 1 inch. In other words, the tube collided the nose of the model before differential pressures within 1 inch of the model could be collected. Even so, the validity of the 3-D CFD solutions depicted in Figure 4-24 is substantiated by the upstream pressure disturbance experiments conducted by Cal Poly student Neil Sharma in 2018⁷. In the past experiments, the half-scale BLDS Fairing configuration afforded a smaller pressure coefficient than the BLDS-Satellite until about 1 inch upstream of the models. Within 1 inch of the BLDS Fairing, C_p became much larger than that of the BLDS-Satellite meeting a maximum value of $C_p \approx 0.415$, much like what is depicted in Figure 4-24.

Probes and sensors used for BLDS measurements may not always be placed directly upstream of the BLDS housing. Sometimes it is desirable or necessary to offset a rake or static pressure probe from the centerline. For this reason, the 3-D CFD solutions were used to estimate how far in the spanwise direction a device must be placed to avoid the disturbed pressure field. Spanwise cut-planes were created in FLUENT at 1, 5, and 10 body heights upstream of the enclosure and fairing, and the surface C_p values were plotted against their spanwise location from the centerline.

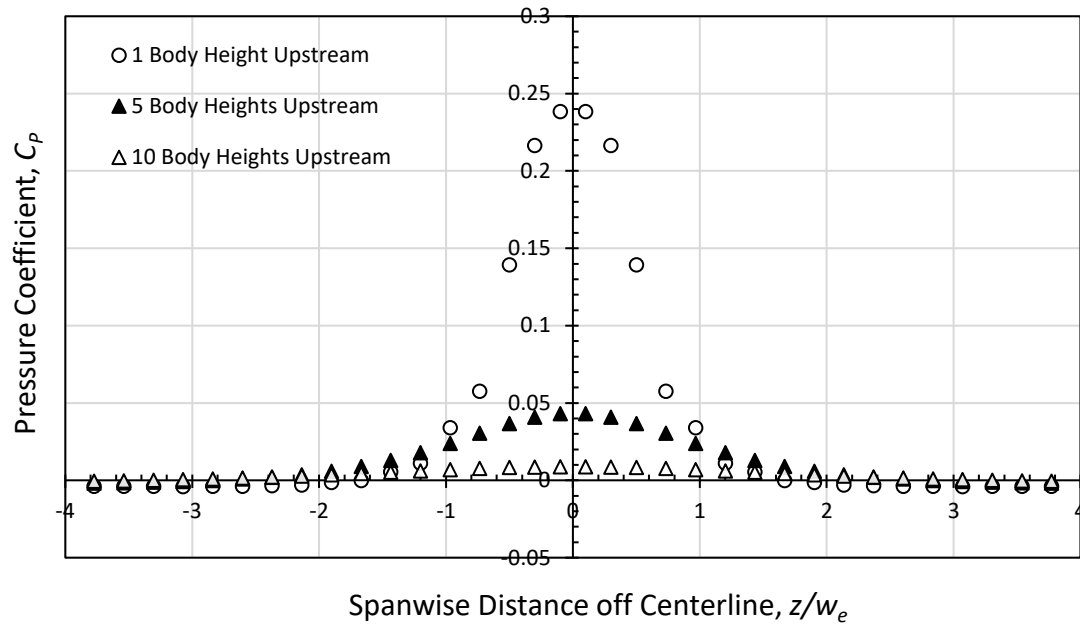


Figure 4-25: Spanwise C_p at Three Upstream Locations for 3-D Case 1 (RFE).

At 5 body heights upstream of the enclosure, the 1% threshold is reached about 1.5 body *widths* away from the centerline and about 1.3 widths away at 1 body height upstream. At 10 body heights upstream, all spanwise C_p values are smaller than 1%. The spanwise upstream pressure disturbance for Case 2 shows a similar trend.

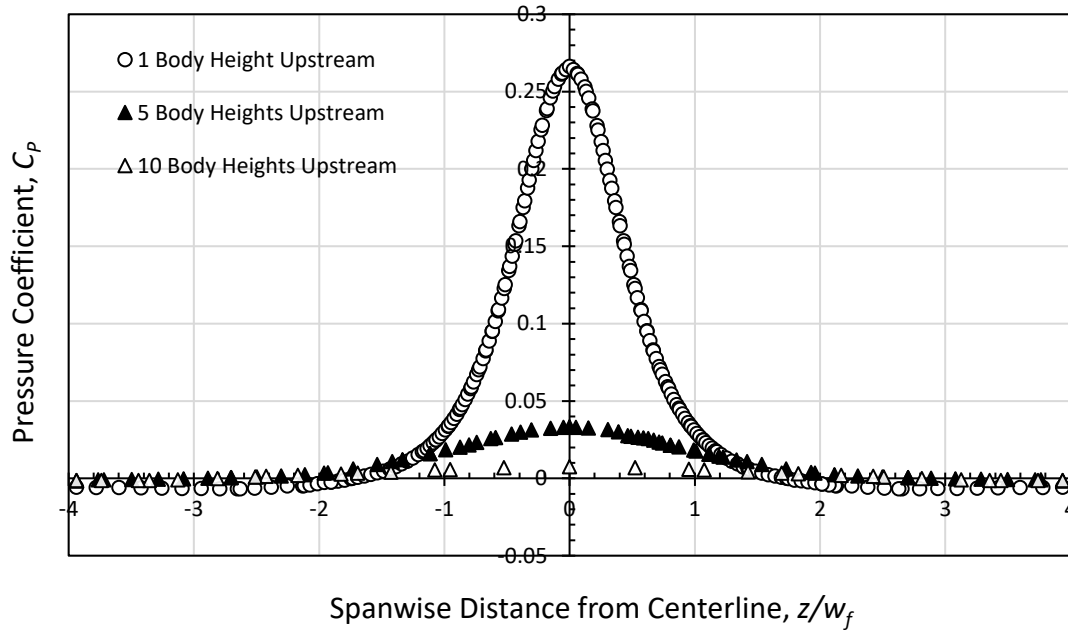


Figure 4-26: Spanwise C_p at Three Upstream Locations for 3-D Case 2 (HSF).

At 5 body heights upstream of the half-scale fairing, the 1% threshold is reached about 1.4 fairing widths away from the centerline and about 1.3 widths away from the centerline at 1 body height upstream. In general, there appears to be about 1-1.5 body widths of influence on either side of the centerline for both geometries.

The dimensionless drag force imposed on each excrescence was calculated in FLUENT using surface integrals of static pressure. The static pressure was integrated over the front surface and back surface of the 3-D enclosure as depicted in Figure 4-27. The sum of the integrated pressure on the front and back faces was then divided by the characteristic area for the Case 1 enclosure, and the reference dynamic pressure.

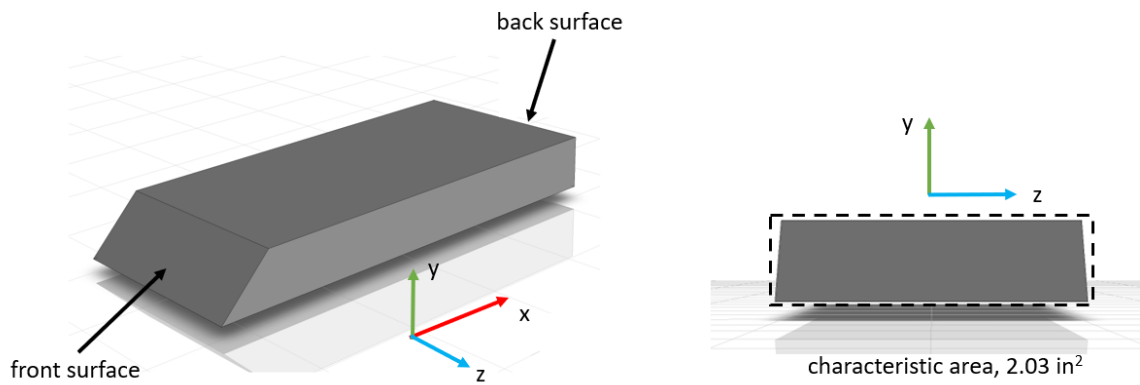


Figure 4-27: Surfaces Used to Integrate Static Pressure and Case 1 Characteristic Area.

Since the sides of the half-scale fairing are not parallel to the flow, the static pressure needed to be integrated on the front, back, and streamlined sides of the HSF to get a good estimate of the pressure drag. Figure 4-28 depicts the surfaces over which pressure was integrated and summed as well as the characteristic area used in the calculation of Case 2 pressure drag. The resulting pressure drag coefficients, C_{DP} , for Cases 1 and 2 are presented in Table 4-8.

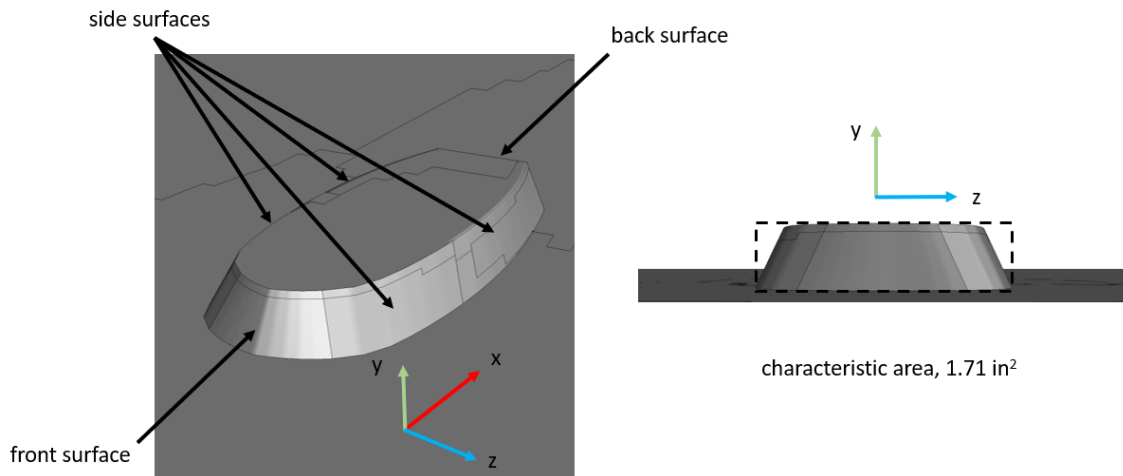


Figure 4-28: Surfaces Used to Integrate Static Pressure and Case 2 Characteristic Area.

Table 4-8: Pressure Drag Coefficients for 3-D Cases 1 and 2

Case	Pressure Drag Coefficient
	C_{DP}
1	0.516
2	0.296

Ultimately, the FLUENT simulations predicted pressure drag coefficients for each excrescence that match past experimental work. Past measurements of BLDS housing drag coefficients⁸ described in Chapter 1 indicate that the ramped-front enclosure housing has a drag coefficient of $C_D \approx 0.5$. The FLUENT results presented in Table 4-8 corroborate the experimentally determined C_D for the ramped-front enclosure in that the computed $C_D \approx 0.5$. The fairing geometry in the wake analysis experiment was manufactured at full-scale, so its C_D is not directly comparable to the half-scale fairing of FLUENT Case 2. However, the pressure drag coefficient calculated from the CFD results

is still approximately 0.3 which is expected based on the experimental C_D of the full-scale model.

As mentioned previously, there is not a significant difference in the pressure disturbance between Cases 1 and 2 unless attention is paid to the region where $x/h \leq 1.5$. Perhaps comparing the HSF and the RFE to each other is not strictly showing how well the streamlined sides in Case 2 work to reduce the upstream pressure disturbance. The ramped front of the enclosure model is at a 45° angle relative to the floor of the domain, whereas the fairing has a blunt nose, approximately 60° . To evaluate any effect that the ramped front may have on the C_p values in Case 1, the enclosure leading edge angle was increased to 60° without changing the enclosure height. The resulting upstream pressure disturbance was compared to the fairing results from Case 2.

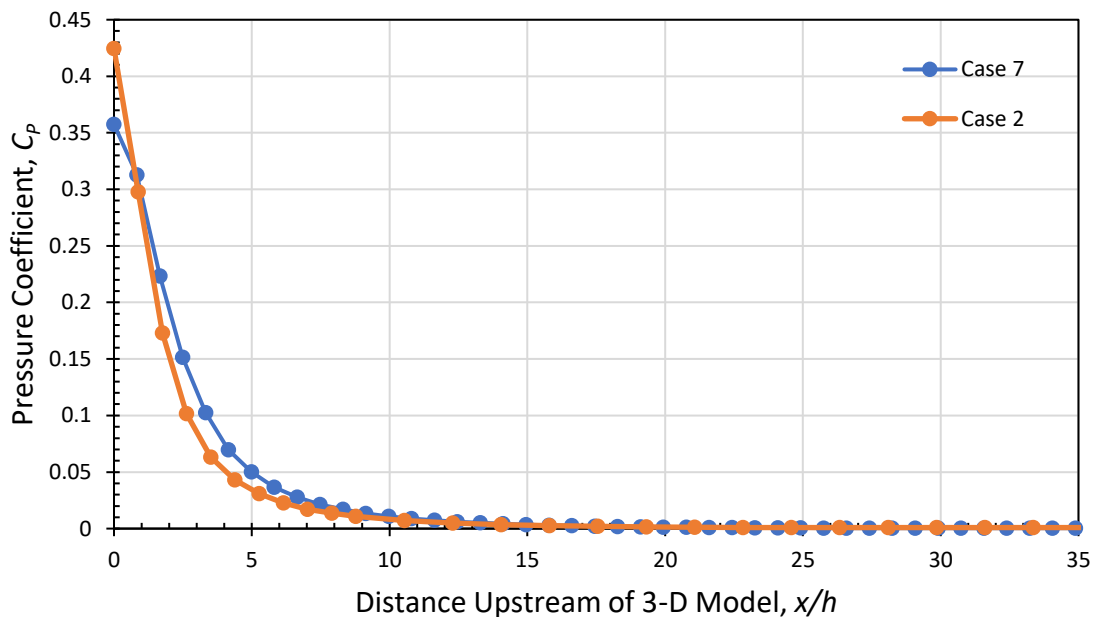


Figure 4-29: 3-D CFD Upstream C_p for RFE Case 7 (60° Ramp) and HSF Case 2.

After matching the nose angles of the enclosure and fairing, the difference in C_p exceeds 0.002 between the models for about $1 \leq x/h \leq 7$, which is slightly further upstream than depicted in Figure 4-24. However, there is no significant difference in C_p caused by the HSF (Case 2) and 60° RFE (Case 7) for $x/h > 7$. As shown in Figure 4-29, for $x/h \leq 1$, the half-scale fairing causes a larger pressure disturbance than the 60° ramped-front enclosure. This comparison shows that the difference in upstream pressure disturbance caused by the streamlined and blunt geometries is only significant within about $x/h = 7$ from the nose of each housing. However, it is important to note that the half-scale fairing was originally designed to be dropped on top of the RFE. At half-scale, the fairing's maximum height is about a 10th of an inch smaller than the RFE height, but if the fairing were printed at full-scale to house the RFE, its height would have to be larger than 0.732 inches. Therefore, in practice, it is likely that a full-scale BLDS fairing will disturb the pressure field more than the 3-D CFD solution in this thesis suggests. Future studies involving BLDS housing geometry should include a comparison of the pressure drag and upstream pressure disturbance for the full-scale fairing model.

The comparison in Figure 4-29 shows that the RFE ramp angle may impact how the enclosure geometry impacts the upstream pressure field. To explore this, the ramp angle was decreased to 30° without changing the height of the enclosure. The results were compared to that of Cases 1 and 7.

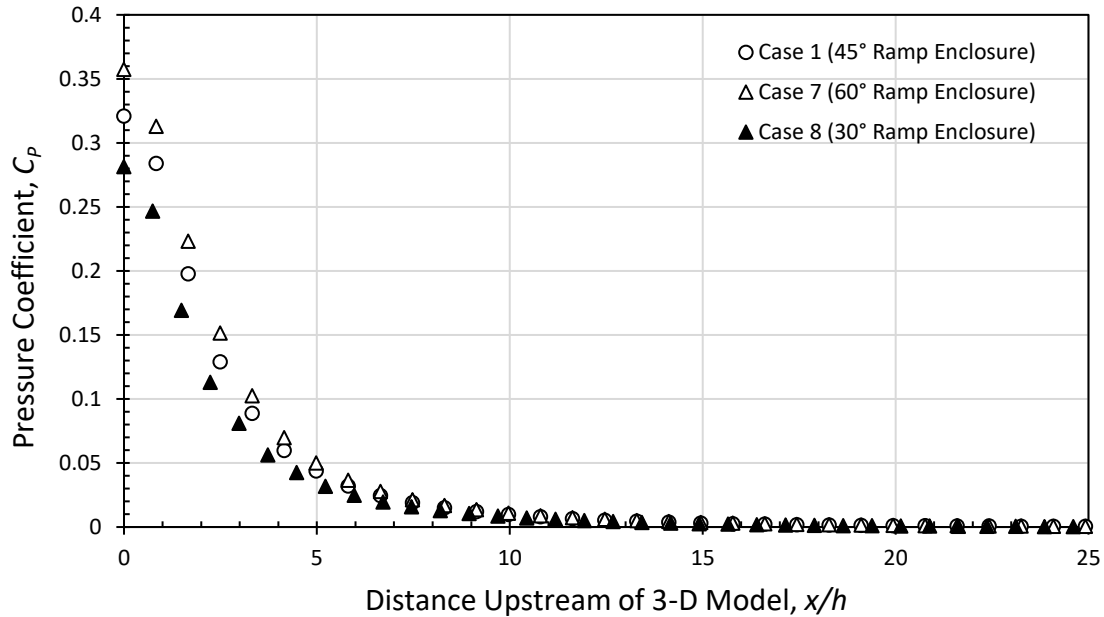


Figure 4-30: 3-D CFD Upstream C_p for Enclosure Cases 1, 7 and 8.

The 1% threshold for the enclosure in Case 8 (30° ramp) occurs at about 9.1 enclosure heights upstream. Additionally, the pressure disturbance grows more quickly on approach to the enclosure nose in Case 7 (60° ramp), than it does for Cases 1 and 8. The 1% threshold for the HSF geometry is the same as that of the 30° RFE geometry. However, the difference in pressure coefficient between Cases 1 and 8 does not become significant until $x/h = 6$. Further upstream from this, there is no significant difference in pressure disturbance caused by the different ramp angles. Likewise, the difference in pressure coefficient between Cases 1 and 7 only exceeds ± 0.002 at $x/h \approx 5$, with no significant difference in pressure disturbance further upstream. For $0 \leq x/h \leq 5$, the 60° ramped-front enclosure causes the largest disturbance to the pressure field followed by the 45° ramped-front enclosure and the smallest disturbance is caused by the 30° ramped-front enclosure.

Finally, the aspect ratio of the RFE was changed to explore how the body width influences the upstream pressure field. The original enclosure of Case 1 has a projected frontal aspect ratio of approximately 3.8. The width of the body was reduced while keeping the height and ramp angle constant to produce an enclosure with an aspect ratio of 3.5 (Case 5) and 3.0 (Case 6).

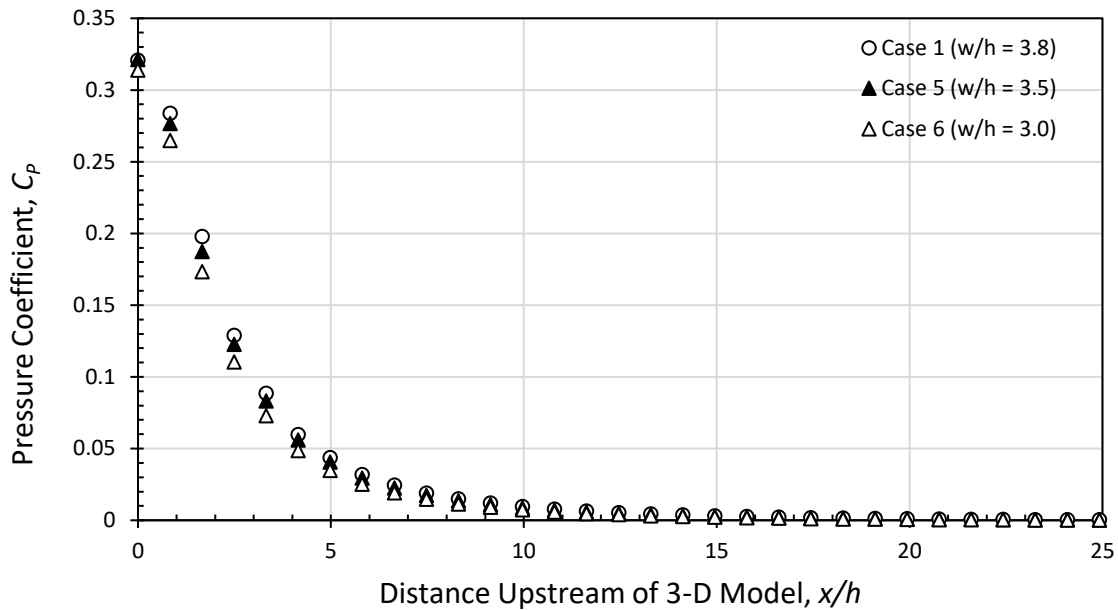


Figure 4-31: 3-D CFD Upstream C_p for Cases 1, 5 and 6.

Changing the enclosure width begins to influence the pressure field at about 8 enclosure heights upstream but has little effect on the value of C_p directly at the nose of the enclosure. Case 5 reaches $C_p = 1\%$ at about 9.5 enclosure heights upstream, and Case 6 at 8.8 enclosure heights affording Case 6 the smallest upstream pressure disturbance on a per excrescence height basis. Much like the results from changing the leading edge angle, there is no significant difference in pressure disturbance caused by the different aspect ratios for $x/h > 5$. For $0 \leq x/h \leq 5$, the 3.0 aspect ratio enclosure consistently

causes the smallest disturbance to the pressure field with a maximum C_p value at $x/h = 0$ of 0.31. The maximum C_p values at $x/h = 0$ for Cases 1 and 5 are the same.

In summary, the half-scale fairing of Case 2 has proven to experience the smallest C_{DP} for the flow scenario regardless of how the enclosure geometry was changed. The Table 4-9 summarizes relevant figures of merit for each 3-D FLUENT case.

Table 4-9: 3-D FLUENT Pressure Disturbance and Pressure Drag Results by Case

Case	Excrescence	Ramp Angle [°]	Excrescence Width [in]	1 % Threshold Upstream <i>Body Heights</i>	Pressure Drag Coefficient C_{DP}
1	Enclosure	45	2.78	9.9	0.52
2	Fairing	60	2.50	9.1	0.30
5	Enclosure	45	2.56	9.5	0.52
6	Enclosure	45	2.19	8.8	0.51
7	Enclosure	60	2.78	10.3	0.50
8	Enclosure	30	2.78	9.1	0.54

For all geometries, regardless of their shapes, the 1% threshold in the computed upstream pressure disturbance occurred at about 8-10 body heights upstream which agrees with previous student work⁷. In the region of about $x/h < 1$, Case 8 proved to have the smallest disturbance to the pressure field followed closely by Case 6. Cases 6 and 8 were also shown to have the smallest pressure drag of all the RFE geometries studied. The 3-D CFD solutions for the RFE models suggests that reducing the ramp angle at the leading edge of the enclosure or the aspect ratio are both viable options for not only reducing the pressure disturbance upstream of the BLDS, but also the drag force on the enclosure. Ultimately, if there is no concern for the pressure field as it is disturbed very near the nose of the BLDS, the fairing shape will incur the smallest

pressure drag coefficient. However, there is not a significant difference between any enclosure configuration and the fairing when it comes to pressure disturbance beyond 6 body heights upstream of the excrescence. Future studies would benefit from exploring how that translates to a full-scale fairing meant to house some version of the RFE. If the BLDS configuration requires instruments be mounted to the nose of the housing, the fairing geometry may cause too much disturbance to get accurate readings. In this scenario, reducing the aspect ratio of the classic enclosure shape or decreasing the ramp angle would be more effective, but only slightly.

5. CONCLUSIONS AND RECOMMENDATIONS

Ansys ICEM CFD and FLUENT were used to model and compute air flow upstream of two BLDS main unit housings. The upstream pressure disturbance and pressure drag incurred on the housings were calculated with the intent of answering two main questions:

1. Can CFD methods accurately compute the flow near small excrescences like the BLDS?
2. How effective are the current BLDS housings at limiting pressure field disturbance and imposed pressure drag?

To address these driving questions, wind tunnel tests were first conducted in Cal Poly's 2x2 ft wind tunnel with 2-D and 3-D BLDS housing models to obtain measurements of the upstream pressure disturbance. Prior to modeling the flow with viscous CFD, potential flow theory was used to compute the upstream pressure disturbance. ICEM CFD was used to generate mesh parameters for 2-D and 3-D models, then FLUENT was used to solve the RANS equations in conjunction with the Spalart-Allmaras turbulence model for the 2-D and 3-D geometries. The computed flow features, and results for dimensionless pressure and drag, were compared to experimental measurements and classic aerodynamic principles to evaluate the CFD solutions. Finally, the BLDS housing geometry was modified to evaluate how the pressure disturbance and pressure drag are affected by housing shape.

5.1 Conclusions

This section summarizes the key results and important conclusions from these studies.

5.1.1 2-D CFD Conclusions

The inviscid analysis from Chapter 3 showed that for excrescences of C/W approximately 2-6, potential flow theory gives a reasonable estimate of the actual viscous upstream pressure disturbance. Agreement between the 2-D inviscid solution and 2-D wind tunnel surface C_p measurements improved with distance upstream of the model leading edge. This shows that most of the upstream pressure disturbance caused by the main unit is inviscid, and only minimal effects of viscosity are seen near the nose of each excrescence.

Additionally, the 2-D FLUENT results showed good agreement with the experimental measurements described in Chapter 2 and accurately represent the expected flow structure for an excrescence mounted to a smooth wall. When compared to the 2-D inviscid solution, the 2-D viscous CFD solutions replicated the trend seen between the potential flow solution and 2-D wind tunnel measurements. This demonstrates that using a pressure-based RANS solver with the Spalart-Allmaras turbulence model is an effective method for not only capturing the effects of viscosity near the nose of a 2-D excrescence, but also the inviscid behavior far upstream.

The 2-D upstream pressure disturbance and pressure drag are linked to excrescence height. In the 2-D experiments, inviscid analysis, and CFD, the tall 2-D model consistently produced a larger upstream pressure disturbance than the short model for $x/h \leq 5$. The

tall model solution gave a maximum C_p at $x/h = 0$ of 0.45 and the short model gave $C_p = 0.33$ at the same location. However, for $x/h > 5$, no significant difference in the pressure disturbance caused by the tall and short 2-D models was observed in the computed results. In addition, the C_{DP} values computed in FLUENT appeared to increase with an increase in h . The method of adding the integrated pressure for each surface normal to the flow direction gave $C_{DP} = 0.70$ for the tall model and $C_{DP} = 0.48$ for the short model. However, the computed boundary layer thicknesses from the TB and SB meshes were not the same, nor were the local Reynolds numbers. Therefore, it can be concluded that the pressure drag coefficient increased with h/δ which agrees well with the expectation described in Hoerner's *Fluid Dynamic Drag*⁵.

Finally, the 2-D wall-bounded CFD solutions gave smaller values of C_p than the free-air solutions, suggesting solid blockage effects are present in the computations. At about 10 body heights upstream, the shorter excrescence shows $\Delta C_p \approx 0.008$ between the wall-bounded and free-air domain whereas the taller model saw $\Delta C_p \approx 0.02$ at this location. These differences are small, but larger than the extrapolated uncertainty in C_p (± 0.005), therefore significant enough to consider in wall-bounded modeling. For $x/h < 1$, solid blockage effects did not have a significant impact on the pressure disturbance.

5.1.2 3-D CFD Conclusions

In 3-D, the primary comparison was made between two existing BLDS housings: the ramped-front enclosure and the half-scale fairing. The computed upstream pressure disturbance for both housings showed a high level of agreement to the experimental

measurements described in Chapter 2. Likewise, the computed boundary layer profiles in the absence of each 3-D excrescence showed agreement with the measured profile from the wind tunnel in both thickness and overall shape.

Additionally, the 3-D CFD models reasonably computed the expected flow phenomena for a small excrescence on an otherwise smooth surface. Specifically, upstream boundary layer separation characterized by $C_f \leq 0$ occurred for both the enclosure and fairing geometries at about $x/h = 0.8$. For both housing geometries, a small region of reversed flow upstream of the nose was visible in the center-plane particle pathline pattern. The 3-D CFD solutions also captured a second zone of separated flow across the excrescence tops with reattachment and a separated wake region behind both excrescence geometries, all of which are expected features described in Hoerner's *Fluid Dynamic Drag*⁵ for flow over small, blunt excrescences. Post-processing of the enclosure model calculations showed a pathline pattern very similar to the classic flow pattern observed in the wake of blunt bodies from G.K. Batchelor's *An Introduction to Fluid Dynamics*¹¹. These observations demonstrate that FLUENT can accurately compute air flow over small excrescences, and that the meshes created in this thesis were adequate to compute the flow accurately.

Comparing computed results for the RFE and the HSF housings showed that there is no significant difference in upstream C_p for $x/h > 6$. For about $1.5 \leq x/h \leq 6$, the enclosure caused a slightly larger disturbance to the pressure field, but for $0 \leq x/h < 1.5$, the fairing caused the larger disturbance. This trend is corroborated by past experimental measurements⁷ of upstream C_p for the half-scale fairing geometry. Even

when the leading edge angle of the enclosure was changed to match that of the fairing, the difference in far upstream ($x/h > 7$) pressure disturbance for the two housings was not significant enough to suggest that housing shape had any effect on the upstream surface pressure disturbance.

Similar behavior was observed with changing the ramp angle and aspect ratio of the enclosure. For $0 \leq x/h \leq 5$, the 60° ramped-front enclosure caused the largest disturbance to the pressure field followed by the 45° ramped-front enclosure and the smallest disturbance is caused by the 30° ramped-front enclosure. However, no significant difference in how each excrescence disturbed the pressure field was observed for $x/h > 5$. Likewise, $0 \leq x/h \leq 5$, the modified enclosure with $w_e/h = 3.0$ (Case 6) caused the smallest disturbance to the pressure field followed by the $w_e/h = 3.5$ and $w_e/h = 3.8$ enclosures, with no significant difference in C_p for $x/h > 5$. Changing the enclosure width was observed to have no effect on the value of C_p directly at the nose of the RFE.

Another useful result from this work is that the computed spanwise pressure disturbance between $1 \leq x/h \leq 10$ was found to consistently damp to $\leq 1\%$ of the dynamic pressure at 1-1.5 body widths away from the centerline. This behavior was demonstrated by both the enclosure and fairing geometries and will be useful to inform placement of BLDS probes and sensors when it is necessary to offset them from the centerline.

Finally, all computed enclosures, regardless of how their shapes were altered, resulted in a pressure drag coefficient of about 0.5 which agrees well with the

experimental values reported in 2017⁸. The half-scale fairing simulation also resulted in a comparable value of $C_{DP} \approx 0.3$ which shows that using FLUENT to compute the pressure drag coefficient is a reliable method for estimating the loads on small excrescences like the BLDS. In the future, using the pressure drag coefficient from a CFD model could be used to inform design decisions related to BLDS adhesion methods after applying the appropriate factors of safety.

Keeping the above findings in mind, the driving questions for this work can be answered:

Can CFD methods accurately compute the flow near small excrescences like the BLDS?

Yes. This thesis demonstrates that CFD in both 2-D and 3-D can accurately compute upstream pressure disturbances and pressure drag for excrescences mounted to a smooth surface. The calculations from FLUENT agree well with the experiments described in Chapter 2. That combined with reasonable estimates for the drag coefficient, agreement with inviscid analysis, and representation of flow structures expected from classic aerodynamic principles shows that the CFD can serve as a reliable tool for future work. FLUENT is a user-friendly CFD software, is well-known in industry, and has extensive documentation available for its use. This thesis has set-up a working FLUENT CFD case that can be used for future computational studies related to the BLDS and provides guidance for some representative BLDS main unit shapes beyond the rules of thumb currently used for informing housing designs.

How effective are the current BLDS housings at limiting pressure field disturbance and imposed pressure drag?

Ultimately, if the goal is to reduce the drag on the excrescence, the fairing geometry is the most effective main unit housing shape. The computed pressure drag coefficient for the HSF geometry was consistently smaller than that of the RFE regardless of how the enclosure geometry was changed. However, if near-nose pressure disturbance is of primary concern, this work shows that for $x/h < 1$, the fairing tends to produce the largest disturbance to the pressure field regardless of how the enclosure shape is altered.

For all geometries, regardless of their shape, the 1% threshold in the computed upstream pressure disturbance occurred at about 8-10 body heights upstream which agrees with previous student work⁷. The smallest upstream zone of disturbed pressure field was caused by the $w_e/h = 3.0$ enclosure of Case 6, and the largest by the 60° ramped-front enclosure of Case 7. Finally, the CFD showed that in general, the shape of the BLDS main unit housing has the most dramatic impact on upstream pressure field for $x/h < 6$. Beyond this point, changing the housing shape does not greatly influence how the upstream pressure field is disturbed by the excrescence.

5.2 Recommendations

This thesis demonstrated that most of the pressure disturbance upstream of the BLDS housings is inviscid. Therefore, it should be possible for a quicker estimate of the upstream pressure disturbance to be obtained using FLUENT in inviscid mode. For

inviscid flows, Ansys FLUENT solves the Euler equations¹⁹. Future CFD studies involving the BLDS housings should explore use of the inviscid model in FLUENT to capture the upstream pressure disturbance without using a turbulence model. This method would not allow for drag estimates, or visualization of viscous effects near the excrescence nose, but if only upstream pressure disturbance is desired, using the inviscid model would reduce computation time. In addition, while the 2-D inviscid solution was found to be a good estimate of the upstream pressure disturbance, the BLDS main unit housings are 3-D excrescences. Therefore, an inviscid analysis using an axisymmetric 3-D Rankine body¹¹ should be conducted. The 3-D CFD solutions can then be compared to a relevant inviscid solution to determine how well potential flow theory represents flow in the vicinity of a 3-D BLDS main unit.

Another inviscid phenomenon that warrants further study are the effects of chord length. The comparison of the inviscid solution to past student work³⁰ with 2-D Rankine bodies demonstrated that model chord length may impact the pressure field. Agreement between the measured and inviscid upstream pressure disturbance decreased for ovals of longer chord. The effect of chord was not studied with viscous CFD in this work, but it would be useful to conduct a detailed viscous analysis to evaluate how varying the chord of BLDS shapes changes the viscous effects present in the flow.

Finally, the fairing housing in this thesis was only modeled at half-scale, but the full-scale version of the fairing housing is intended to be placed on top of the existing BLDS electrical unit. A full-scale fairing housing would have a larger height, width, and

frontal area than any ramped-front enclosure housing presented in this work.

Therefore, future studies involving BLDS housing geometries should include the full-scale fairing instead of the half-scale version. Computed results for the spanwise pressure disturbance, upstream pressure disturbance, and pressure drag coefficient for a full-scale fairing will help inform future BLDS project work on the consequences and benefits of implementing a drop-on fairing.

REFERENCES

- [1] Westphal, R.V., Bleazard, M., Drake, A., Bender, A., Frame, D., Jordan, S.R. "A Compact, Self-Contained System for Boundary Layer Measurements in Flight." *AIAA Paper* 2006-3828.
- [2] Westphal, R.V., Frame, D., Jordan, S.R., Wanner, A., Thompson, B., Bender, A.M., Drake, A., "Design of a Third-Generation Boundary Layer Measurement System." *AIAA Paper* 2008-7332, <https://doi.org/10.2514/6.2008-7332>.
- [3] Akagi, Raymond M. "Ram Air-Turbine of Minimum Drag." *California Polytechnic State University*, Mar. 2021, <https://digitalcommons.calpoly.edu/theses/2261>. Accessed 10 May 2022.
- [4] Mejia, K.M., Ulk, C.R., Antunes, A.P., Cosin, R., Westphal, R.V., "Testing of an Autonomous Boundary Layer Data System Device in the Transonic Flight Regime." *AIAA Paper* 2018-4196, <https://doi.org/10.2514/6.2018-4196>.
- [5] Hoerner, S. *Fluid-Dynamic Drag: Theoretical, Experimental, and Statistical Information*. Hoerner Fluid Dynamics, 1965
- [6] R. Westphal, private communication, April 2022.
- [7] Sharma, N. R. and Westphal, R.V. "Surface Pressure Disturbance Upstream of the Boundary Layer Data System." Private Communication. *California Polytechnic State University San Luis Obispo*, 2018.
- [8] Mages, D. "BLDS Coefficient of Drag Determination via Wake Analysis." Private Communication. *California Polytechnic State University San Luis Obispo*, 2014.
- [9] Pritchard, P.J. and Mitchell, J.W. *Fox and McDonald's Introduction to Fluid Mechanics*. Wiley, 2015
- [10] ESDU, 2016. *An introduction to aircraft excrescence drag*. ESDU 90029c. The Royal Aeronautical Society.
- [11] Batchelor, G K. *An Introduction to Fluid Dynamics*. Cambridge University Press, 1967.
- [12] Bender, A.M., Westphal, R.V., Drake, A., "Application of the Boundary Layer Data System on a Laminar Flow Swept Wing Model in Flight." *AIAA Paper* 2010-4360, <https://doi.org/10.2514/6.2010-4360>.

- [13] Ngo, C.C., and Gramoll, K., *Fluids EBook: Incompressible and Inviscid Flow*, University of Oklahoma, http://ecourses.ou.edu/cgi-bin/ebook.cgi?doc&topic=fl&chap_sec=07.4&page=theory.
- [14] Liburdy, J. "Potential Flows." *Intermediate Fluid Mechanics*, Oregon State University, 16 Sept. 2021, <https://open.oregonstate.education/intermediate-fluid-mechanics/chapter/potential-flows/>.
- [15] Alfonsi, G. Reynolds-Averaged Navier-Stokes equations for turbulence modeling. *Applied Mechanics Reviews*, July 2009.
- [16] Mclean, J. D. *Understanding Aerodynamics: Arguing from the Real Physics*. Wiley, 2012.
- [17] Spalart, P. R. and Allmaras, S. R., "A One-Equation Turbulence Model for Aerodynamic Flows," *Recherche Aerospatiale*, No. 1, 1994, pp. 5-21.
- [18] Ansys® FLUENT, 2020 R1, ANSYS Inc.
- [19] Ansys® FLUENT, Release 12.0, Help System, User's Guide, ANSYS, Inc.
- [20] Ansys® ICEM CFD, 2020 R1, ANSYS Inc.
- [21] Sherry, M., Lo Jacono, D., Sheridan, J. "An Experimental Investigation of the Recirculation Zone Formed Downstream of a Forward Facing Step." *Journal of Wind Engineering and Industrial Aerodynamics*, vol. 98, no. 12, 8 Oct. 2010, pp. 888–894., <https://doi.org/10.1016/j.jweia.2010.09.003>.
- [22] White, F. M. *Viscous Fluid Flow*. McGraw-Hill, 2006.
- [23] Anderson, D.A., et al. *Computational Fluid Mechanics and Heat Transfer*. CRC Press, 2011.
- [24] Roy, C.J., Raju, A., and Hopkins, M.M., "Estimation of Discretization Errors Using the Method of Nearby Problems." *AIAA Journal*, vol. 45, no. 6, 2007, pp. 1232–1243., <https://doi.org/10.2514/1.24282>.
- [25] Celik, I. B., Ghia, U., Roache, P.J., Freitas, C.J., "Procedure for Estimation and Reporting of Uncertainty Due to Discretization in CFD Applications." *Journal of Fluids Engineering*, vol. 130, no. 7, 2008, p. 078001., <https://doi.org/10.1115/1.2960953>.

- [26] Ferrari, M. and Odaguil, F. "An Original and Consistent Method to Calculate Drag Increments Using CFD." AIAA Paper 2019-1905, <https://doi.org/10.2514/6.2019-1905>.
- [27] Rae, W. H., and Pope, A. "Wall Corrections for Two-Dimensional Testing." *Low-Speed Wind Tunnel Testing*, Wiley, New York, 1984, pp. 350–374.
- [28] Sproston, J. L. and Göksel, O.T. "The calibration of a surface static tube." *The Aeronautical Journal (1968)* 76 (1972): 101 - 103.
- [29] Devenport, William. *Ideal Flow Machine*, Virginia Polytechnic Institute and State University , <http://www.dept.aoe.vt.edu/~devenpor/aoe5104/ifm/ifminfo.html>.
- [30] Diep, A. "Zone of Influence: An Experimental Study." Private Communication. *California Polytechnic State University San Luis Obispo*, 2017.
- [31] NASA Langley Research Center, Turbulence Modeling Resource, "2D NACA 0012 Airfoil Validation Case," http://turbmodels.larc.nasa.gov/naca0012_val.html, October 10, 2011.

APPENDICES

Appendix A. Test Set-Up & BLDS Housing Shapes from Past Pressure Disturbance Experiment

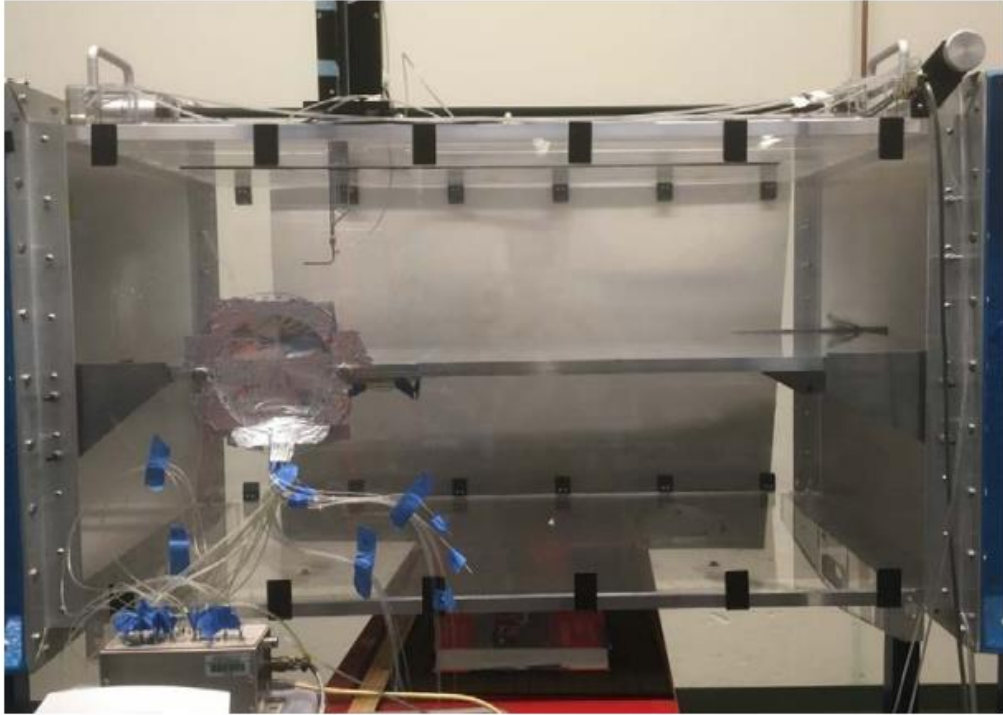





Figure A-1: Experimental Set-Up From Past Pressure Disturbance Experiment⁷.

Table A-1: Summary of Test Cases From Past Pressure Disturbance Experiment⁷.

Name	Dimensions $w \times l \times h$ (in)	Image
BLDS-PTDS	2.781 x 6.406 x 0.906	

<p>BLDS- Traverse</p>	<p>Housing dims same as BLDS- PTDS</p> <p>Stage Dims: 0.719 x 0.969 x 3.906</p>	
<p>BLDS- Fairing</p>	<p>2.297 x 4.969 x 0.625</p>	
<p>BLDS- Total Rake Array</p>	<p>0.234 x 2.469 x 2.250</p>	

<p>BLDS- Mini Satellite (with feet)</p>	<p>2.000 x 3.563 x 0.594</p>	
<p>BLDS- Mini Satellite (no feet)</p>	<p>2.000 x 3.563 x 0.484</p>	
<p>BLDS- Satellite (no feet)</p>	<p>2.750 x 4.141 x 0.547</p>	
<p>BLDS- Rake Short Housing</p>	<p>2.781 x 6.969 x 0.813</p>	

Appendix B. 2-D Experiment Raw Data for Test Cases 1 and 2

TEST CASE 1 (2-D TALL)			TEST CASE 2 (2-D SHORT)		
Floor Scale Measurement	Distance Upstream of Model Nose	Pressure Differential	Floor Scale Measurement	Distance Upstream of Model Nose	Pressure Differential
[in]	[in]	[VDC]	[in]	[in]	[VDC]
9.25	21.4	1.217	5	25.65	1.247
5.5	25.15	1.207	6	24.65	1.249
6	24.65	1.209	7	23.65	1.254
7	23.65	1.212	8	22.65	1.256
8	22.65	1.213	9	21.65	1.26
9	21.65	1.215	10	20.65	1.26
10	20.65	1.215	11	19.65	1.262
11	19.65	1.215	12	18.65	1.263
12	18.65	1.215	13	17.65	1.264
13	17.65	1.212	14	16.65	1.265
14	16.65	1.21	15	15.65	1.266
15	15.65	1.207	16	14.65	1.265
16	14.65	1.204	17	13.65	1.264
17	13.65	1.199	18	12.65	1.263
18	12.65	1.194	19	11.65	1.262
19	11.65	1.186	20	10.65	1.259
20	10.65	1.176	21	9.65	1.256
21	9.65	1.164	22	8.65	1.252
22	8.65	1.149	23	7.65	1.244
23	7.65	1.13	24	6.65	1.233
24	6.65	1.103	24.5	6.15	1.228
25	5.65	1.068	25	5.65	1.22
26	4.65	1.021	25.5	5.15	1.211
27	3.65	0.967	26	4.65	1.197
28	2.65	0.888	26.5	4.15	1.185
29	1.65	0.795	27	3.65	1.165
29.5	1.15	0.743	27.5	3.15	1.144
			28	2.65	1.113
			28.5	2.15	1.07
			29	1.65	1.017
			29.25	1.4	0.959
TEST CASE 1 (2-D TALL)			TEST CASE 2 (2-D SHORT)		
Wind-Off Tare	-0.011	VDC	Wind-Off Tare	-0.012	VDC
Reference Pressure	1.264	VDC	Reference Pressure	1.261	VDC
Model Nose Position	30.65	in	Model Nose Position	30.65	in
Excrescence Hieght	1.5	in	Excrescence Hieght	0.713	in
Ambient Temp.	69.82	°F	Ambient Temp.	69.81	°F
Ambient Pressure	14.657	psia	Ambient Pressure	14.61	psia
Test Date	1/26/2022		Test Date	2/16/2022	

Appendix C. Empty Tunnel Correction Raw Data

Experimental Constants (Measured)					
Wind-Off Tare (VDC)	-0.013	Ambient Temp.	69.82	°F	
Reference Static Pressure (VDC)	1.269	Ambient Pressure	14.657	psia	
Reference Static Pressure (inH2O)	3.846	Test Date	1/26/2022		
Model Nose Location from Inlet (in)	30.65				
Traverse Probe Distance from Floor (in)	0.28				
Experimental Data					
		Pressure Differentials			
Floor Scale Location [in]	Dist. Upstream of Nose [in]	VDC	inH2O	Cp	
9.25	21.4	1.267	3.84	0.00156	
5.5	25.15	1.251	3.792	0.01404	
6	24.65	1.254	3.801	0.01170	
7	23.65	1.258	3.813	0.00858	
8	22.65	1.261	3.822	0.00624	
9	21.65	1.264	3.831	0.00390	
10	20.65	1.267	3.84	0.00156	
11	19.65	1.269	3.846	0.00000	
12	18.65	1.273	3.858	-0.00312	
13	17.65	1.272	3.855	-0.00234	
14	16.65	1.275	3.864	-0.00468	
15	15.65	1.276	3.867	-0.00546	
16	14.65	1.278	3.873	-0.00702	
17	13.65	1.28	3.879	-0.00858	
18	12.65	1.283	3.888	-0.01092	
19	11.65	1.284	3.891	-0.01170	
20	10.65	1.284	3.891	-0.01170	
21	9.65	1.287	3.9	-0.01404	
22	8.65	1.289	3.906	-0.01560	
23	7.65	1.29	3.909	-0.01638	
24	6.65	1.291	3.912	-0.01716	
25	5.65	1.291	3.912	-0.01716	
26	4.65	1.293	3.918	-0.01872	
27	3.65	1.294	3.921	-0.01950	
28	2.65	1.295	3.924	-0.02028	
29	1.65	1.296	3.927	-0.02106	
30	0.65	1.296	3.927	-0.02106	
30.65	0	1.297	3.93	-0.02184	
32	-1.35	1.288	3.903	-0.01482	

Appendix D. 3-D Experiment Raw Data for Test Cases 3 and 4

TEST CASE 3 (3-D ENCLOSURE)			TEST CASE 4 (3-D FAIRING)		
Floor Scale Measurement	Distance Upstream of Model Nose	Pressure Differential	Floor Scale Measurement	Distance Upstream of Model Nose	Pressure Differential
[in]	[in]	[VDC]	[in]	[in]	[VDC]
25.25	25.25	1.246	5	25.65	1.256
24	24	1.251	6	24.65	1.259
22	22	1.257	7	23.65	1.263
20	20	1.263	8	22.65	1.266
18	18	1.264	9	21.65	1.269
16	16	1.27	10	20.65	1.27
14	14	1.273	11	19.65	1.274
12	12	1.275	12	18.65	1.275
11	11	1.277	13	17.65	1.276
10	10	1.276	14	16.65	1.276
9	9	1.276	15	15.65	1.28
8	8	1.274	16	14.65	1.283
7	7	1.271	17	13.65	1.284
6	6	1.266	18	12.65	1.285
5	5	1.256	19	11.65	1.286
4	4	1.24	20	10.65	1.286
3	3	1.208	21	9.65	1.288
2	2	1.138	22	8.65	1.289
1.1	1.1	0.997	23	7.65	1.288
			24	6.65	1.286
			25	5.65	1.284
			25.5	5.15	1.281
			26	4.65	1.278
			26.5	4.15	1.273
			27	3.65	1.268
			27.5	3.15	1.26
			28	2.65	1.245
			28.5	2.15	1.226
			29	1.65	1.197
			29.75	0.9	1.102
TEST CASE 3 (3-D ENCLOSURE)			TEST CASE 4 (3-D FAIRING)		
Wind-Off Tare	-0.013	VDC	Wind-Off Tare	-0.012	VDC
Reference Pressure	1.264	VDC	Reference Press	1.271	VDC
Model Nose Positio	30.65	in	Model Nose Pos	30.65	in
Excrescence Hieght	0.732	in	Excrescence Hie	0.684	in
Ambient Temp.	70.82	°F	Ambient Temp.	69.81	°F
Ambient Pressure	14.67	psia	Ambient Pressur	14.61	psia
Test Date	1/14/2022		Test Date	2/16/2022	

Appendix E. Boundary Layer Rake Experiment Raw Data

Wind-Off Tare	-0.015	VDC						
Free-Stream Velocity	39.6	m/s						
Air Viscosity	1.82E-05	N-s/m ²						
Air Density	1.1913	kg/m ³						
Ambient T	70.22	°F						
Ambient P	14.601	psia						
Test Date	3/9/2022							
Probe Label	Tube Height from test-section Floor [m]	Tube Height from test-section Floor [in]	Pressure Differential [VDC]	Pressure Differential [inH2O]	Pressure Differential [Pa]	Velocity [m/s]	u/U	
1	0.0004064	0.016	0.338	1.059	263.785251	21.04413	0.531417	
2	0.0007874	0.031	0.432	1.341	334.028349	23.68085	0.598001	
3	0.0014986	0.059	0.509	1.572	391.567908	25.63948	0.647462	
4	0.0028702	0.113	0.616	1.893	471.525477	28.13573	0.710498	
14	0.0051816	0.204	0.729	2.232	555.966648	30.55132	0.771498	
5	0.0068326	0.269	0.806	2.463	613.506207	32.09336	0.810438	
15	0.008255	0.325	0.875	2.67	665.06763	33.41478	0.843807	
6	0.0095758	0.377	0.925	2.82	702.43098	34.34057	0.867186	
16	0.0107188	0.422	0.951	2.898	721.859922	34.81225	0.879097	
7	0.0121158	0.477	1.011	3.078	766.695942	35.87709	0.905987	
8	0.0143764	0.566	1.087	3.306	823.488234	37.18214	0.938943	
9	0.0182626	0.719	1.199	3.642	907.182138	39.0259	0.985502	
10	0.024638	0.97	1.249	3.792	944.545488	39.82145	1.005592	
11	0.0313436	1.234	1.249	3.792	944.545488	39.82145	1.005592	
12	0.0378206	1.489	1.251	3.798	946.040022	39.85294	1.006387	
13	0.0503936	1.984	1.25	3.795	945.292755	39.8372	1.00599	

Appendix F. MATLAB Scripts for all Inviscid Analyses

Comparing Rankine Oval/Cylinder to Past Experimental Data

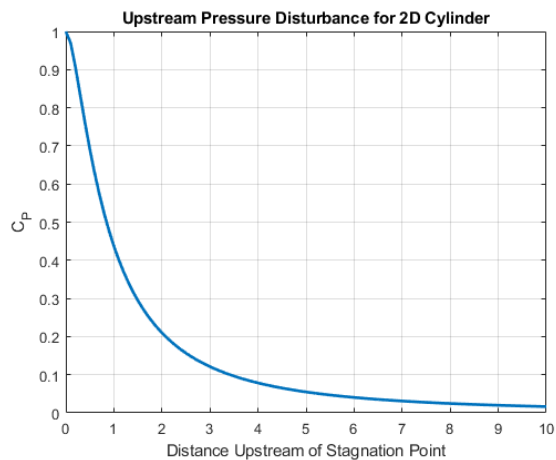
Michelle Leclere Appendix F

The following script is used to compare the potential flow solution for upstream pressure disturbance of Rankine bodies and a circular cylinder to the measurements from a 2014 study done by Cal Poly student Andy Diep. The Rankine Oval potential flow is interpreted as a solid body in crossflow.

Circular Cylinder.....	143
Rankine Ovals.....	143

Circular Cylinder

```
x = (1:0.1:100);
Cp_cyl = (1./(x.^2)).*(2-(1./(x.^2)));
s_cyl = (x-1);
advplot(s_cyl, Cp_cyl, '-', 2, 'Distance Upstream of Stagnation Point', ...
        'C_P', 'Upstream Pressure Disturbance for 2D Cylinder', 1)
xlim([0 10]);
ylim([0 1]);
```



Rankine Ovals

```
RATIO = [];
a_vals = [1.78]; % [1.78,2.81,3.55]; for 3, 6, 9 respectively
for a = a_vals
    Cp_ovl = (1./((x.^2)-a^2)).*(2-(1./((x.^2)-a^2)));
    L = sqrt(1+(a^2)); % location of the upstream stagnation point [in]
    fcn_2 = @(H) (((H^2)-(a^2))/(2*a))*tan(2*a*H) - H; % implicit function for oval
    half-body width
    if a >=1
        H_guess = 0.9315*(a^(-0.724));
    elseif a>0 && a<1
        H_guess = 1;
    end
end
```

```

H = fzero(fcn_2, H_guess); % half body width
RATIO = [RATIO L/H] % chord to half width ratio
s_ovl = (x-L)./H; % normalized upstream distance from the stagnation point
advplot(s_ovl, Cp_ovl, '-', 2, 'x-x_s_t_a_g/b', 'Cp',...
    'Upstream Cp for 2D Potential Flows', 1)
hold on
end
xlim([0.03 35]);
ylim([0 0.08]);
hold on

% The following sets of data are from the 2014 study done by Andy Diep

s_3 = [3.442622951 3.87295082 4.87704918 5.833333333 6.789617486 7.745901639...
    8.702185792 9.658469945 10.6147541 11.52322404 12.5273224 13.48360656,...
    14.48770492 15.44398907 16.44808743 17.30874317 18.26502732 19.22131148...
    20.22540984 21.18169399 22.18579235 22.71174863 22.99863388 24.14617486...
    25.05464481 25.96311475 27.25409836 27.97131148 28.78415301 29.78825137...
    30.69672131 31.36612022 31.74863388];

s_6 = [2.821038251 3.346994536 4.351092896 5.355191257 6.359289617 7.363387978...
    8.319672131 9.323770492 10.28005464 11.33196721 12.33606557 13.29234973...
    14.3442623 15.30054645 16.35245902 17.35655738 18.26502732 19.3647541...
    20.32103825 21.2773224 22.32923497 22.85519126 23.33333333 24.28961749...
    25.38934426 26.20218579 27.34972678 28.25819672 28.87978142 29.3579235...
    30.31420765 31.12704918 32.27459016];

s_9 = [4.590163934 5.068306011 6.072404372 7.076502732 8.080601093 9.084699454...
    10.08879781 11.09289617 12.04918033 13.1010929 14.05737705 15.06147541...
    16.06557377 17.02185792 18.1215847 19.03005464 20.08196721 21.13387978...
    22.09016393 23.04644809 23.57240437 24.05054645 25.05464481 26.10655738...
    27.06284153 28.01912568 28.78415301 29.07103825 30.0273224 30.98360656...
    31.31830601 31.93989071 32.41803279 33.03961749];

s_cyl = [2.749348775 2.849247444 3.092587975 3.336485562 3.580197463 3.77609541...
    4.020178682 4.263147843 4.554859383 5.084526582 5.517637447 6.046004849...
    6.479301399 7.294181155 8.155946438 9.353337825 10.40728735 12.03463295...
    12.99184046 14.71425691 16.38811667 17.63109379 19.06588378 20.45285982...
    22.55611674 21.50402406 24.51667454 25.71165202 26.81174433];

Cp_3 = [0.047174842 0.037838234 0.024924412 0.017924773 0.012481555 0.009839893...
    0.007509515 0.005490421 0.004093896 0.003475367 0.003168548 0.002238949...
    0.001465204 0.00100253 0.001162637 0.001166465 0.000548149 -0.000381451...
    0.000401225 0.000405477 0.000409942 0.000256639 0.000102273 0.000263018...
    0.000267058 0.000115456 -0.000345729 -0.00034254 -2.76413E-05 -2.31762E-05...
    -1.91363E-05 -1.61596E-05 0.000296825];

Cp_6 = [0.068339393 0.05666858 0.036439582 0.024459612 0.016837618 0.011861538...
    0.00875295 0.006111501 0.004248049 0.003318875 0.001922562 0.000992962 0.000530714...
    0.000534966 -8.2924E-05 -7.84589E-05 -0.000696987 -0.001159023 9.03659E-05...
    -0.000372308 -0.00036763 -5.40069E-05 -5.18807E-05 0.000263656 -4.27378E-05...
    -3.91231E-05 -3.40201E-05 0.000125662 0.000128426 0.000130552 0.000601731...
    0.000294061 0.000454806];

```

```

Cp_9 = [0.076596288 0.064302694 0.04282856 0.029136527 0.021670175 0.015760243...
0.0120293 0.008920924 0.007057473 0.005038804 0.004109205 0.003179818 0.002406073...
0.001787757 0.001481363 0.001174119 0.001023155 0.001027833 0.001032085 0.00119198...
0.000727393 0.000885161 0.00120091 0.001205588 0.000275988 0.000747167 0.000128001...
0.000907487 0.000911739 0.000604708 0.000606196 0.00060896 0.000455444 0.000302566];

Cp_cyl = [0.050187012 0.046614639 0.043042904 0.039005151 0.035122738 0.031240112...
0.027047021 0.023785963 0.019748423 0.016643978 0.014315803 0.01229873 0.009815217...
0.008110095 0.007181881 0.005478458 0.003774398 0.002383562 0.001611111
0.000686717...
0.000383467 0.000544323 0.000240011 -6.45124E-05 0.000410842 0.000561512
0.000264204...
0.000580187 0.00027439];

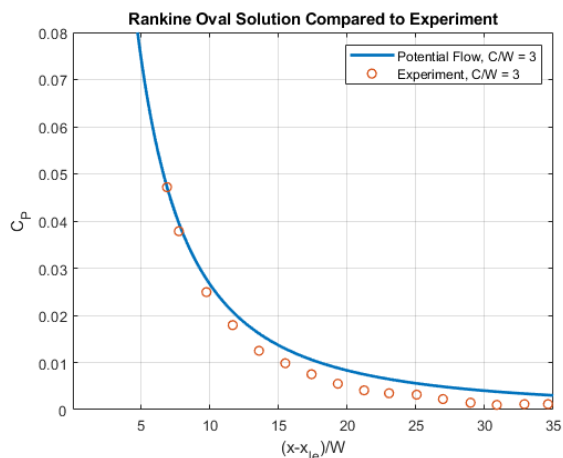
advplot((s_3./0.5), Cp_3, 'o', 1, '(x-x_l_e)/W', 'C_P',...
'Rankine Oval Solution Compared to Experiment', 1)
%% % hold on
% advplot((s_6./0.5), Cp_6, 'o', 1, '(x-x_l_e)/W', 'C_P',...
% 'Rankine Oval Solution Compared to Experiment', 1)
%% % hold on
% advplot((s_9./0.5), Cp_9, 'o', 1, '(x-x_l_e)/W', 'C_P',...
% 'Rankine Oval Solution Compared to Experiment', 1)
%% hold on
% advplot((s_cyl./0.5), Cp_cyl, 'o', 1, '(x-x_l_e)/W', 'C_P',...
% 'Circular Cylinder Solution Compared to Experiment', 1)

legend('Potential Flow, C/W = 3', 'Experiment, C/W = 3')

```

RATIO =

3.0113



[Published with MATLAB® R2021b](#)

Comparing Rankine Oval to 2-D Measurements from Chapter 2

Michelle Leclere Appendix F

The following script is used to compare the potential flow solution for upstream pressure disturbance of Rankine bodies in uniform flow to the 2-D wind tunnel measurements presented in Chapter 2. The Rankine Oval potential flow is interpreted as that of a "bump" on a solid, impermeable surface.

Rankine Oval Upstream Pressure Disturbance 146

Rankine Oval Upstream Pressure Disturbance

```
x = (1:0.1:100);
RATIO = [];
a_vals = [2.49];%[1.445] for TALL, [2.49] for SMALL
for a = a_vals
    U = 10;
    m = (U*pi)/a;
    Cp_ov1 = (1./((x.^2)-a^2)).*(2-(1./((x.^2)-a^2)));
    L = sqrt(1+(a^2)); % location of the upstream stagnation point
    fcn_2 = @(H) (((H^2)-(a^2))/(2*a))*tan((2*a*H)) - H; % implicit function for half-
body width
    if a >=1
        H_guess = 0.9315*(a^(-0.724));
    elseif a>0 && a<1
        H_guess = 1;
    end
    H = fzero(fcn_2, H_guess)
    RATIO = [RATIO L/H] % half chord to half width ratio
    s_ov1 = (x-L)./H; % normalized upstream distance from the stagnation point of the
oval normalized by half body width
    advplot(s_ov1, Cp_ov1, '-', 2,'x-x_s_t_a_g/b', 'Cp',...
        'Upstream Cp for 2D Potential Flows', 1)
    hold on
end
xlim([0.03 18]);
ylim([-0.1 0.8]);
hold on

% Experimental Data from Test Case 1
s_exp = [14.27 16.77 16.43 15.77 15.10 14.43 13.77 13.10 12.43 11.77 11.10...
10.43 9.77 9.10 8.43 7.77 7.10 6.43 5.77 5.10 4.43 3.77 3.10 2.43 1.77 1.10 0.77];

Cp_exp = [0.007318065 0.002908591 0.00363448 0.004333297 0.005866288 ...
0.006592177 0.00893227 0.010492333 0.013612457 0.015253734 0.019208032...
0.022409371 0.026390741 0.031986316 0.038361922 0.045598773 0.053669798...
0.065695122 0.079361722 0.0954767 0.118048499 0.146297087 0.185790967...
0.230154533 0.294695662 0.370536226 0.413608217];

% Experimental Data from Test Case 2
s_exp_short = [35.97 34.57 33.17 31.77 30.36 28.96 27.56 26.16 24.75 23.35...
21.95 20.55 19.14 17.74 16.34 14.94 13.53 12.13 10.73 9.33 8.63 7.92 ...
```

```

7.22 6.52 5.82 5.12 4.42 3.72 3.02 2.31 1.96];

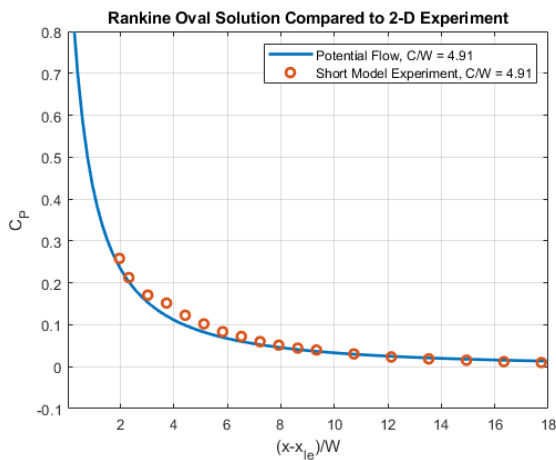
Cp_exp_short = [0.002756641 0.002286116 0.000461631 0.000879327 -0.000457627...
0.001252473 0.001278017 0.001953032 0.002601787 0.002929649 0.003620862...
0.005695335 0.007869343 0.009991092 0.012044898 0.015382142 0.018764281...
0.023216357 0.030463222 0.039845395 0.044396793 0.051388736 0.059796456...
0.072133408 0.083474309 0.102104037 0.122771008 0.151882226 0.170710104...
0.212734055 0.25829572];

% advplot(s_exp, Cp_exp, 'o', 2, '(x-x_1_e)/W', 'C_P',...
% 'Rankine Oval Solution Compared to 2-D Experiment', 1)
advplot(s_exp_short, Cp_exp_short, 'o', 2, '(x-x_1_e)/W', 'C_P',...
'Rankine Oval Solution Compared to 2-D Experiment', 1)
legend('Potential Flow, C/W = 4.91', 'Short Model Experiment, C/W = 4.91')

```

RATIO =

4.9289



[Published with MATLAB® R2021b](#)

Comparing Rankine Oval to 2-D CFD from Chapter 3

Michelle Leclere Appendix F

The following script is used to compare the potential flow solution for upstream pressure disturbance of Rankine bodies in uniform flow to the 2-D CFD solutions presented in Chapter 3. The Rankine Oval potential flow is interpreted as that of a "bump" on a solid, impermeable surface.

Rankine Oval and Free-Air FLUENT 2-D Results..... 147

Rankine Oval and Free-Air FLUENT 2-D Results

```

x = (1:0.1:100);
RATIO = [];
a_vals = [1.445]; % [1.445] for TALL, [2.49] for SHORT

```

```

for a = a_vals
    U = 10;
    m = (U*pi)/a;
    Cp_ovl = (1./((x.^2)-a^2)).*(2-(1./((x.^2)-a^2)));
    L = sqrt(1+(a^2)); % location of the upstream stagnation point
    fcn_2 = @(H) (((H^2)-(a^2))/(2*a))*tan(2*a*H) - H; % implicit function for half-
body width
    if a >=1
        H_guess = 0.9315*(a^(-0.724));
    elseif a>0 && a<1
        H_guess = 1;
    end
    H = fzero(fcn_2, H_guess);
    RATIO = [RATIO L/H] % chord to half width ratio
    s_ovl = (x-L)./H; % normalized upstream distance from the stagnation point
    advplot(s_ovl, Cp_ovl, '-', 2,'x-x_s_t_a_g/b', 'Cp',...
        'Upstream Cp for 2D Potential Flows', 1)
    hold on
end
xlim([0.03 18]);
ylim([-0.1 0.8]);
hold on

% CFD Solution for 2-D Case 3
s_FL_tall = [32 31.59493701 31.18987402 30.78481102 30.37974803 29.97468241...
29.56961942 29.16456693 28.75950131 28.3544357 27.94937008 27.54430446...
27.13923885 26.73417323 26.32910761 25.92404199 25.51897638 25.11393701...
24.70887139 24.30380577 23.89874016 23.49367454 23.08860892 22.68354331...
22.27847769 21.87341207 21.46834646 21.06328084 20.65821522 20.25317585...
19.84811024 19.44304462 19.037979 18.63291339 18.22784777 17.82278215...
17.41771654 17.01265092 16.6075853 16.20251969 15.79748031 15.3924147...
14.98734908 14.58228346 14.17721785 13.77215223 13.36708661 12.962021...
12.55695538 12.15188976 11.74682415 11.34178478 10.93671916 10.53165354...
10.12658793 9.72152231 9.316456693 8.911391076 8.506325459 8.101259843...
7.696194226 7.291128609 6.886062992 6.481023622 6.075958005 5.670866142...
5.265879265 4.860629921 4.455643045 4.050656168 3.645669291 3.240419948...
2.835433071 2.430446194 2.02519685 1.620209974 1.215223097 0.81023622...
0.404986877 0];
Cp_FL_tall = [0.00606196 0 -0.00626126 -0.00513499 -0.00549102 -0.00560586 -0.0056943...
-0.00572139 -0.00571013 -0.00565851 -0.00557312 -0.00545694 -0.00531201 -
0.00513915...
-0.00493934 -0.00471258 -0.00445939 -0.00418007 -0.00387415 -0.00354142 -
0.00318133...
-0.00279323 -0.00237639 -0.00192985 -0.00145259 -0.000943436 -0.000401056
0.000176016...
0.000789383 0.00144089 0.00213248 0.00286628 0.00364473 0.00447035 0.00534605
0.00627495...
0.00726041 0.00830625 0.0094166 0.010596 0.0118494 0.0131824 0.0146012 0.0161123...
0.0177237 0.0194434 0.0212807 0.0232463 0.0253517 0.0276103 0.0300367 0.032648
0.0354631...
0.0385039 0.0417953 0.0453659 0.0492487 0.0534823 0.0581111 0.0631878 0.0687738
0.0749431...
0.0817807 0.0893967 0.0979063 0.107491 0.118278 0.130639 0.14456 0.161019 0.179261
0.20199...

```

```

0.226212 0.258416 0.290402 0.333804 0.374304 0.411051 0.445969 0.45155];

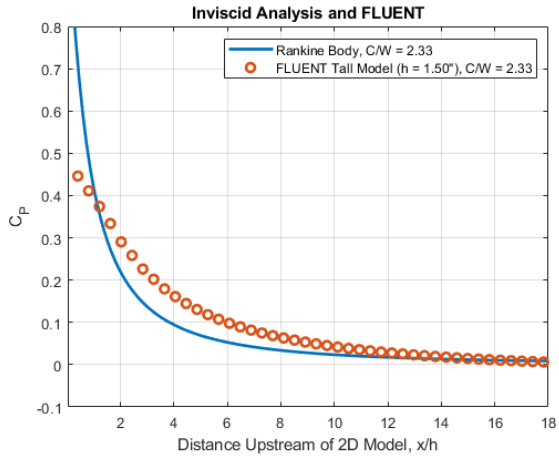
% CFD Solution for 2-D Case 4
s_FL_short = [67.6056338 66.74986692 65.89410003 65.03833315 64.18256626 63.32679383...
62.47102695 61.61528224 60.75950981 59.90373738 59.04796496 58.19219253 57.3364201...
56.48064767 55.62487524 54.76910281 53.91333038 53.0576134 52.20184097 51.34606854...
50.49029611 49.63452368 48.77875125 47.92297882 47.06720639 46.21143396
45.35566153...
44.4998891 43.64411667 42.78839969 41.93262726 41.07685483 40.2210824 39.36530997...
38.50953754 37.65376511 36.79799268 35.94222025 35.08644782 34.23067539
33.37495841...
32.51918598 31.66341355 30.80764112 29.95186869 29.09609626 28.24032383 27.3845514...
26.52877897 25.67300654 24.81723411 23.96151713 23.1057447 22.24997227 21.39419984...
20.53842741 19.68265499 18.82688256 17.97111013 17.1153377 16.25956527 15.40379284...
14.54802041 13.69230343 12.836531 11.98070312 11.12509704 10.26893645 9.413330376...
8.557724299 7.702118221 6.845957636 5.990351558 5.134745481 4.278584895
3.422978818...
2.56737274 1.711766663 0.855606077 0];
Cp_FL_short = [0.0137754 0.00660293 0.00162795 0.0016664 0.00173662 0.00140873
0.00117196...
0.000979799 0.00082273 0.000689152 0.000577741 0.000485802 0.000410846 0.000351536...
0.000306556 0.000274877 0.000255919 0.00024893 0.000253226 0.000268973 0.00029623...
0.000334509 0.000383658 0.000443815 0.000515162 0.000597925 0.00069239 0.000798836...
0.00091763 0.00104927 0.00119433 0.00135346 0.00152736 0.00171685 0.00192275
0.00214594...
0.00238762 0.00264906 0.00293163 0.00323685 0.00356641 0.00392216 0.00430628
0.00472124...
0.00516973 0.00565483 0.00617996 0.00674903 0.00736647 0.00803732 0.00876739
0.00956318...
0.0104327 0.0113845 0.0124288 0.0135777 0.0148458 0.0162493 0.0178083 0.0195466
0.0214929...
0.0236823 0.0261576 0.0289722 0.032192 0.0359031 0.0402081 0.045261 0.0512119
0.0583949...
0.0669477 0.0777895 0.0906976 0.108336 0.129394 0.161503 0.197452 0.258461 0.317057
0.328553];

advplot(s_FL_tall, Cp_FL_tall, 'o', 2, 'Distance Upstream of 2D Model, x/h', 'C_P',...
'Inviscid Analysis and FLUENT', 1)
% advplot(s_FL_short, Cp_FL_short, 'o', 2, 'Distance Upstream of 2D Model, x/h', 'C_P',...
% 'Inviscid Analysis and FLUENT', 1)
legend('Rankine Body, C/W = 2.33', 'FLUENT Tall Model (h = 1.50)', 'C/W = 2.33')

```

RATIO =

2.3301



[Published with MATLAB® R2021b](#)

Appendix G. 2-D Geometry Replay Script

```
# Replay script for 2D model to compare with 2D wind tunnel experiments
#
# define parameters (all lengths are in inches)
#
set Lx 90
set Ly 24
set BLDSy 0.71
set BLDSx 3.5
set LEx 30.65
#
# define points
#
ic_geo_new_family PNT
ic_point {} PNT pnt.00 (-$Lx/16),0,0
ic_point {} PNT pnt.01 0,0,0
ic_point {} PNT pnt.02 $LEx,0,0
ic_point {} PNT pnt.03 ($LEx+$BLDSx),0,0
ic_point {} PNT pnt.04 $Lx,0,0
ic_point {} PNT pnt.05 ($LEx+$BLDSy),$BLDSy,0
ic_point {} PNT pnt.06 ($LEx+$BLDSx),$BLDSy,0
ic_point {} PNT pnt.07 (-$Lx/16),(4*$BLDSy),0
ic_point {} PNT pnt.08 0,(4*$BLDSy),0
ic_point {} PNT pnt.09 $Lx,(4*$BLDSy),0
ic_point {} PNT pnt.10 (-$Lx/16),$Ly,0
ic_point {} PNT pnt.11 0,$Ly,0
ic_point {} PNT pnt.12 $Lx,$Ly,0
#
# define curves with boundary names
#
ic_geo_new_family INLET
ic_curve point INLET crv.00 {pnt.00 pnt.07}
ic_curve point INLET crv.01 {pnt.07 pnt.10}
#
ic_geo_new_family OUTLET
ic_curve point OUTLET crv.02 {pnt.04 pnt.09}
ic_curve point OUTLET crv.03 {pnt.09 pnt.12}
#
ic_geo_new_family SYMMETRY_TOP
ic_curve point SYMMETRY_TOP crv.04 {pnt.10 pnt.11}
ic_curve point SYMMETRY_TOP crv.05 {pnt.11 pnt.12}
#
ic_geo_new_family WALL_UP
ic_curve point WALL_UP crv.06 {pnt.01 pnt.02}
#
ic_geo_new_family WALL_DWN
ic_curve point WALL_DWN crv.07 {pnt.03 pnt.04}
#
ic_geo_new_family SYMMETRY
ic_curve point SYMMETRY crv.08 {pnt.00 pnt.01}
#
ic_geo_new_family INTERIOR
ic_curve point INTERIOR crv.09 {pnt.07 pnt.08}
ic_curve point INTERIOR crv.10 {pnt.01 pnt.08}
ic_curve point INTERIOR crv.11 {pnt.08 pnt.11}
ic_curve point INTERIOR crv.12 {pnt.08 pnt.09}
#
```

```

ic_geo_new_family BLDS
ic_curve point BLDS crv.13 {pnt.02 pnt.05}
ic_curve point BLDS crv.14 {pnt.05 pnt.06}
ic_curve point BLDS crv.15 {pnt.06 pnt.03}
ic_curve point BLDS crv.16 {pnt.02 pnt.03}
#
# Create Blocking
#
ic_geo_new_family FLUID
ic_boco_set_part_color FLUID
ic_hex_unload_blocking
ic_hex_initialize_mesh 2d new_numbering new_blocking FLUID
ic_hex_unblank_blocks
ic_hex_multi_grid_level 0
ic_hex_projection_limit 0
ic_hex_default_bunching_law default 2.0
ic_hex_floating_grid off
ic_hex_transfinite_degree 1
ic_hex_unstruct_face_type one_tri
ic_hex_set_unstruct_face_method uniform_quad
ic_hex_set_n_tetra_smoothing_steps 20
ic_hex_error_messages off_minor
ic_hex_unstruct_face_type
ic_hex_set_unstruct_face_method
#
# Split Block
#
ic_hex_split_grid 11 13 pnt.07 m PNT INLET OUTLET SYMMETRY_TOP WALL_UP WALL_DWN SYMMETRY
INTERIOR BLDS FLUID VORFN
ic_hex_split_grid 11 33 pnt.05 m PNT INLET OUTLET SYMMETRY_TOP WALL_UP WALL_DWN SYMMETRY
INTERIOR BLDS FLUID VORFN
ic_hex_split_grid 11 19 pnt.01 m PNT INLET OUTLET SYMMETRY_TOP WALL_UP WALL_DWN SYMMETRY
INTERIOR BLDS FLUID VORFN
ic_hex_split_grid 41 19 pnt.02 m PNT INLET OUTLET SYMMETRY_TOP WALL_UP WALL_DWN SYMMETRY
INTERIOR BLDS FLUID VORFN
ic_hex_split_grid 47 19 pnt.03 m PNT INLET OUTLET SYMMETRY_TOP WALL_UP WALL_DWN SYMMETRY
INTERIOR BLDS FLUID VORFN
#
# Associate points
#
ic_hex_move_node 11 pnt.00
ic_hex_move_node 41 pnt.01
ic_hex_move_node 33 pnt.07
ic_hex_move_node 43 pnt.08
ic_hex_move_node 44 pnt.11
ic_hex_move_node 13 pnt.10
ic_hex_move_node 21 pnt.12
ic_hex_move_node 34 pnt.09
ic_hex_move_node 19 pnt.04
ic_hex_move_node 53 pnt.03
ic_hex_move_node 54 pnt.06
ic_hex_move_node 47 pnt.02
ic_hex_move_node 48 pnt.05
#
# Associate Curves
#
ic_hex_find_comp_curve crv.01
ic_hex_set_edge_projection 33 13 0 1 crv.01

```

```

ic_hex_find_comp_curve crv.11
ic_hex_set_edge_projection 43 44 0 1 crv.11
ic_hex_find_comp_curve crv.04
ic_hex_set_edge_projection 13 44 0 1 crv.04
ic_hex_find_comp_curve crv.09
ic_hex_set_edge_projection 33 43 0 1 crv.09
ic_hex_find_comp_curve crv.00
ic_hex_set_edge_projection 37 33 0 1 crv.00
ic_hex_find_comp_curve crv.00
ic_hex_set_edge_projection 11 37 0 1 crv.00
ic_hex_find_comp_curve crv.10
ic_hex_set_edge_projection 42 43 0 1 crv.10
ic_hex_find_comp_curve crv.10
ic_hex_set_edge_projection 41 42 0 1 crv.10
ic_hex_find_comp_curve crv.08
ic_hex_set_edge_projection 11 41 0 1 crv.08
ic_hex_find_comp_curve crv.06
ic_hex_set_edge_projection 41 47 0 1 crv.06
ic_hex_find_comp_curve crv.12
ic_hex_set_edge_projection 43 49 0 1 crv.12
ic_hex_find_comp_curve crv.05
ic_hex_set_edge_projection 44 50 0 1 crv.05
ic_hex_find_comp_curve crv.05
ic_hex_set_edge_projection 50 56 0 1 crv.05
ic_hex_find_comp_curve crv.05
ic_hex_set_edge_projection 56 21 0 1 crv.05
ic_hex_find_comp_curve crv.03
ic_hex_set_edge_projection 34 21 0 1 crv.03
ic_hex_find_comp_curve crv.02
ic_hex_set_edge_projection 38 34 0 1 crv.02
ic_hex_find_comp_curve crv.02
ic_hex_set_edge_projection 19 38 0 1 crv.02
ic_hex_find_comp_curve crv.07
ic_hex_set_edge_projection 53 19 0 1 crv.07
ic_hex_find_comp_curve crv.16
ic_hex_set_edge_projection 47 53 0 1 crv.16
ic_hex_find_comp_curve crv.13
ic_hex_set_edge_projection 47 48 0 1 crv.13
ic_hex_find_comp_curve crv.15
ic_hex_set_edge_projection 53 54 0 1 crv.15
ic_hex_find_comp_curve crv.14
ic_hex_set_edge_projection 48 54 0 1 crv.14
ic_hex_find_comp_curve crv.12
ic_hex_set_edge_projection 49 55 0 1 crv.12
ic_hex_find_comp_curve crv.12
ic_hex_set_edge_projection 55 34 0 1 crv.12
#
# Delete BLOCK and CURVE
#
ic_hex_mark_blocks unmark
ic_hex_mark_blocks superbloc 21
ic_hex_change_element_id VORFN
ic_geo_incident curve crv.16
ic_delete_geometry curve names crv.16 0 1
ic_set_dormant_pickable curve 0 {}

```

Appendix H. Discretization Error Calculations for 2-D and 3-D Meshes

The following discretization error calculations were done per the guidelines in the Journal of Fluids Engineering Editorial Policy Statement on the Control of Numerical Accuracy²⁵. The parameter of interest, φ , in each calculation is the computed surface pressure coefficient, C_p , collected from the CFD solution at the surface location indicated. Richardson extrapolation was used to compute the extrapolated values of C_p denoted as φ_{ext}^{21} at each location.

Table H-1: Discretization Error Estimation for 2-D Tall Mesh

	Upstream Location Relative to Excrescence Nose			Averages	Maximum Discretization Error
	17 Inches Upstream	30 Inches Upstream	0 Inches Upstream		
N_1, N_2, N_3	15978, 5840, 3880	15978, 5840, 3880	15978, 5840, 3880	-	-
r_{21}	2.736	2.736	2.736	-	-
r_{32}	1.505	1.505	1.505	-	-
φ_1	0.032391	0.02652	0.4853	-	-
φ_2	0.031901	0.02552	0.4691	-	-
φ_3	0.031181	0.02419	0.4529	-	-
φ_{ext}^{21}	0.032465	0.02671	0.49	-	-
$\varphi_{ext}^{21} - \varphi_1$	0.00007438	0.0001848	0.005500	-	0.005
ρ	1.938	1.784	1.338	1.6869	-
e_a^{21}	1.512	3.771	3.339	2.874	-
e_{ext}^{21}	0.2291	0.6919	1.120	0.6805	-
GCI_{fine}^{21}	0.2870	0.871	1.416	0.858	-

Table H-2: Discretization Error Estimation for 3-D RFE Mesh.

	Upstream Location Relative to Excrescence Nose			Averages	Maximum Discretization Error
	16 Inches Upstream	32 Inches Upstream	0 Inches Upstream		
N_1, N_2, N_3	360622, 120464, 32952	360622, 120464, 32952	360622, 120464, 32952	-	-
r_{21}	2.994	2.994	2.994	-	-
r_{32}	3.656	3.656	3.656	-	-
φ_1	0.003844	0.01894	0.1776	-	-
φ_2	0.003770	0.01832	0.1716	-	-
φ_3	0.003338	0.01403	0.1961	-	-
φ_{ext}^{21}	0.003867	0.01909	0.18	-	-
$\varphi_{ext}^{21} - \varphi_1$	0.00002335	0.0001561	0.002462	-	0.002
ρ	1.283	1.424	1.113	1.2734	-
e_a^{21}	1.932	3.236	3.372	2.846	-
e_{ext}^{21}	0.6038	0.8176	1.368	0.9297	-
GCI_{fine}^{21}	0.7593	1.030	1.733	1.2	-

Table H-3: Discretization Error Estimation for 3-D HSF Mesh.

	Upstream Location Relative to Excrescence Nose			Averages	Maximum Discretization Error
	21 Inches Upstream	34 Inches Upstream	4 Inches Upstream		
N_1, N_2, N_3	963000, 547233, 179338	963000, 547233, 179338	963000, 547233, 179338	-	-
r_{21}	1.760	1.760	1.760	-	-
r_{32}	3.051	3.051	3.051	-	-
φ_1	0.006652	0.00368	0.0305	-	-
φ_2	0.006644	0.00374	0.0303	-	-
φ_3	0.006611	0.00430	0.0296	-	-
φ_{ext}^{21}	0.006665	0.00365	0.03	-	-
$\varphi_{ext}^{21} - \varphi_1$	0.00001350	0.0000330	0.000430	-	0.0004
ρ	0.850	1.772	0.704	1.1087	-
e_a^{21}	0.121	1.547	0.656	0.775	-
e_{ext}^{21}	0.2026	0.9057	1.389	0.8326	-
GCI_{fine}^{21}	0.2537	1.122	1.761	1.046	-

Appendix I. 3-D RFE-A Mesh, Height, and Width Independence Study

Table I-1: 3-D Ramped-Front Enclosure Mesh Independence Study Case Identifiers.

Mesh	Grid Points	Reference Dynamic Pressure [Pa] q_{ref}
RFE-M-1	32,952	976.8
RFE-M-2	120,464	976.8
RFE-M-3	360,622	976.9
RFE-M-4	579,483	977.1

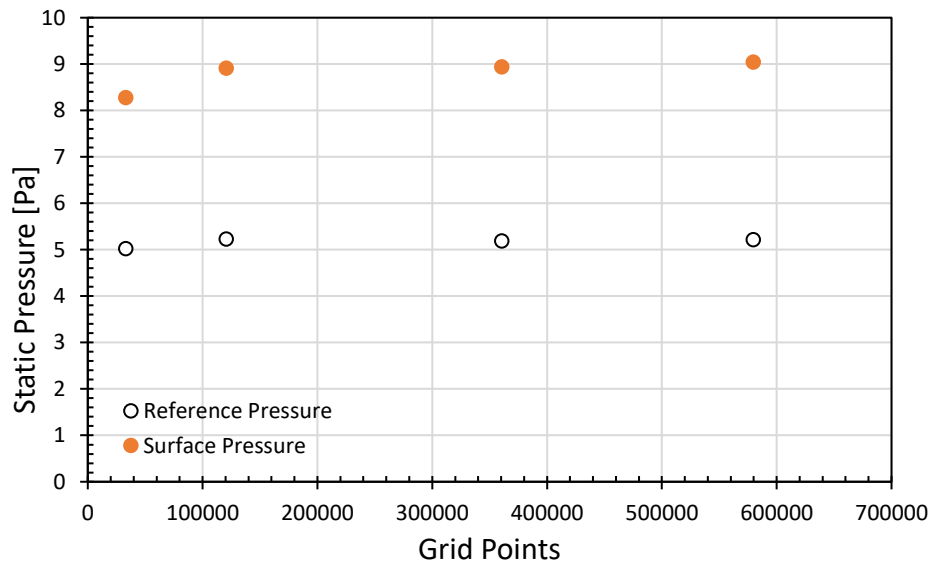


Figure I-1: 3-D Ramped-Front Enclosure Mesh Independence Study.

Mesh independence was achieved with about 600,000 grid points on mesh RFE-M-4 as the surface and reference static pressures changed by 1.2% and 0.58% between RFE-M-3 and RFE-M-4, respectively. The domain geometry, blocking and mesh patterns were recorded and rearranged in a working replay script that was used to alter the height and width of the domain to achieve the desired free-air conditions. The edge parameters from mesh RFE-M-4 were scaled with each change in height and width to maintain the mesh pattern.

Table I-2: 3-D RFE Height Independence Study Case Identifiers

Mesh	Domain Width [in] w_D	Domain Height [in] h_D	Reference Dynamic Pressure [Pa] q_{ref}
RFE-H-1	24	24	977.1
RFE-H-2	24	60	977.7
RFE-H-3	24	84	977.5
RFE-H-4	24	108	977.5

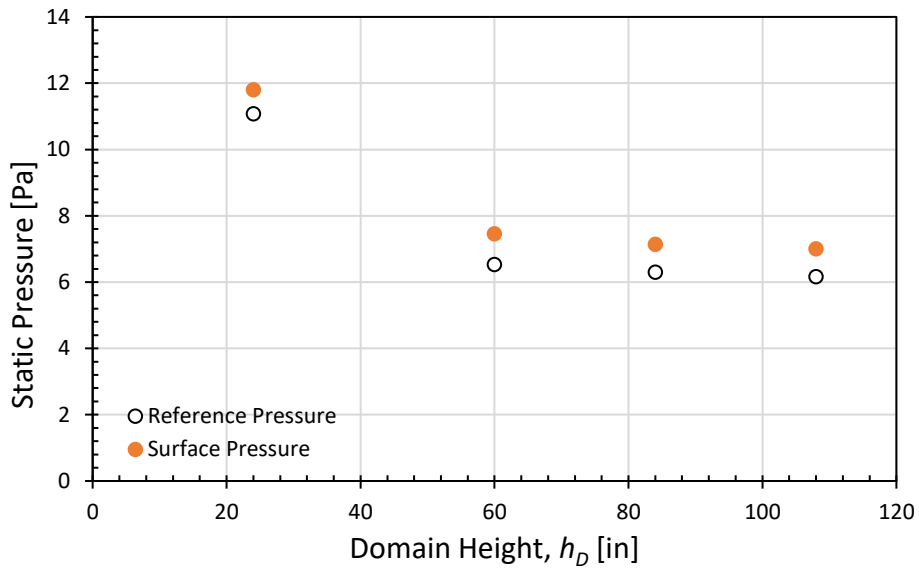


Figure I-2: 3-D RFE Height Independence Study.

Figure I-2 shows that the solution will be unconstrained by the upper boundary of the domain if $h_D \geq 108$ inches.

Table I-3: 3-D RFE Width Independence Study Case Identifiers

Mesh	Domain Width [in] w_D	Domain Height [in] h_D	Reference Dynamic Pressure [Pa] q_{ref}
RFE-W-1	12	24	977.9
RFE-W-2	24	24	977.1
RFE-W-3	48	24	977.1
RFE-W-4	60	24	977.5

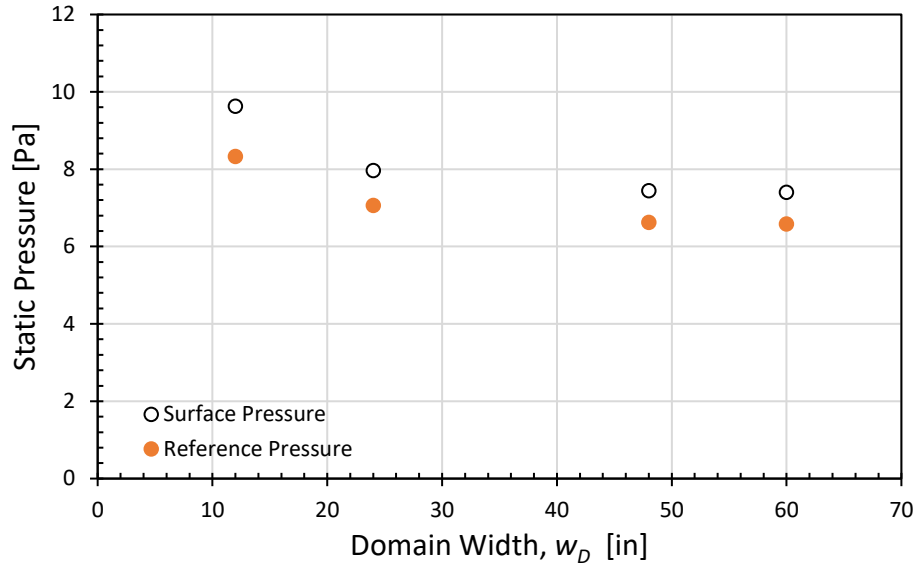


Figure I-3: 3-D Enclosure Width Independence Study.

Figure I-3 shows that the solution will be unconstrained by the sides of the domain if $w_D \geq 60$ inches. The resulting RFE-A mesh is shown below with critical dimensions in inches.

The mesh edge parameters for each edge labelled in Figure I-4 are listed in Table I-4.

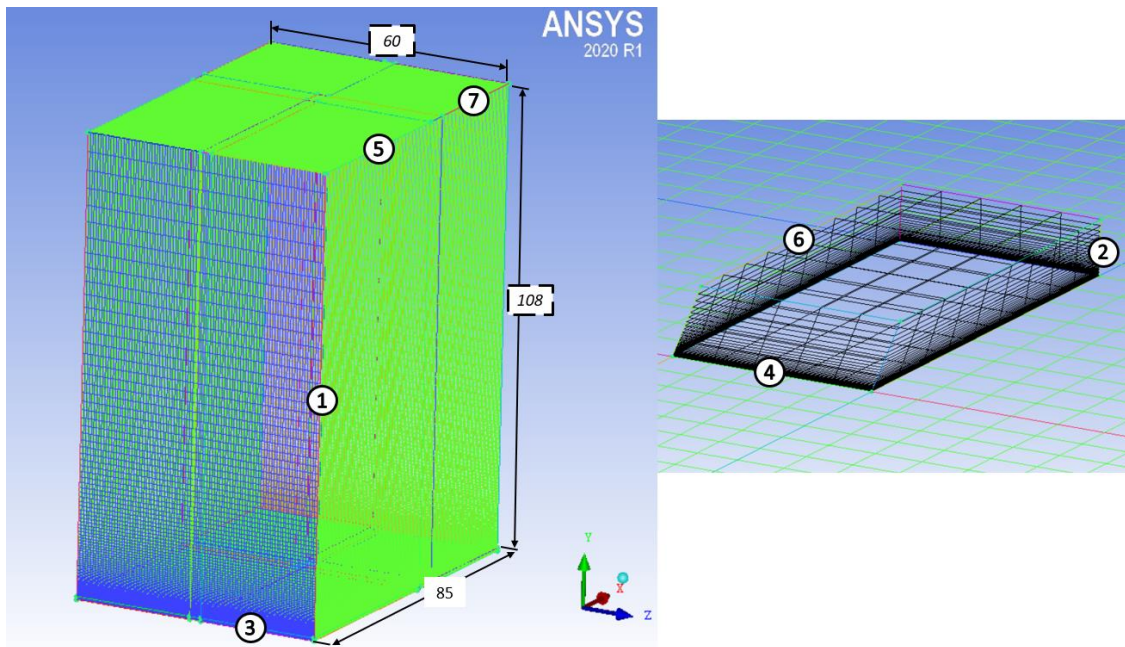


Figure I-4: 3-D RFE-A Mesh.

Table I-4: 3-D RFE-A Mesh Edge Parameters.

Edge	Length [in]	Nodes	Mesh Law	Spacing 1	Ratio 1	Spacing 2	Ratio 2
1	107.269	93	Geometric 1	0.1	1.2	0	2
2	0.7315	40	Geometric 1	0.001	1.1	0	2
3	28.6092	45	Uniform	0	2	0	2
4	2.7815	6	Uniform	0	2	0	2
5	48.7315	80	Uniform	0	2	0	2
6	5.4385	10	Uniform	0	2	0	2
7	30.85	52	Uniform	0	2	0	2

Appendix J. 3-D HSF-A Mesh, Height, and Width Independence Study

Table J-1: 3-D Half-Scale Fairing Mesh Independence Study Case Identifiers

Mesh	Grid Points	Reference Dynamic Pressure [Pa] q_{ref}
HSF-M-1	179,338	1030.0
HSF-M-2	547,233	1029.6
HSF-M-3	963,000	1031.1

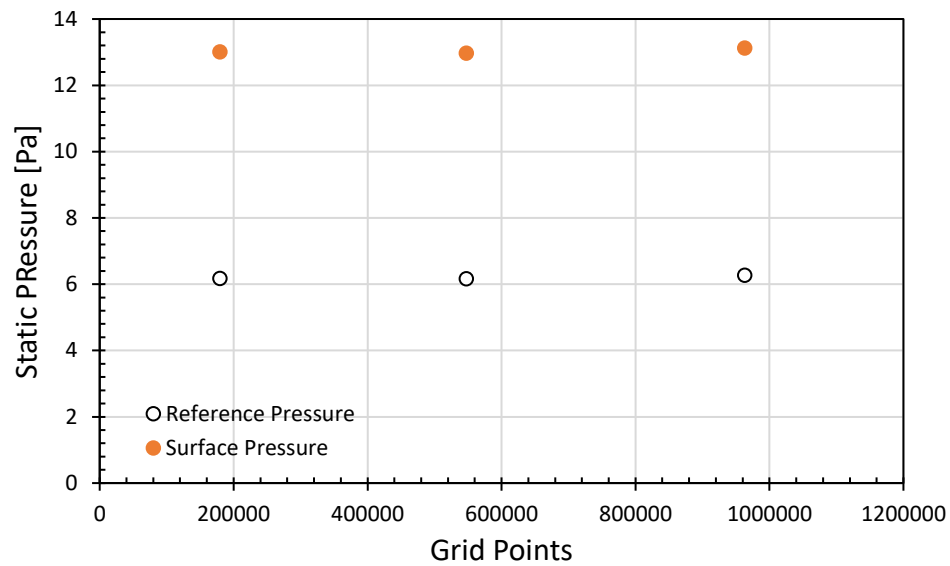


Figure J-1: 3-D Half-Scale Fairing Mesh Independence Study.

Mesh independence was achieved with about 1,000,000 grid points on mesh HSF-M-3 as the surface and reference static pressures changed by 0.27% and 0.08% between HSF-M-2 and HSF-M-3, respectively. The edge parameters from mesh HSF-M-3 were scaled with each change in height and width to maintain the mesh pattern during the height and width independence studies below.

Table J-2: 3-D HSF Height Independence Study Case Identifiers

Mesh	Domain Width [in] w_D	Domain Height [in] h_D	Reference Dynamic Pressure [Pa] q_{ref}
HSF-H-1	100	60	1031.1
HSF-H-2	100	108	1030.0
HSF-H-3	100	132	1029.8

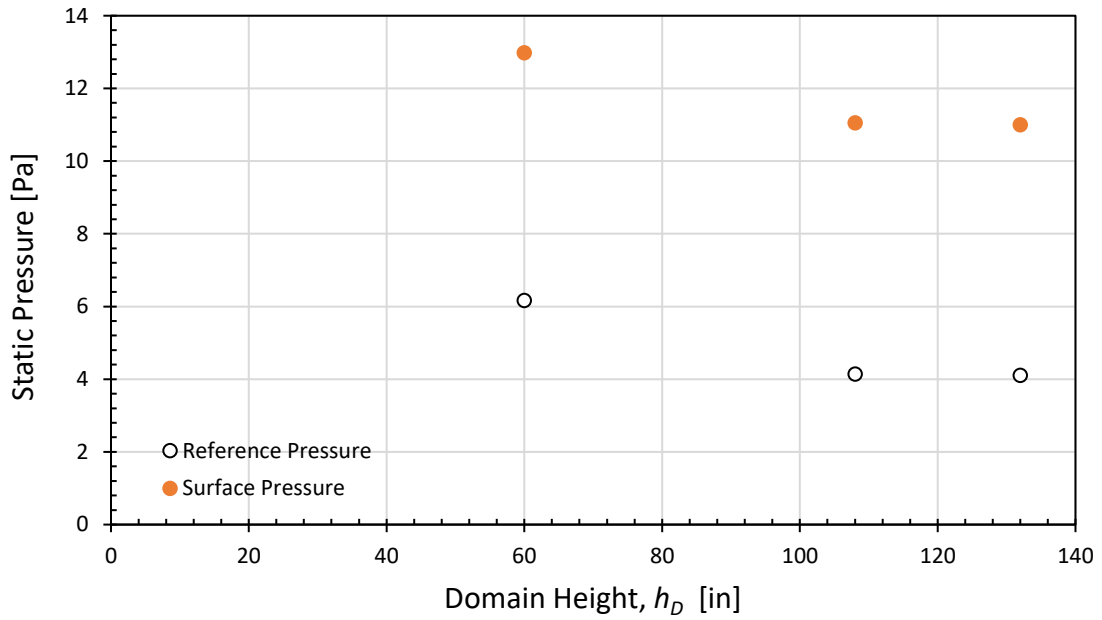


Figure J-2: 3-D HSF Height Independence Study.

Figure J-2 shows that the solution will be unconstrained by the upper boundary of the domain if $h_D \geq 132$ inches.

Table J-3: 3-D HSF Width Independence Study Case Identifiers

Mesh	Domain Width [in] w_D	Domain Height [in] h_D	Reference Dynamic Pressure [Pa] q_{ref}
HSF-W-1	88	60	1031.2
HSF-W-2	100	60	1031.1
HSF-W-3	120	60	1030.5

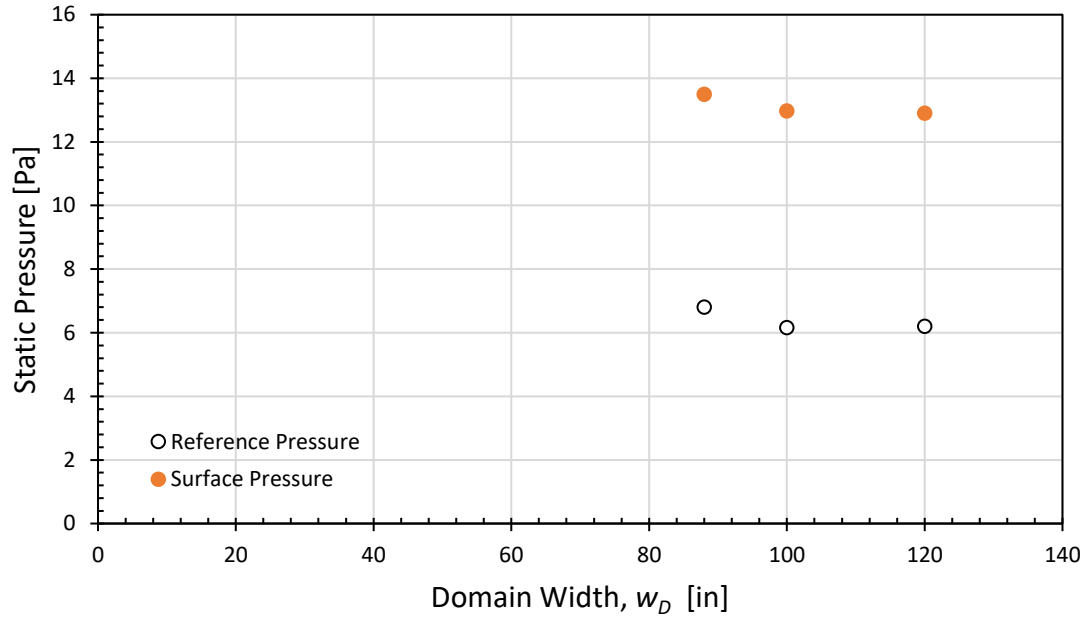


Figure J-3: 3-D HSF Width Independence Study.

Figure J-3 shows that the solution will be unconstrained by the sides of the domain if $w_D \geq 100$ inches. The resulting HSF-A mesh is shown below with critical dimensions in inches. The mesh edge parameters for each edge labelled in Figure J-4 are listed in Table J-4.

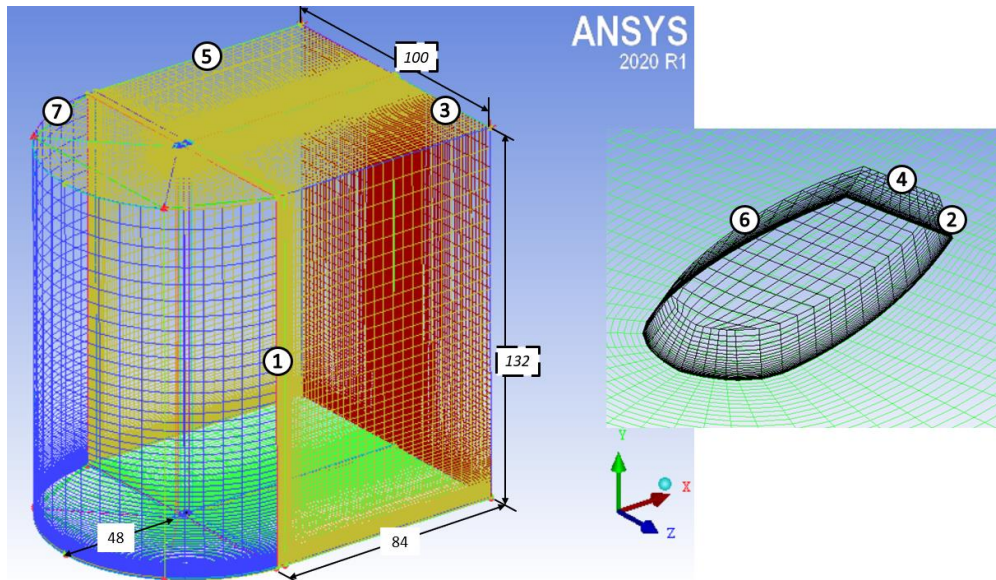


Figure J-4: 3-D HSF-A Mesh.

Table J-4: 3-D HSF-A Mesh Edge Parameters.

Edge	Length [in]	Nodes	Mesh Law	Spacing 1	Ratio 1	Spacing 2	Ratio 2
1	131.316	78	Geometric 1	0.1	1.1	0	2
2	0.684	25	Geometric 1	0.005	1.1	0	2
3	49.275	75	Geometric 2	0	2	0.1	1.2
4	76.1467	11	Uniform	0	2	0	2
5	83.85	40	BiGeometric	0.3	1.1	0	2
6	3.35	9	Uniform	0	2	0	2
7	30.076	7	Uniform	0	2	0	2

Appendix K. p_{ref} Locations and Values for all 2-D and 3-D CFD Cases

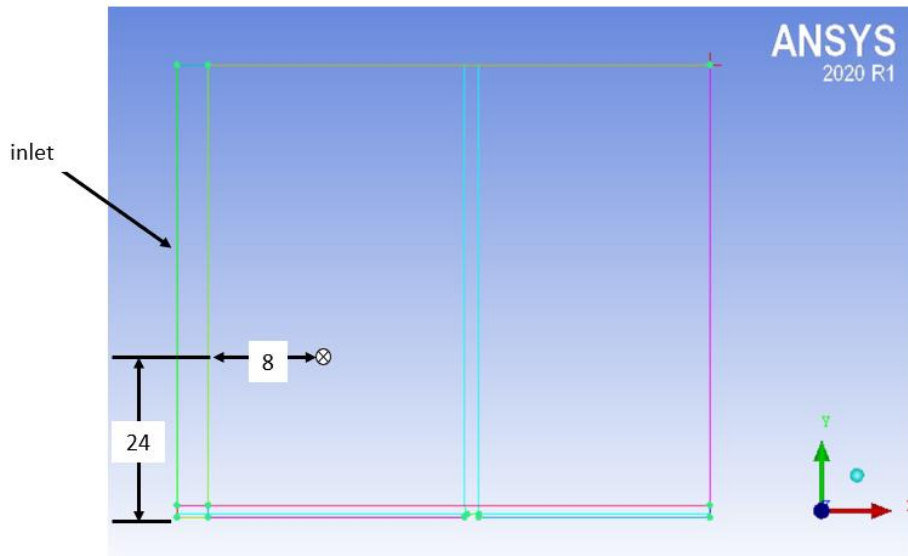


Figure K-1: Location of Free Stream Reference Static Pressure for 2-D CFD Cases.

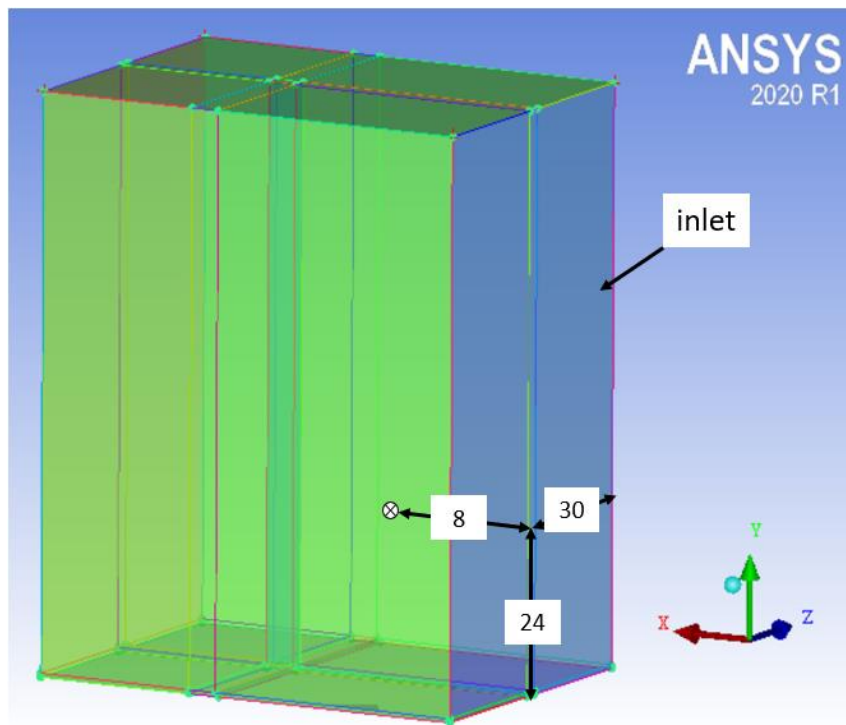


Figure K-2: Location of Free Stream Reference Static Pressure for 3-D RFE Cases.

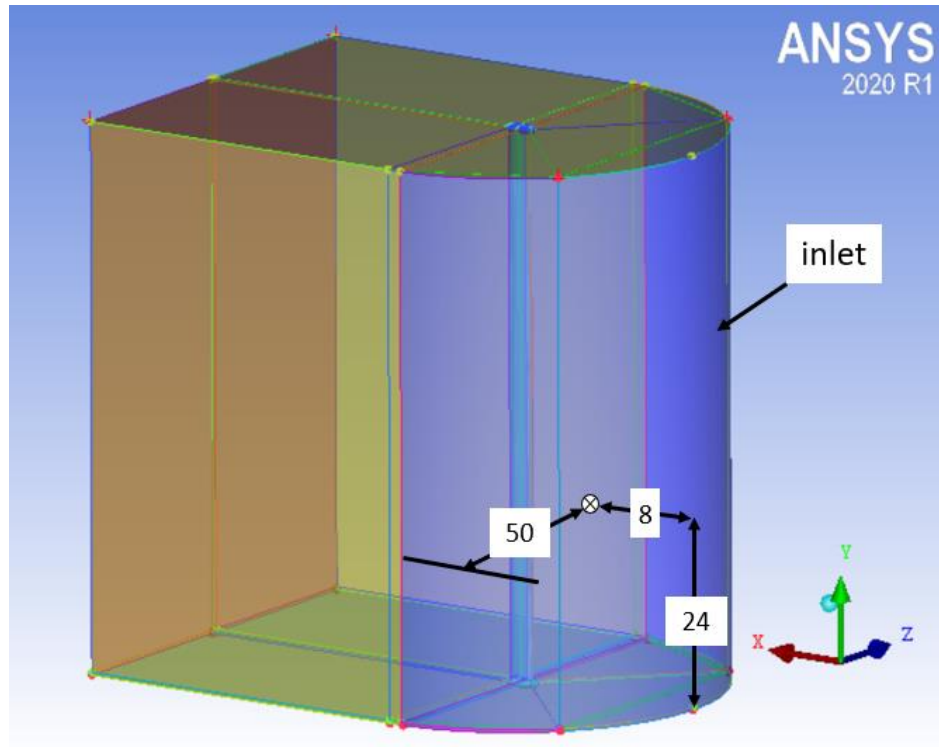


Figure K-3: Location of Free Stream Reference Static Pressure for 3-D HSF Cases.

Table K-1: Free Stream Reference Static Pressure for CFD Cases.

	Case	Mesh	Reference Static Pressure, p_{ref} [Pa]
2-D Cases	1	TB	87.61
	2	SB	44.51
	3	TA	43.96
	4	SA	14.43
3-D Cases	1	RFE-A	4.070
	2	HSF-A	8.420
	5	RFE-A	4.013
	6	RFE-A	4.013
	7	RFE-A	4.120
	8	RFE-A	3.990